2016-03

Prototype design and mission analysis for a small satellite exploiting environmental disturbances for attitude stabilization

Polat, Halis C.

Monterey, California: Naval Postgraduate School

NAVAL POSTGRADUATE SCHOOL

MONTEREY, CALIFORNIA

THESIS

PROTOTYPE DESIGN AND MISSION ANALYSIS FOR A SMALL SATELLITE EXPLOITING ENVIRONMENTAL DISTURBANCES FOR ATTITUDE STABILIZATION

by

Halis C. Polat

March 2016

Thesis Advisor: Marcello Romano
Co-Advisor: Stephen Tackett

Approved for public release; distribution is unlimited

THIS PAGE INTENTIONALLY LEFT BLANK

REPORT DOCUMENTATION PAGE			*Form Approved OMB No. 0704–0188*
Public reporting burden for this collection of information is estimated to average 1 hour per response, including the time for reviewing instruction, searching existing data sources, gathering and maintaining the data needed, and completing and reviewing the collection of information. Send comments regarding this burden estimate or any other aspect of this collection of information, including suggestions for reducing this burden, to Washington headquarters Services, Directorate for Information Operations and Reports, 1215 Jefferson Davis Highway, Suite 1204, Arlington, VA 22202-4302, and to the Office of Management and Budget, Paperwork Reduction Project (0704-0188) Washington, DC 20503.			
1. AGENCY USE ONLY ***(Leave blank)***	**2. REPORT DATE** March 2016	**3. REPORT TYPE AND DATES COVERED** Master's thesis	
4. TITLE AND SUBTITLE PROTOTYPE DESIGN AND MISSION ANALYSIS FOR A SMALL SATELLITE EXPLOITING ENVIRONMENTAL DISTURBANCES FOR ATTITUDE STABILIZATION			**5. FUNDING NUMBERS**
6. AUTHOR(S) Halis C. Polat			
7. PERFORMING ORGANIZATION NAME(S) AND ADDRESS(ES) Naval Postgraduate School Monterey, CA 93943-5000			**8. PERFORMING ORGANIZATION REPORT NUMBER**
9. SPONSORING /MONITORING AGENCY NAME(S) AND ADDRESS(ES) N/A			**10. SPONSORING / MONITORING AGENCY REPORT NUMBER**
11. SUPPLEMENTARY NOTES The views expressed in this thesis are those of the author and do not reflect the official policy or position of the Department of Defense or the U.S. Government. IRB Protocol number ____N/A____.			
12a. DISTRIBUTION / AVAILABILITY STATEMENT Approved for public release; distribution is unlimited			**12b. DISTRIBUTION CODE**

13. ABSTRACT (maximum 200 words)

In order to accomplish complex and sophisticated missions, small satellites, particularly CubeSat, need a robust and accurate attitude control system. Due to the mass- and volume-constrained design environment of CubeSat, conventional methods are sometimes inadequate to provide needed performance at low altitudes where environmental disturbances are high. This thesis studies exploitation of the most dominant disturbance torque at low altitudes (i.e., the residual aerodynamic torque) for stabilization and attitude control. By shifting internal masses, the distance between the center of pressure and the center of mass is adjusted so that the aerodynamic torque can be modulated as the control torque. To establish a realistic simulation environment, all launched CubeSat missions were analyzed in terms of their attitude control methodologies, sizes, altitudes and mission types. In light of the mission analysis, a prototype 3U CubeSat was designed with only commercial off-the-shelf components to check the practicality and feasibility of the method. The Linear Quadratic Regulator control method with gain scheduling was used to stabilize and control the attitude in a high-fidelity simulation environment. In simulations, the method stabilized the CubeSat and maintained the desired attitude under varying conditions such as initial angular velocity and displacement, orbit altitude and inclination, shifting mass fraction and CubeSat alignment and size.

14. SUBJECT TERMS CubeSat Prototype Design, shifting mass, attitude stabilization, CubeSat Mission Analysis, LQR with gain scheduling, exploitation of environmental disturbances			**15. NUMBER OF PAGES** 167
			16. PRICE CODE
17. SECURITY CLASSIFICATION OF REPORT Unclassified	**18. SECURITY CLASSIFICATION OF THIS PAGE** Unclassified	**19. SECURITY CLASSIFICATION OF ABSTRACT** Unclassified	**20. LIMITATION OF ABSTRACT** UU

NSN 7540–01-280-5500 Standard Form 298 (Rev. 2–89)
Prescribed by ANSI Std. 239–18

THIS PAGE INTENTIONALLY LEFT BLANK

Approved for public release; distribution is unlimited

PROTOTYPE DESIGN AND MISSION ANALYSIS FOR A SMALL SATELLITE EXPLOITING ENVIRONMENTAL DISTURBANCES FOR ATTITUDE STABILIZATION

Halis C. Polat
First Lieutenant, Turkish Air Force
B.S., Turkish Air Force Academy, 2009

Submitted in partial fulfillment of the
requirements for the degree of

MASTER OF SCIENCE IN SPACE SYSTEMS OPERATIONS

from the

NAVAL POSTGRADUATE SCHOOL
March 2016

Approved by: Marcello Romano, Ph.D.
Thesis Advisor

Stephen Tackett
Co-Advisor

Rudy Panholzer, Ph.D.
Chair, Space Systems Academic Group

THIS PAGE INTENTIONALLY LEFT BLANK

ABSTRACT

In order to accomplish complex and sophisticated missions, small satellites, particularly CubeSat, need a robust and accurate attitude control system. Due to the mass- and volume-constrained design environment of CubeSat, conventional methods are sometimes inadequate to provide needed performance at low altitudes where environmental disturbances are high. This thesis studies exploitation of the most dominant disturbance torque at low altitudes (i.e., the residual aerodynamic torque) for stabilization and attitude control. By shifting internal masses, the distance between the center of pressure and the center of mass is adjusted so that the aerodynamic torque can be modulated as the control torque. To establish a realistic simulation environment, all launched CubeSat missions were analyzed in terms of their attitude control methodologies, sizes, altitudes and mission types. In light of the mission analysis, a prototype 3U CubeSat was designed with only commercial off-the-shelf components to check the practicality and feasibility of the method. The Linear Quadratic Regulator control method with gain scheduling was used to stabilize and control the attitude in a high-fidelity simulation environment. In simulations, the method stabilized the CubeSat and maintained the desired attitude under varying conditions such as initial angular velocity and displacement, orbit altitude and inclination, shifting mass fraction and CubeSat alignment and size.

THIS PAGE INTENTIONALLY LEFT BLANK

TABLE OF CONTENTS

LIST OF FIGURES

THIS PAGE INTENTIONALLY LEFT BLANK

LIST OF TABLES

THIS PAGE INTENTIONALLY LEFT BLANK

LIST OF ACRONYMS AND ABBREVIATIONS

ACS	Attitude Control System
ADCS	Attitude Determination and Control System
ADS	Attitude Determination System
AIS	Automatic Identification System
AMSAT	Radio Amateur Satellite Corporation
APD	Avalanche Photodiode
C2	Command and Control
CAD	Computer Aided Design
CDS	CubeSat Design Specification
CMG	Control Moment Gyroscope
CoM	Center of Mass
CoP	Center of Pressure
COTS	Commercial-Off-the-Shelf
CSD	Canisterized Satellite Dispenser
CTECS	Compact Total Electron Contact Sensor
DCM	Direction of Cosine Matrix
ECEF	Earth-Centered, Earth-Fixed
ELF	Extremely Low Frequency
EMW	Electromagnetic Wave
ENA	Energetic Neutral Atom
FM	Frequency Modulation
GEO	Geosynchronous Equatorial Orbit
GPS	Global Positioning System
GSD	Ground Sample Distance
HWM07	Horizontal Wind Model 2007
IR	Infra-red
LEO	Low Earth Orbit
LQR	Linear Quadratic Regulator
MoE	Measure of Evaluation
MTV	Miniature Tracking Vehicle

N/A	Not Available
NASA	National Aeronautics and Space Administration
NLAS	Nanosatellite Launch Adapter System
NPSCuL	Naval Postgraduate School CubeSat Launcher
NRLMSISE	Naval Research Laboratory Mass Spectrometer and Incoherent Scatter Radar Exosphere
OBS	On-board Computer
ORS	Operationally Responsive Satellite
PD	Proportional-Derivative
P-POD	Poly-Picosatellite Orbital Deployer
RAAN	Right Ascension of Ascending Node
RW	Reaction Wheel
SSA	Space Situational Awareness
SSO	Sun Synchronous Orbit
UHF	Ultra-High Frequency
UTC	Coordinated Universal Time
VHF	Very High Frequency
VLEO	Very Low Earth Orbit

ACKNOWLEDGMENTS

This thesis would not be complete without the enlightening and critical advice from Dr. Marcello Romano, Stephen Tackett and Dr. Josep Virgili-Llop. It is the final and most extensive product of my postgraduate education in the Space Systems Operations curriculum at the Naval Postgraduate School. In addition, it was a privilege for me to further my education with the distinguished professors in the Space Systems Academic Group. I would like to thank all of them for their sincere and professional advice.

I also want to thank my country, Turkey, and in particular, the Turkish Air Force, for letting me have this academic opportunity.

Finally, I want to thank my wife, Feriste, for her infinite support and patience, and my daughter, Oyku, for bringing me good luck.

THIS PAGE INTENTIONALLY LEFT BLANK

DISCLAIMER

The views expressed in this thesis are those of the author and do not reflect the official policy or position of the Republic of Turkey, Turkish Armed Forces or the Turkish Air Force.

THIS PAGE INTENTIONALLY LEFT BLANK

I. LITERATURE REVIEW AND THEORETICAL FRAMEWORK

Small satellites are grouped according to size. Generally, any satellite under 500 kg is considered small. Nevertheless, the size and power limitations of a small satellite starts with microsatellites that are between 10 and 100 kg. The nano- and picosatellites make up the bottom level of current small-satellite technology. Nanosatellites are between 1–10 kg and picosatellites, 0.1–1 kg. There are also femtosatellites (0.01–0.1 kg), but they are not as common as the others [1].

In 1999, Jordi Puig-Suari from California Polytechnic State University and Bob Twiggs from Stanford University devised a standardized design called the CubeSat. The CubeSat is a low-cost and easy-to-develop alternative to conventional satellites. It is a 10-cm cube and has a maximum mass of 1 kg (Figure 1) [2]. Puig-Suari and Twiggs's goal was to enable graduate students to work on satellite projects in which the students could actually see the launch and perform ground operations. In order to decrease the time-length of the projects, the standardized design of a CubeSat with commercial-off-the-shelf (COTS) components was proposed and has been accepted since then by an increasing number of academic, commercial and military entities such as NASA, Aerospace Corporation, and Planet Labs. The increasing number of launches and successful mission results are the key indicators that investments in the CubeSat concept will continue.

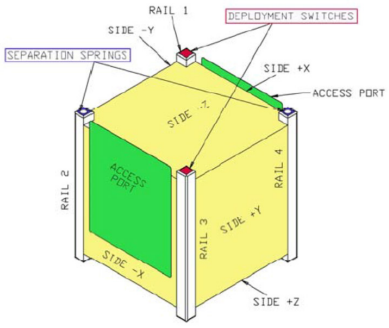

Figure 1. 1U CubeSat

Source [2]: J. Puig-Suari, "The CubeSat: The picosatellite standard for research and education," presented at AIAA SPACE 2008 Conference & Exposition, San Diego, CA, 2008.

The 1U design of a 10-cm cube (Figure 1) was later enlarged for more capable satellites. The 2U, 3U and 1.5U models were the first larger configurations. After that, a 6U (12 kg, 12 x 24 x 36 cm) design was developed for better performance, as it has more space for enhancements and capable components.

Since the first CubeSat launch, the missions have evolved from technology demonstration and education missions, to scientific, military, and commercial missions. Even though all these mission types are still common, the potential of the CubeSat for performing conventional satellite missions is forcing the designers to improve the features of CubeSat. Since these mission types—such as imaging and high throughput communication—require better pointing accuracies, the Attitude Determination and Control System (ADCS) should provide better performance than current technology.

Due to the advancements in micro- and nanotechnologies, CubeSat subsystems and components have improved. However, the intrinsic constraints of CubeSat—mass, volume, and power—make it difficult to achieve missions requiring high performance. Because of these constraints, ADCS is one of the least-developed subsystems of CubeSat. Moreover, CubeSat is more susceptible to external disturbances than the bigger satellites due to the lower inertia per unit area attributes. In addition, the altitude of most CubeSats are in low/very low Earth orbit where environmental disturbances, particularly aerodynamic torque, are the major design drivers for ADCS.

In this thesis, the exploitation of the aerodynamic torque for attitude control will be investigated. In particular, the shifting masses concept is studied by devising a high-fidelity dynamic and simulation environment with a linear control technique. The exploitation of the aerodynamic torque is demonstrated in a study [3] with three shifting masses and is supplemented with a reaction wheel or a magnetorquer in one axis if required to stabilize a 3U CubeSat. This means that the major disturbance torque at low Earth orbit (LEO) can be harnessed as a control torque that decreases the need for high power and massive solutions for generating the requested torque.

The methodology to exploit the aerodynamic torque is the use of shifting masses to change the location of the center of mass (CoM) with respect to the center of pressure

(CoP) [3]. With that, the direction and magnitude of the aerodynamic torque can be controlled within the limitation of the mass and travel range of the shifting masses. The modulation of the aerodynamic torque damps the rotational kinetic energy of the system, causing it to stabilize about the equilibrium point.

In this thesis, the proposed attitude control methodology will be investigated in a more advanced simulation model, which includes the gravity gradient torque besides the aerodynamic torque and also the horizontal winds and co-rotation of the atmosphere for better determining the aerodynamic drag force. The dynamics plant will also include shifting masses' dynamics in terms of relative and absolute acceleration and velocity. In addition, the control methodology will consist of a linear control unlike the nonlinear control in the original study [3]. The establishment of the model and the control logic are presented in Chapter IV.

In order to simulate a more realistic environment and platform in the simulation, both CubeSat missions and design characteristics have been studied. First, all launched CubeSat missions have been investigated in terms of configuration, operational altitude, attitude control methodology, and mission type and success rate. That analysis allows us to see the trends in attitude control methodologies and prove the active control methods' increasing numbers. In addition, the parameters that will be used in the simulation will be more realistic from this CubeSat mission data analysis. The simulation will mimic the current trends in terms of mission characteristics. CubeSat mission data analysis is presented in Chapter II.

To mimic a real CubeSat platform in the simulation, a prototype design is also made. Including the shifting masses actuators, all components of the prototype are COTS and fit in a 3U CubeSat. The shifting masses actuator system is also demonstrated in a 1U-size CAD model that has enough space to contain all of the shifting masses. All of the simulation inputs, such as mass and travel range of the shifting masses system, CoM location, total mass, and inertia will be derived from the prototype design to prevent unrealistic simulation parameters. The prototype design is presented in Chapter III.

The evaluation of the simulation results based on the CubeSat data mission analysis and the prototype design is presented in Chapter V. Different configurations are investigated to distinguish the good design spots of the proposed attitude control methodology. In addition, the number of the shifting masses is investigated for determining optimal design choice. Further development ideas and a conclusion to the research topic are presented in Chapter VI.

A. CUBESAT

On August 4, 1957, the satellite age started with a sphere that was 58 cm in diameter and weighed 83 kg. That satellite, Sputnik, was launched as a LEO satellite with 92 days of mission duration. Then, on February 1, 1958, Explorer I, which was 14 kg, was launched into an elliptical orbit at LEO with 111 days of mission duration. After Explorer I and Sputnik were launched (in fact, the first small satellites), satellites evolved and got bigger in every dimension. Mass, height, width, length, mission duration and even the orbital altitudes got bigger, wider, and higher. The performance requirements dictated bigger satellites, so bigger satellites were built as launch capabilities allowed. Some examples of the extent to which satellite technology reached in the Geosynchronous Equatorial Orbit (GEO) belt are large antennas and solar panels on satellites, large telescopes as payloads on spacecraft and the football-field size of the International Space Station. Furthermore, entrepreneurs are still pursuing bigger and larger satellites. However, smaller satellites are gaining recognition [4].

Small satellites came to the space technology platform again in the 1990s as an alternative to satellites with high costs and long development times. Many countries were unable to send satellites due to the expense. With the small satellites, the opportunity of having access to space became available to companies and developing countries. Commercial companies like Surrey Satellite Technologies drew attention to the practicality of the small satellites. Universities pursued the trend and established small-satellite labs in their premises [4].

The other feature of the CubeSat program is the launching opportunities. With standardized launchers, any qualified satellite developer can send their satellite with

shared costs. This particular feature is the reason for the spread of the idea among universities and corporations from all over the world. It all started with the Poly-Picosatellite Orbital Deployer P-POD (Figure 2) designed in conjunction by California Polytechnic State University and the Space Systems Development Laboratory at Stanford University. The P-POD is capable of launching CubeSat from 1U up to 3U configuration [2]. Along with the P-POD, there are other CubeSat launchers such as: the NanoRacks CubeSat Deployer at the International Space Station [5]; the Nanosatellite Launch Adapter System (NLAS) Dispenser [6] by NASA; the CubeSat Launcher (NPSCuL) at the Naval Postgraduate School [7]; and ISIPOD and ISIS 6-POD by Innovative Solutions in Space BV [8].

Figure 2. P-POD

Source [2]: J. Puig-Suari, "The CubeSat: The picosatellite standard for research and education," presented at AIAA SPACE 2008 Conference & Exposition, San Diego, CA, 2008.

The request for larger, standardized CubeSat from governments and commercial markets drove the nanosatellite-size CubeSat into the design sheets. This was followed by new launcher designs and specifications for configurations up to 27U (54 kg, 34 x 35 x 36 cm). These launchers are called Canisterized Satellite Dispensers-CSD (Figure 3) or "Canisters" [9].

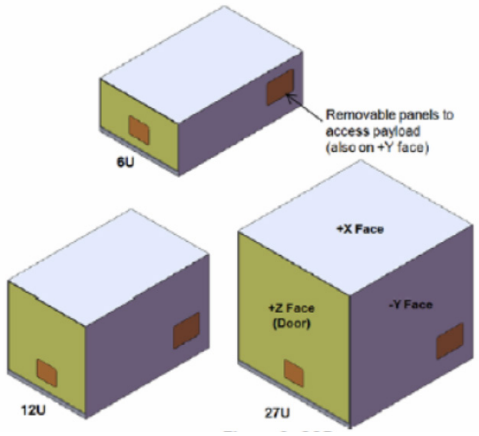

Figure 3. Canisterized Satellite Dispenser

Source [9]: R. Hevner, W. Holemans, J. Puig-Suari, and R. Twiggs, "An Advanced Standard for CubeSats," in *25th Annual AIAA/USU Conference on Small Satellites*, Logan, UT, 2011, p. 9.

Even though a less expensive and faster way to space by the standardized CubeSat concept is highly advantageous, it comes with intrinsic limitations. In fact, in order to benefit from the CubeSat, one needs to overcome the power, mass, and volume limitations. These limitations affect the subsystems that can be carried along with the limited payload capabilities. Mostly due to these reasons, the attitude determination and control system for most of the CubeSat is noticeably less developed or even absent in some cases. ADCS needs power, mass and size, all of which are limited, as previously stated. Hence, attitude knowledge and pointing accuracy become the mission critical points for the projects.

Without an accurate attitude knowledge and pointing accuracy, the performance and outcome of most mission types are not promising. For example, in order to acquire higher resolution images, designers have to decrease ground sample distance (GSD) as much as possible. However, in that case pointing accuracy and pointing stability highly affect the maintainability of the GSD and eventually the image quality [10]. Currently, there is an increasing number of technology demonstration missions just for ADCS components, such as micro-reaction wheels (BEESAT [11]), magnetic torquers (e-st@r [12]), micropropulsion (POPSAT-HIP-1 [13]), or even CMGs (SwampSat [14]).

The CubeSat program promises highly profitable applications, but as long as pointing accuracy and the controllability of the satellites remain weak, these promises cannot be realized. Whenever a reliable and accurate 3-axis-stabilized CubeSat is demonstrated and proven, these picosatellites can be as valuable as the larger satellites or at least fill existing gaps [15].

The miniaturization of the proven attitude control components will enable CubeSat with a pointing accuracy less than 1 degree, but the current typical CubeSat pointing accuracy is approximately 2 degrees [16]. With that technological improvement, different types of missions can be fulfilled.

B. ENVIRONMENTAL DISTURBANCES

Environmental disturbances shape the ADCS design in every aspect. Smaller spacecraft exposed to environmental disturbances are much worse due to their low inertial properties per unit area. As stated earlier, the physical limitations of these small satellites make it challenging to overcome these disturbances.

There are four main environmental disturbances to consider during spacecraft design: Gravity Gradient Effect, Aerodynamic Torque, Solar Radiation, and Earth's Magnetic Field [17]. These four disturbances vary mostly due to orbit altitude. At LEO and Very Low Earth Orbit (VLEO < 450 km), the dominant disturbance is aerodynamic torque.

1. Aerodynamic Torques

Even though the density of the atmosphere is low at LEO altitudes, there are atmospheric particles that generate aerodynamic drag on orbiting spacecraft. The generated drag force on different surfaces and the distance between the CoP and the CoM, $\vec{r}_{cp}$, create the aerodynamic torque [17].

Aerodynamic torque is the main disturbance torque at low altitudes. Hence, to model and estimate the torque is highly important for the spacecraft design. However, there are difficulties due to multiple unknowns such as solar activity, which affects atmospheric density ρ, high altitude winds, and co-rotation of the atmosphere, which

affect the relative wind velocity magnitude and direction $\vec{V}$. All these eventually change the outcome of the aerodynamic torque equation. Equation 1.1 can be used for preliminary designs, but for more accurate design models, a thorough analysis is required.

$$\vec{T}_{Aero} = (\frac{1}{2}\rho \vec{V}^2 C_D A) \times \vec{r}_{cp} \tag{1.1}$$

Hughes [18] approach to aerodynamic torque is accepted throughout this thesis. At LEO, molecular mean free path is much larger than spacecraft dimensions (approximately 1 km); it means that one atmospheric particle hits the spacecraft before interacting with other particles. This allows us to use free molecular flow model rather than continuum flow model [18].

Free molecular flow model enables us to treat particle interactions with spacecraft surfaces individually. In addition, we can add the effect of each surface and acquire the total complex structure value with this assumption [18]. In order to accomplish this we need to determine the shadowing status and momentum exchange model (Figure 4).

In this free molecular flow model, momentum exchange can be divided into two different phases: The impact and the leaving. In the impact the molecule diffuses among the other molecules and gives away all its energy and direction information. When the molecule finally leaves the surface, its energy and the direction will be determined by probabilistic kinetic energy property of the surface temperature [18]. We will assume that the leaving energy is negligible.

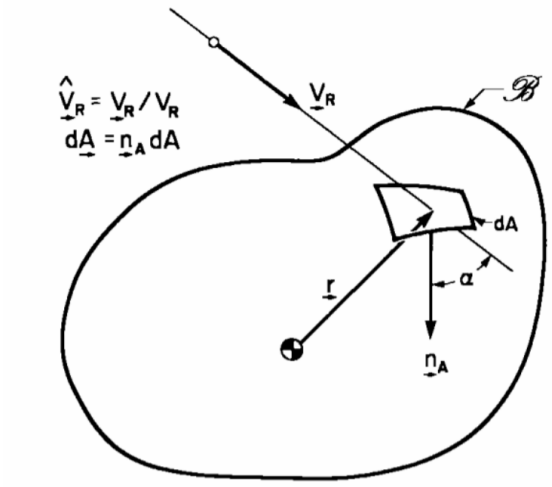

Figure 4. Molecule and Surface Element Interaction

Source [18]: P. C. Hughes, *Spacecraft Attitude Dynamics*, Mineola, NY: Dover Publications, 2004.

The momentum flux of the molecule can be considered as the force element with those assumptions. This leads us to the force element equation [18]:

$$d\underset{\rightarrow}{f} = \rho V_R^2 \cos\alpha \hat{V}_{\underset{\rightarrow}{R}} dA\,, \tag{1.2}$$

where α is the angle of attack and equals to $\cos^{-1}(\hat{V}_{\underset{\rightarrow}{R}} \bullet \hat{n}_{\underset{\rightarrow}{A}})$ and $\hat{n}_{\underset{\rightarrow}{A}}$ is the unit inward normal to the surface. When Equation 1.2 is integrated for the whole body and the shadowing considerations are implemented, we have the total force equation [18]:

$$\underset{\rightarrow}{f} = \oiint H(\cos\alpha)\rho V_R^2 \cos\alpha dA \hat{V}_{\underset{\rightarrow}{R}}\,, \tag{1.3}$$

where Heaviside function is used for shadowing (when $x \geq 0$, $H(x) = 1$, otherwise $H(x) = 0$) [18].

By definition, it is known that the center of pressure is considered as the point that total force acts on. Thus, the total torque will be the cross product of the aerodynamic drag force and the center of pressure position vector relative to center of mass $r_{\underset{\rightarrow}{cp}}$:

$$\underset{\rightarrow}{T}_{Aero} = \underset{\rightarrow}{r}_{cp} \times \underset{\rightarrow}{f} \tag{1.4}$$

2. Gravity-Gradient Torque

Gravitational effect varies for different parts of spacecraft, as their distances to the center of Earth are not the same. These force gradients create a net torque on spacecraft that is called gravity-gradient torque [17].

Gravity-gradient torque is typically the second most dominant torque at LEO. For preliminary designs, it can be calculated by applying worst-case conditions:

$$T_{gg} = \frac{3\mu}{2R^3}\left|I_z - I_y\right|\sin(2\theta), \tag{1.5}$$

where μ is the gravitational constant for the body (for Earth = 3.986 x 10^{14} m^3/s^2), R is the distance from the Earth's center, I_z and I_y are the moments of inertia about z and y axes and θ is the angle of maximum deviation from local vertical [19].

Again, this calculation is not adequate for ADCS modeling purposes. The Wie [20] approach for the formulation of the gravity-gradient torque is followed in this thesis:

$$T_{gg} = 3\sqrt{\frac{\mu}{R^3}}\vec{a} \times \hat{J} \cdot \vec{a}, \tag{1.6}$$

where $\hat{J}$ is the inertia matrix and $\vec{a}$ is the direction of cosines of the local vertical relative to body triad. In matrix format, Equation 1.6 can be written as [20]:

$$\begin{bmatrix} T_{gg_1} \\ T_{gg_2} \\ T_{gg_3} \end{bmatrix} = 3\sqrt{\frac{\mu}{R^3}} \begin{bmatrix} 0 & -C_{33} & C_{23} \\ C_{33} & 0 & -C_{13} \\ -C_{23} & C_{13} & 0 \end{bmatrix} \begin{bmatrix} J_{11} & J_{12} & J_{13} \\ J_{21} & J_{22} & J_{23} \\ J_{31} & J_{32} & J_{33} \end{bmatrix} \begin{bmatrix} C_{13} \\ C_{23} \\ C_{33} \end{bmatrix}, \tag{1.7}$$

where $\begin{bmatrix} C_{13} \\ C_{23} \\ C_{33} \end{bmatrix}$ is the third column of the direction of cosine matrix of body triad relative to orbital triad.

3. Solar Torque

Similar to aerodynamic drag, the photons coming from the sun hit the surface of the spacecraft and create a force. Due to displacement between the center of solar pressure and center of mass $\vec{r}_{ps}$, the impact force creates a torque on spacecraft. The force depends on the surface reflectance factor q. A rough estimation for reflectance factor is that the solar arrays are considered as absorbers (q=0) and spacecraft body as reflectors (q=0.5-1) [19].

Even though solar radiation effect on spacecraft is small, its effect is continuous and, in the long term, it disturbs the attitude of the spacecraft. Designers often consider the worst case solar torque in their ADCS designs [18]:

$$T_{sp} = \frac{F_s}{c} A_s (1+q) \cos i \left(\left| \vec{r}_{ps} \right| \right), \tag{1.8}$$

where F_s is the solar constant, c is the speed of light, A_s is the surface, i is the solar incidence angle.

In this thesis, the solar torque will be ignored in the environmental disturbance calculations due to its very small effect in short term missions as it is the case for LEO or VLEO CubeSat missions.

4. Magnetic Torque

The fourth environmental disturbance that a spacecraft faces along its mission is Magnetic Torque. As different types of electronic devices drive and generate currents for the spacecraft operation, those current loops and other magnetic devices, if they are present, cause a magnetic moment $\vec{m}_m$ for the spacecraft. Earth's magnetic field $\vec{B}$

interacts with the magnetic moment of the spacecraft and generate a magnetic torque on the spacecraft [18]:

$$\vec{T}_{mag} = \underrightarrow{m}_m \times \underrightarrow{B} \tag{1.9}$$

When the net magnetic moment of the spacecraft is zero, there is no magnetic torque on the spacecraft from the magnetic field of the Earth. At that condition, the magnetic moment does not change due the orientation of the spacecraft [18]. This is useful for eliminating the magnetic torque with adjustable magnets that can always control the magnetic moment's value. However, the calculation of the magnetic torque with magnetic moment values other than zero needs a geomagnetic field model. With the latitude, longitude and the distance in geomagnetic reference frame, the magnetic field vector of the Earth can be estimated. Then, the transformation to the body triad is needed to calculate the magnetic torque on spacecraft.

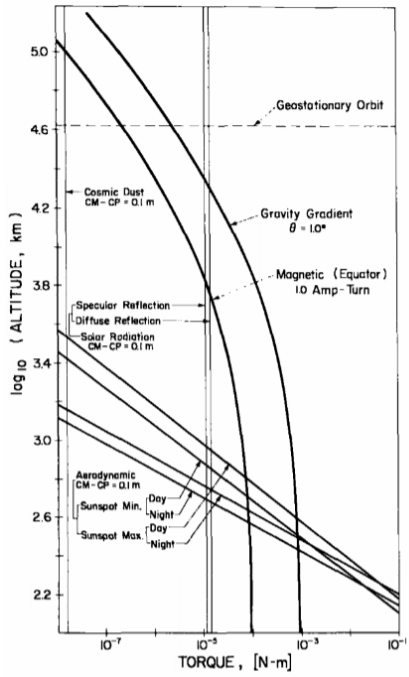

Figure 5. The Environmental Disturbance Torques for a Typical Spacecraft

Source [18]: P. C. Hughes, *Spacecraft Attitude Dynamics*, Mineola, NY: Dover Publications, 2004.

As altitude changes, all of the torques change with different trends except the solar torque which can be seen in Figure 5 ($T_{gg}, T_{mag} \sim R^{-3}; T_{aero} \sim \rho_{atm} \sim e^{-altitude}$) [18]. Therefore, the dominant torques change due to the operational altitude. For more accurate results, solar activity can be included into the design models, which is very hard to predict.

C. EXPLOITATIONS OF ENVIRONMENTAL DISTURBANCES

The environmental disturbances that are explained earlier have to be compensated to perform the mission within the limits. There are proven ways for controlling the attitude such as reaction/momentum wheels, control moment gyros, magnetic torquers, and thrusters. In addition, the use of the environmental torques in favor of the spacecraft attitude control has been studied since the spacecraft age began.

The oldest technique is the gravity gradient stabilization. The method exploits the relation between inertial parameters of a spacecraft and the gravity gradient torque. When the minimum inertia axis of a spacecraft aligns with the local vertical axis, the roll and pitch angular rates are decreased by gravity gradient torque proportional to the difference in inertial values ($I_{\min} - I_{\text{int}}$ & $I_{\min} - I_{\max}$) [18]. Thus, gravity gradient torque tends to stabilize the spacecraft in nadir-fixed pointing attitude within some number of degrees depending on the altitude and the configuration. In order to improve the stabilizing effect of the gravity gradient torque, designers added extendible booms to the spacecraft to increase the difference between minimum inertia and the other two inertias by increasing the maximum and the intermediate inertias.

The gravity gradient stabilization is a cheap passive control technique that has been used by many spacecraft including the Space Shuttle and the International Space Station. Small satellites are also adapting this method as either their primary or secondary attitude control systems. Some examples from the CubeSat missions are UniCubeSat-GG with extendable solar array panels by the University of Rome [21], CP10 (EXOCUBE) with deployable booms by California Polytechnic State University [22], and DTUsat with a deployable boom of 1.4 meters by the National Space Institute at the Technical University of Denmark [23].

Another method is the use of permanent magnets to align the CubeSat with Earth's magnetic field which is the most common method adopted by the CubeSat designers due to its simplicity. With the permanent magnets that can be mounted in the desired axis, the magnetic moment of the spacecraft can be increased along that axis. Since the magnetic torque always tries to align the magnetic moment with the magnetic field, spacecraft has a stabilizing torque. It is the same as the needle in a compass.

On the other hand, permanent magnets cannot generate magnetic torque about the magnetic field's direction. In order to dampen the rotational energy, magnetic hysteresis materials are used in the perpendicular plane. Hysteresis rods periodically magnetize and demagnetize due to their magnetic characteristics (high magnetic permeability). This periodic magnetization dissipates the rotational energy.

The passive magnetic control is highly depended on orbit selection. For example, a spacecraft in LEO with zero inclination angle will have a nearly constant magnetic field direction while a polar orbiting satellite will see the magnetic field changing direction. The unsteady nature of the magnetic field in terms of magnitude and the direction makes it an ineffective method for missions with precise pointing requirements. Despite the inherent problems, many CubeSat missions use passive magnetic control method. Some examples are ITUpSAT-1 and TurkSat-3USat with permanent magnet and hysteresis rods by Istanbul Technical University [24], Firebird II-A and Firebird II-B (twin CubeSat) by Montana State University and the University of New Hampshire [24], SkyCube by the Southern Stars Group [25], and CP8 (IPEX) by California Polytechnic State University [26].

Even though solar radiation torque is very small in comparison to other torques in LEO, its continuous effect makes it exploitable for interplanetary missions. The method is called "Solar Sail." The photons hitting the large solar sail create an acceleration. With this small acceleration, spacecraft can reach high velocities since the acceleration is continuous. The other advantage of the solar radiation torque is that it is always present in the solar system while aerodynamic, gravity gradient, and magnetic field torques are not when the spacecraft is not in the vicinity of Earth. One example of the solar sail

application is the NanoSail-D (Figure 6) by NASA, which is a technology demonstration mission for future use of this method [27].

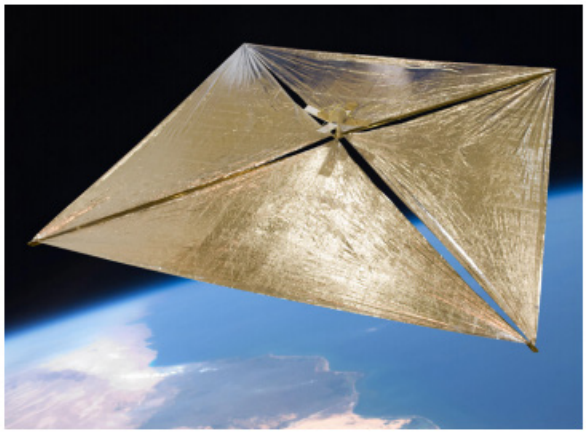

Figure 6. NanoSail-D On-Orbit Deployed Configuration

Source [27]: NanoSail-D. (2010). NASA. [Online]. Available: http://www.nasa.gov/sites/default/files/484314main_NASAfactsNanoSail-D.pdf Accessed 24 August 2015.

Another method of exploitation of environmental disturbances is movable appendages such as solar panels to change the aerodynamic drag and torque. For example, the Waseda-Sat 2 (Figure 7) by Waseda University of Japan was designed to use the movable solar panels to change the cross-sectional area and therefore the aerodynamic drag [28]. The goal of that configuration is to use the aerodynamic stability of an object to stabilize about the equilibrium points. Unfortunately, the design was never tested in space, because no communication was established with the CubeSat after the launch.

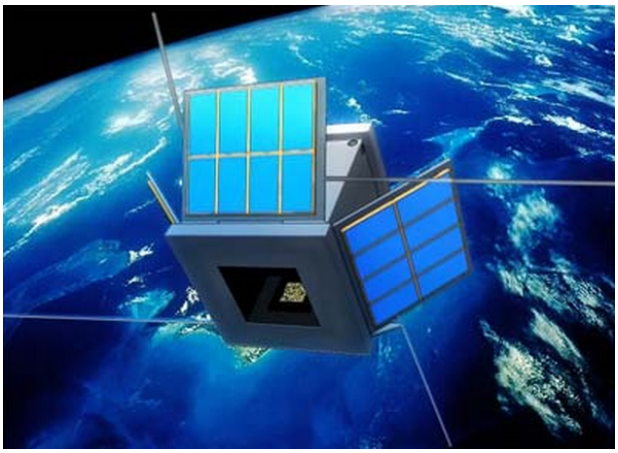

Figure 7. Waseda-SAT-2

Source [28]: T. Miyashita, Waseda satellite project, Waseda University Faculty of Science and Engineering [Online]. Available: http://www.miyashita.mmech.waseda.ac.jp/Waseda-Sat2/missionkei.html. Accessed 24 August 2015.

The last method is the changing the center of mass by shifting masses to adjust the aerodynamic torque as a control torque for attitude stabilization which was proposed by Chesi [3]. In his dissertation, Chesi proposed that by shifting masses in a nanosatellite, the change in center of mass will cause the aerodynamic torque to change in both magnitude and direction. This particular control over the aerodynamic torque, which is the most dominant torque in LEO, may enable the small satellites to withstand the environmental disturbances with their limited size, mass, and power limitations [3]. In this thesis, the shifting masses concept is studied by devising a high fidelity dynamics and simulation environment with a linear control technique.

D. SHIFTING MASSES USE IN ADCS

Finding inexpensive and simple ways to control the attitude of a spacecraft led to different methods such as moving or shifting masses. In the past, those methods involving moving masses were mostly passive. One of the most common passive control technique is the nutation dampers for spinning spacecraft. The objective of using the nutation dampers is to dissipate the kinetic energy of the nutation of a spinning spacecraft so that the angular velocity and the spinning axis can be parallel to each other [29]. There are different types of nutation dampers [18] such as mass-spring dashpot type (Figure 8), blade-mass with fluid (Figure 9), pendulum nutation dampers, ball-in-tube dampers

(impact dampers), and viscous-ring dampers (Figure 10). The selection of the type is made according to attitude and mission characteristics of the specific spacecraft, but the goal is to use the moving masses to stabilize a perturbed motion about the spinning axis.

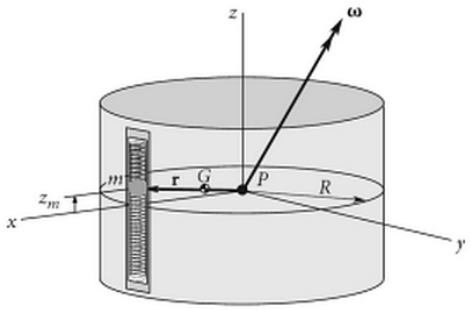

Figure 8. Mass-Spring Dashpot Type

Source [29]: H. Curtis, *Orbital Mechanics for Engineering Students*, Oxford: Elsevier Butterworth-Heinemann, 2005.

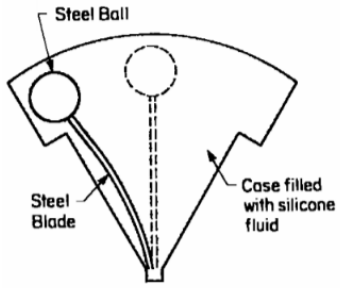

Figure 9. Blade-Mass Nutation Damper with Fluid

Source [18]: P. C. Hughes, *Spacecraft Attitude Dynamics*, Mineola, NY: Dover Publications, 2004.

The other common use of moving masses in attitude control is for vehicles in re-entry phase. Byrne [31], Petsopoulos [32], Rogers (Figure 11) [33], and Robinett [34] studied and demonstrated the use of internal moving mass trim control system for roll control of spinning vehicles. Guo and Zhao also proposed an LQR control method with two moving masses for spinning spacecraft [35].

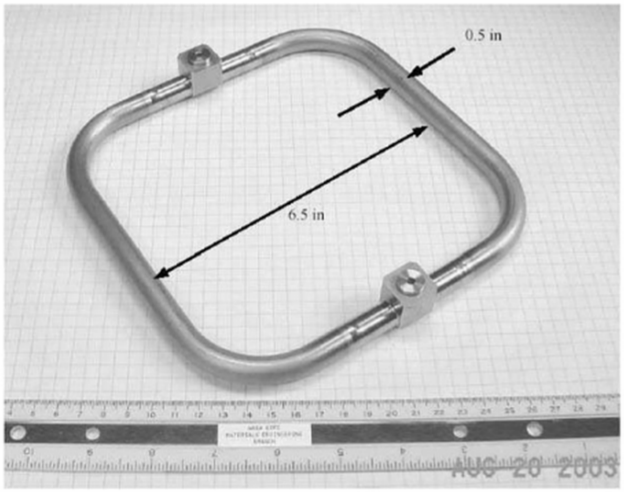

Figure 10. ST5 Viscous Ring Damper by NASA

Source [30]: F. L. Markley and J. L. Crassidis, *Fundamentals of Spacecraft Attitude Determination and Control*, New York: Springer, 2014.

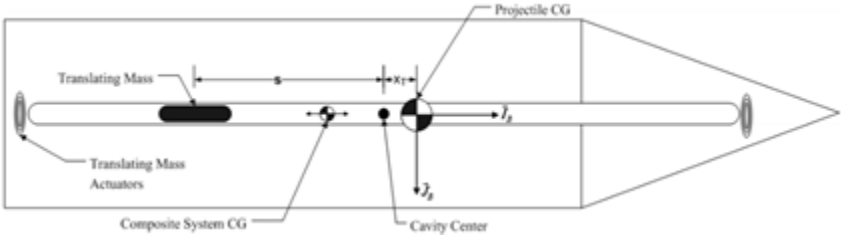

Figure 11. The Variable Stability Projectile

Source [33]: J. Rogers and M. Costello, "A variable stability projectile using an internal moving mass," presented at AIAA Atmospheric Flight Mechanics Conference and Exhibit, Honolulu, HI, 2008.

A recent study about the Mars entry guidance by Atkins [36] also uses two masses to control angle-of-attack and sideslip angles (Figure 12). One of the advantages of the using internal mass re-entry vehicles is that the movements of the masses do not interact with external flow, unlike flaps or ailerons. In addition, internal masses do not change the aerodynamic properties of the vehicle's surface, which is important for precise trajectories [36].

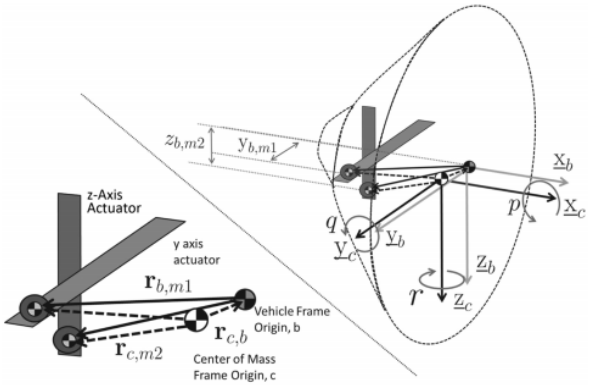

Figure 12. Proposed Method for Angle-of-Attack and Sideslip Angle Control

Source [36]: B. M. Atkins and E. M. Queen, "Internal moving mass actuator control for Mars entry guidance," *Journal of Spacecraft and Rockets,* vol. 52, no. 5, pp. 1294–1310, 2015.

The use of moving masses for attitude control was also studied by researchers for solar-sail spacecraft concepts. The use of a two-axis gimbaled control boom system was proposed to compensate the solar torque disturbances resulting from the difference between the center of mass and the center of pressure [37]. In addition, two shifting masses for pitch and yaw as a solar sail validation mission's primary attitude control (Figure 13) that does not use propellant is studied [38]. A MATLAB-based control toolbox for Solar Sail Spacecraft is also developed which includes moving mass actuators [39].

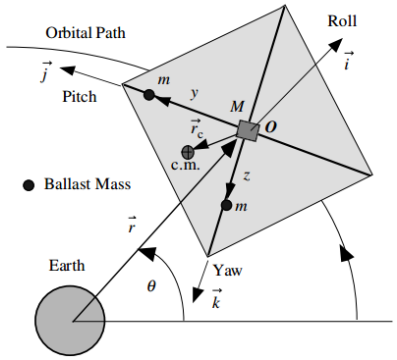

Figure 13. Solar-Sail Spacecraft with Shifting Masses

Source [38]: B. Wie and D. Murphy, "Solar-sail attitude control design for a sail flight validation mission" *Journal of Spacecraft and Rockets,* vol. 44, no. 4, pp. 809–821, 2007.

In 1962, Grubin [40] presented one of the earliest studies of the dynamics of a spacecraft with moving masses. He derived the equations of motion by considering the center of mass of the body without the moving masses as a reference point and gave two simplified application examples in a 2D environment (a point moving mass in one axis and a swiveled rocket engine on a moving vehicle) [40]. Later, Edwards [41] developed the automatic detumbling system with one mass internally moving in one axis. Edwards proposed that a tumbled large spacecraft could be put into a pure spin with one mass (1% of the total mass) in two hours. In this thesis, the papers of Grubin [40] and Edwards [41] are accepted as stepping stones for developing the dynamics model of the spacecraft with shifting masses.

Kumar [42] also proposed an LQR control method for a picosatellite (1U CubeSat in particular) with one moving mass. With only one mass moving in one axis and no disturbance torques, Kumar [42] linearized the three-coupled non-linear differential equations of motion presented in Edwards [41].

In another study, a hybrid control strategy was offered to achieve a full control over the attitude of spacecraft by using two internal movable masses, which provide an under-actuated control in normal operation [43].

All of above references about the moving mass control systems use the inertial properties of the multi-body vehicles to control or stabilize without the use of environmental disturbances. In a recent study by Chesi [3], exploitation of the environmental disturbances was proposed by using the shifting masses. In this thesis, the control logic is based on the exploitation of the aerodynamic torque by changing the center of mass (Figure 14) as it was proposed in Chesi's dissertation.

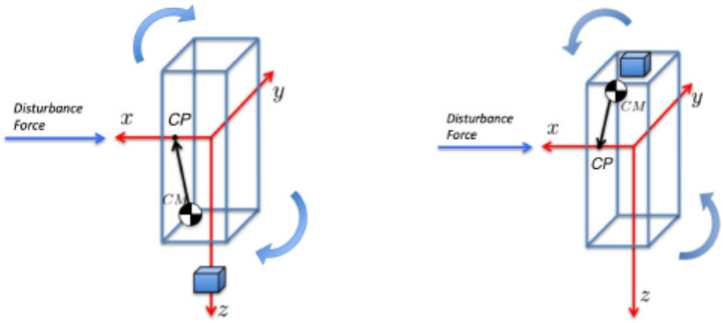

Figure 14. Basic Principle of Harnessing the Disturbance Torque by Changing the Center of Mass

Source [3]: S. Chesi, "Attitude control of nanosatellite using shifting masses," PhD Dissertation, Graduate Division of the University of California, Santa Cruz, CA, 2014.

THIS PAGE INTENTIONALLY LEFT BLANK

II. HISTORICAL SURVEY AND ANALYSIS OF LAUNCHED CUBESAT MISSIONS

Access to space has been always expensive. Both launch and spacecraft costs are high, because they are not reusable and are mostly custom-built. In regard to launch vehicles, companies are trying to develop reusable parts. At this moment, ride-sharing is one of the many ways to reduce the launch cost. On the other hand, the spacecraft have been mostly designed and manufactured in such a way that they are only applicable to one specific mission. Hence, the cost has remained very high. However, COTS components became common in spacecraft designs especially for small satellites. These components caused the drop in development and manufacturing costs.

All of the above explanations about the affordable access to space point to the CubeSat design. With highly standardized bus designs, manufacturers and developers can find almost every component from commercially available products. This affects not only the cost, but development times are reduced to 1–2 years. It is one of the main reasons why CubeSat is brought into the spacecraft technology platform. In addition, standardized CubeSat launchers, which can be mounted on rockets as auxiliary payloads, can deliver multiple CubeSats in one launch such as P-POD [2], NanoRacks [5], NLAS [6], NPSCuL [7], ISIPOD [8], and CSD [9]. More ride-shared payloads lower launch costs.

The drive for CubeSat stemmed from reduced cost and development times, but the trend is changing as many universities and private companies are getting access to space. Since missions became diverse in the last decade, the use and design of the CubeSat have also been transformed. Bigger configurations were introduced to meet more complex mission requirements. More complex subsystems were implemented to accomplish scientific, commercial or military goals. New systems and technologies were tested since the access to space has become cheaper. All of these also affected Attitude Determination and Control System-ADCS. Higher-level missions required more sensitive and accurate attitude control over the CubeSat. These missions determined the complexity level of the ADCS components.

In this thesis, a new attitude control method is investigated. Therefore, a survey of CubeSat missions was conducted to see the trends of the attitude control along with the other features of the missions such as configuration, operational altitude or mission type. In addition, this thesis research aimed to design a prototype model and a mission for the simulations of the proposed attitude control method. One other reason for the CubeSat Mission Analysis is to shape the design of a prototype CubeSat and mission. The results of the analysis will be considered in the prototype design phase.

The attitude control methodology is the focus area of this survey. The scope of the survey also includes the launch date, CubeSat size, operational altitude, pointing accuracy and mission type as auxiliary data. The aim is to categorize attitude control methodologies with respect to those auxiliary data.

A. DATA COLLECTION

Michael Swartwout, Associate Professor at Saint Louis University, is maintaining an active list about the CubeSat missions from the first to the most current [44]. His list contains information about the CubeSat missions. The information is mostly launch- and mission-related along with the categories of size and contractor.

In this thesis, Swartwout's list [44] establishes a baseline. Then, each individual CubeSat mission is studied in order to acquire additional information such as attitude control methodologies, operational altitudes and mission types (Appendix A). The satellite's launch year, name, size, and mission status information are extracted from Swartwout's CubeSat Database [44].

During the survey phase of the study, official web pages or related academic publications of individual CubeSat missions were searched. Moreover, various web-based satellite databases were searched to determine the intended information, attitude control methodology, and for cross-validation of the data [45], [46], and [47].

B. DATA ANALYSIS AND EVALUATION

In the data analysis phase of the survey, all missions are considered individually. They are analyzed according to their launch years, sizes, mission types, and attitude

control methodologies. In addition, cross-relations between different categories are investigated by three-dimensional graphs. All CubeSat missions considered in this study were launched before November 30, 2015.

Among all CubeSat missions, one particular mission affected the tables the most. It is the Flock constellation by Planet Labs [48]. They constitute 32% (131 ea.) of all launched CubeSat missions (408 ea.). They are the largest CubeSat constellation that has ever been launched. Since they have the same design for every CubeSat they launched, one should consider that while interpreting the graph results.

Since 2002, a total of 408 CubeSats have been launched into space. The numbers for CubeSat missions increased a lot in the last three years. Seventy-four percent of all missions were launched in the last three years. The year 2014 was the peak for CubeSat missions with 119 launches (Figure 15).

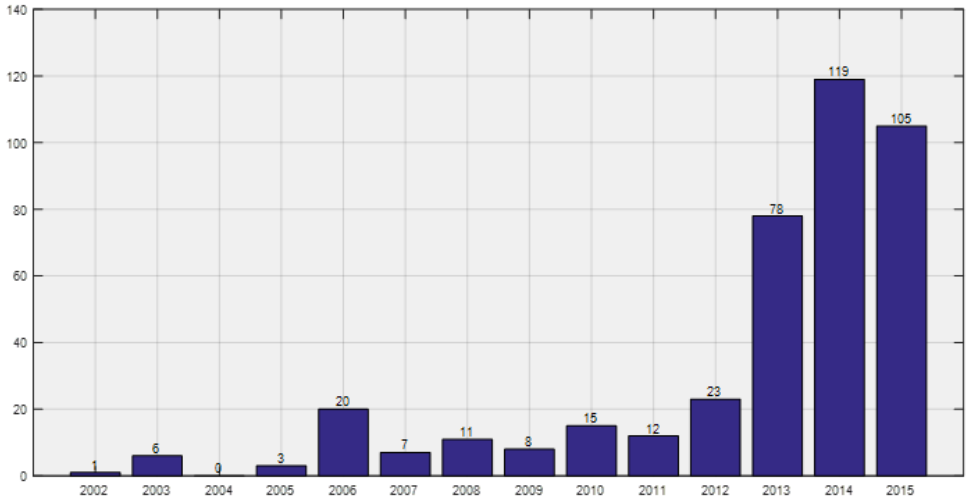

Figure 15. CubeSat Missions with Launch Years

There are six different configurations for CubeSat designs that have been launched up to date. 1U and 3U configurations are the most common types. Eighty-five percent of all CubeSat missions have either an 1U or 3U configuration (Figure 16).

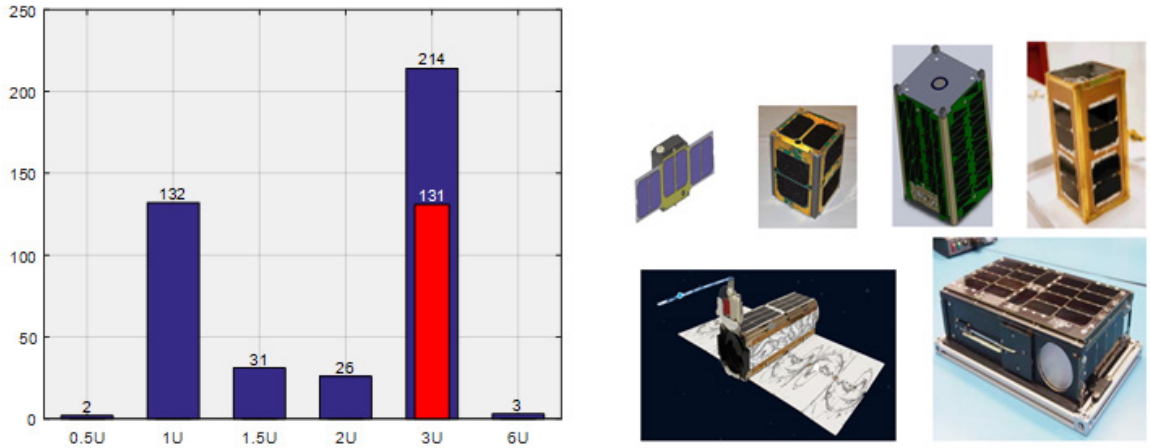

Figure 16. CubeSat Missions with Different Configuration Sizes

On the left, the red bar shows the Flock constellation. On the right, different CubeSat configuration examples, which reached orbit, are given. Adapted from [49], [50], [51], [52], [48] and [53].

Even though the CubeSat design came with the original 1U design, 3U configuration outnumbered (214 ea. to 132 ea.) the 1U configuration in the last two years. The ratio of 3U configuration to all other configurations in the last two years was approximately 3:1 (Figure 17).

In this survey, all missions are divided into five mission types: Technology Demonstration, Scientific, Communication, Earth Observation, and Military. Technology demonstration or validation missions are considered as Technology Demonstration missions even though their missions are for Earth Observation, Communication, or Military. Missions aiming at scientific research on Earth's atmosphere or magnetosphere are classified as Scientific. Earth Observation missions in this survey are only imaging missions. Military missions are classified as Military only if the purpose of the mission is military-related. For example, CubeSat, USS Langley, launched by the U.S. Naval Academy is a Technology Demonstration mission as they are experimenting on hosting a web server from space [54].

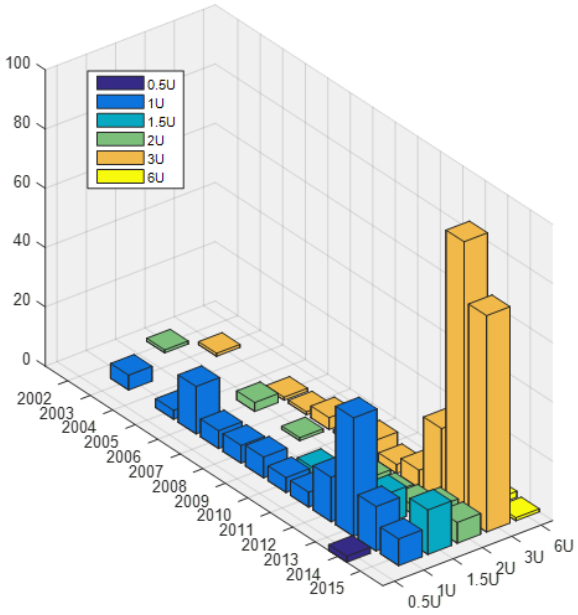

Figure 17. CubeSat Mission Sizes with Launch Years

Following the above definitions, 77.9% of all missions were either Technology Demonstration or Earth Observation (Figure 18). Technology Demonstration missions (39%) are the most common CubeSat missions. These missions offer relatively cheap solutions to validations and experimentations in space along with the educational contributions to undergraduates and postgraduates. Earth Observation missions (38.4%) are the second most common CubeSat missions, mostly due to the Flock Constellation [48]. This large constellation idea with inexpensive assets is one of the main reasons for the rising popularity of CubeSat.

The altitudes of the CubeSat missions are all in LEO limits, which is less than 1000 km. Twenty-nine percent of all missions were at 350–400 km. Only 8% of all missions were below 350 km (Figure 19). One possible explanation for that is the high environmental disturbance torques in low altitudes, which makes it difficult to control the CubeSat. Other reasons may be the lower coverage and shorter lifetime.

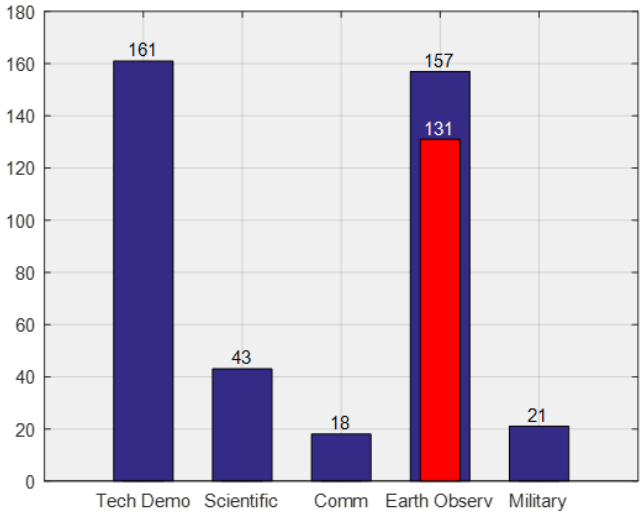

Figure 18. CubeSat Mission Types

The red bar shows the Flock constellation.

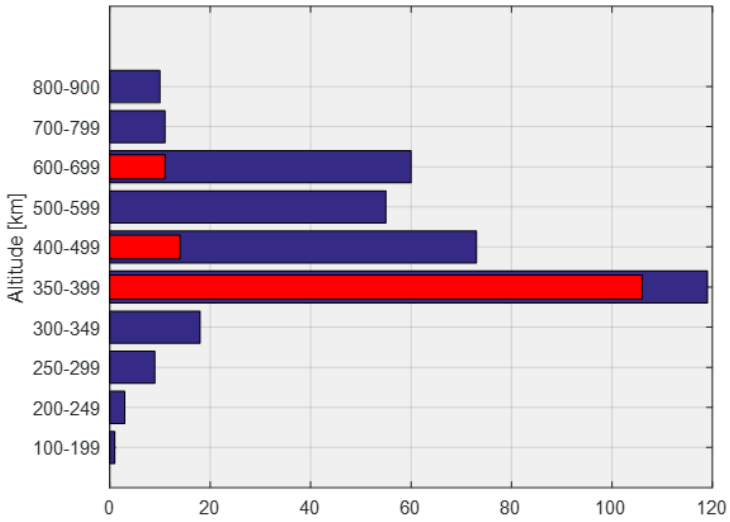

Figure 19. CubeSat Missions with Altitude

The red bars show the Flock constellation.

In regard to attitude control components, the most common method is to use magneto torquers. All CubeSat missions with reaction wheels (41%) also used magneto torquers for momentum dumping. Fifty-four percent of all missions used magneto

torquers. Besides these widespread attitude control methods, there was one CMG application and 13 propulsion experiments. Among the passive control methods, passive magnetic control with permanent magnets and hysteresis rods were the most common method, which formed 13% of all CubeSat missions. As a result, 23% of all missions chose passive or no attitude control while 58% chose the active control method (Figure 20).

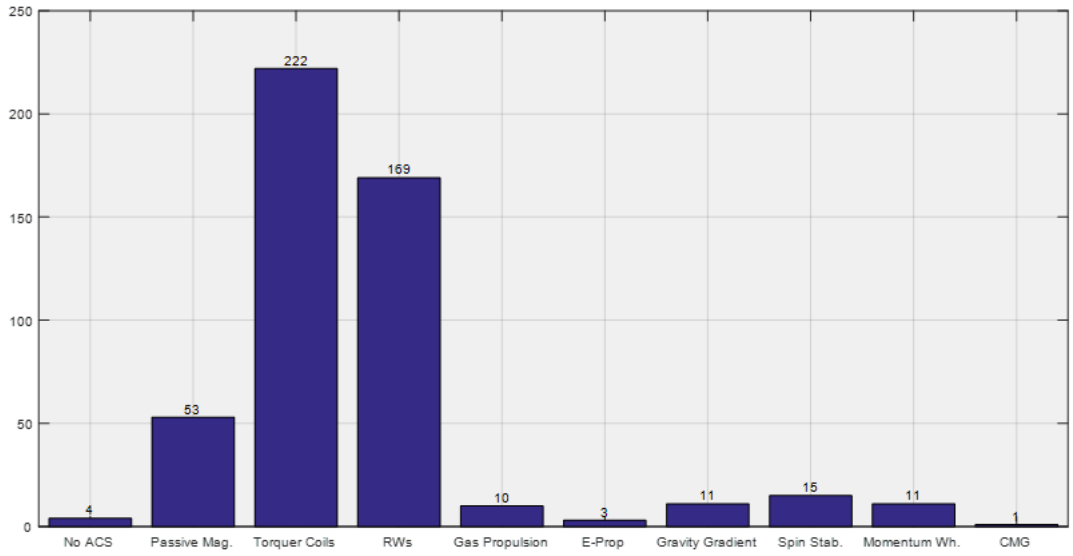

Figure 20. Attitude Control Methodologies/Components for CubeSat Missions

From this point, the relation of attitude control methodologies with other categories will be demonstrated. When we look at the distribution of attitude control methodology from 2002 to 2015 (Figure 21), it can be seen that 87% of all missions with active attitude control came in the last four years. In addition, the increasing trend in active attitude control can be deduced from the ratios of active and passive control methods. The ratio of passive control to active control was 3 to 2 in 2011. However, the ratio changed rapidly after 2011: 3 to 4 in 2012, 1 to 2 in 2013, 1 to 12 in 2014, and lastly 1 to 10 in 2015.

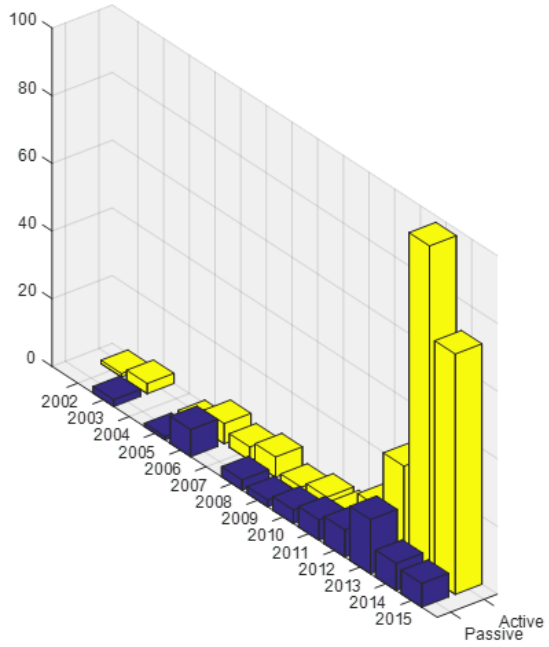

Figure 21. Attitude Control Methodologies with Launch Years

The selection of attitude control methodology also shows dependence on size. While active and passive control methods for 1U configuration were nearly equal in numbers, the 3U configuration had mostly active control methods. Eighty percent of 3U CubeSats used active control (Figure 22).

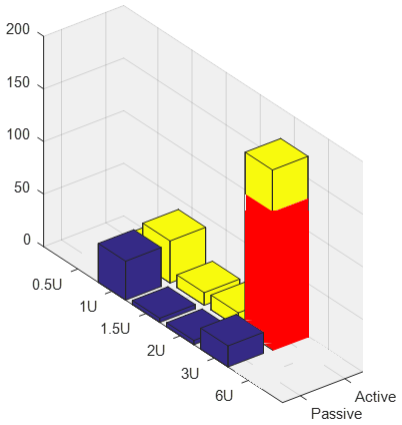

Figure 22. Attitude Control Methodologies with Different Configuration Sizes

The red bar shows the Flock constellation.

The selection trend of the attitude control methodology and the operational altitude are not correlated (Figure 23).

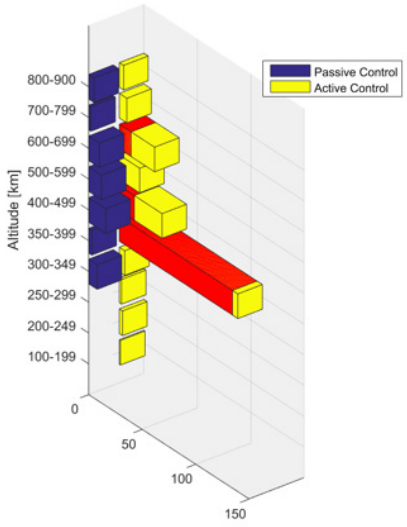

Figure 23. Attitude Control Methodologies wrt Altitude

The red bars show the Flock constellation.

Another factor in attitude control methodology is the mission type. As mentioned earlier, various missions require different attitude control methodologies. Some complex missions may necessitate highly sophisticated attitude control systems while others need simple systems. When we look at the distribution of the attitude control methodologies with respect to different mission types (Figures 24 and 25), Communication and Earth Observation missions provide opposite results. Eighty-nine percent of Earth Observation missions use active control since imaging requirements demand better control over the CubeSat. On the other hand, the ratio of passive to active control is approximately 3 to 1 in Communication missions, because those missions with omni-directional antennas do not need strict attitude control. In addition, scientific missions selected active and passive control methods equally depending on the different mission requirements (Figure 25).

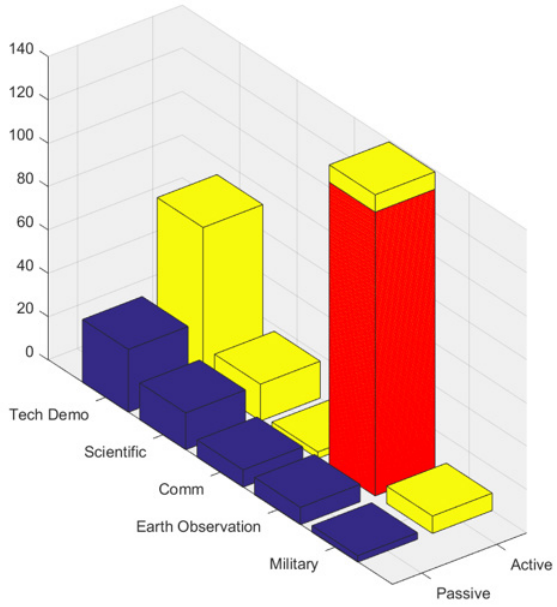

Figure 24. Attitude Control Methodologies with Different Mission Types

The red bar shows the Flock constellation.

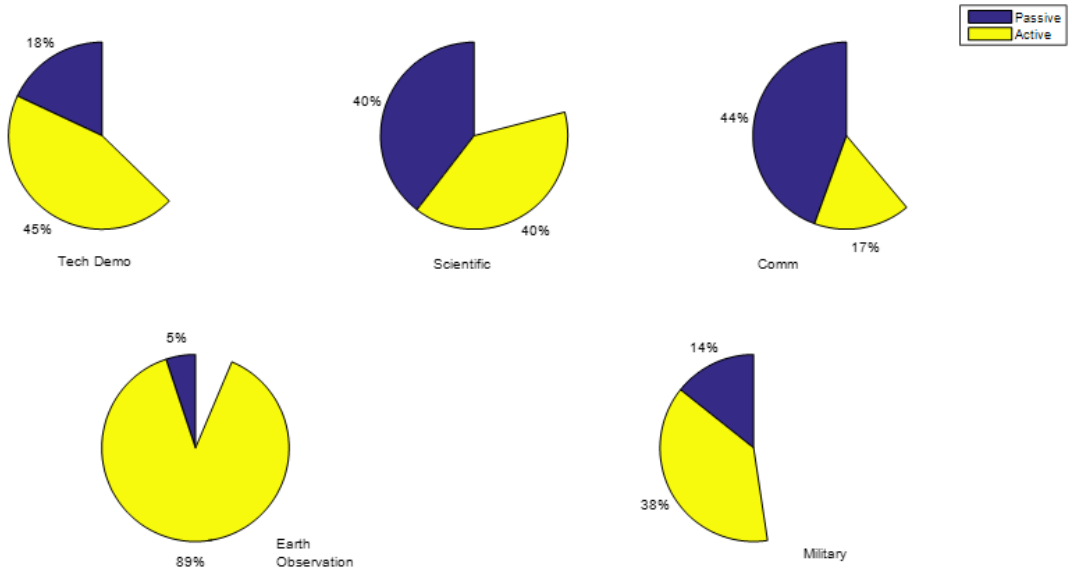

Figure 25. Attitude Control Methodology Selections for Different Mission Types

Finally, the mission status of all missions is presented in Figure 26. The biggest threat to the CubeSat, as for all space missions, is launch failure (21%). Also, lack of communication with the satellite after deployment (16%) is a risk for CubeSat missions. This may be caused by failure of the power or communication system. However, the failure of the ADCS may also eliminate communication. Overall, 51% of all CubeSat missions accomplish either their primary or both primary and secondary goals.

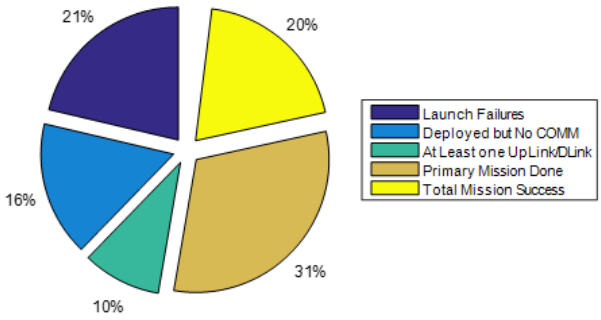

Figure 26. Mission Status

C. FUTURE TRENDS

In evaluating the above data, some trends can be deduced. First, attitude control of future CubeSats will be mostly active. The statistical evidence for this trend is the size, mission type, and year categories. There is an increase in 3U configuration numbers and there will be bigger configurations. As stated before, bigger configurations mostly select the active control method (Figure 22). In regard to mission types, imaging missions are the most promising missions for the CubeSat. The ratio of active control to passive control for Earth Observation missions is 17 to 1 (Figure 25). Lastly, every year the active control percentages have been increasing for CubeSat missions (Figure 21), mostly due to various complex missions demanding better control over the CubeSat. All of the above indicate that active control method selection percentages will increase along with bigger configurations.

The proposed attitude control method in this thesis is also an active attitude control method. Since choosing and designing a prototype model representing the trend is the most appropriate platform to simulate a new attitude control method, a prototype model is designed in the next chapter according to the CubeSat mission analysis in this chapter.

III. PROTOTYPE DESIGN OF A 3U CUBESAT WITH SHIFTING MASSES

In the scope of this thesis, the practicality of the proposed attitude control methodology is investigated. The preliminary design of the prototype CubeSat—named "Shift-Mass Sat"—and its mission are created. This design will provide meaningful and realistic inputs to our model, which will be demonstrated in the next chapter. Rather than giving generic scalar inputs such as mass of the CubeSat and the shifting masses, position of the CoM, orbit altitude, and inclination, it is useful to derive this data from the Shift-Mass Sat design and mission analysis efforts. CubeSat mission analysis is already demonstrated; moreover, the effects of that study will be implemented in this chapter while determining the mission and CubeSat attributes.

In this thesis, the mission of the CubeSat is selected later as an example mission statement. Moreover, the spacecraft design is built upon the preselected attitude control subsystem. In line with the CubeSat component selection trends, Shift-Mass Sat incorporates all of its components from COTS materials. This component selection methodology facilitates the CubeSat development time and mitigates the compatibility issues between subsystems.

Except for the selection of attitude control actuator, all of the components were selected from two online CubeSat component catalogs [55], [56]. There are two main benefits of using online databases for CubeSat component selection. First, one is to compare different types of up-to-date components easily and the second one is to use the 3D model files of the components. The 3D model files provide a more realistic demonstration of the Shift-Mass Sat design, and also a visual test for a volume-constrained environment such as a CubeSat's.

In regard to design boundaries, CubeSat Design Specification (CDS) revision 13 (Appendix B) has been used for limitations and regulations [57]. According to the CDS, CubeSat must conform to specific mechanical, electrical, operational, and testing requirements. In Shift-Mass Sat design, mechanical and electrical requirements were considered. Testing and operational requirements are beyond the scope of this study.

A. MISSION

The mission characteristics shaped the model environment. Since the model is for testing a new attitude control method, the mission of the CubeSat can be any mission that is highly sensitive to pointing accuracy and stabilization. Accordingly, an earth observation mission was chosen for Shift-Mass Sat. As seen in Chapter II, imaging missions constitute 39% of all CubeSat missions (Figure 18). The details of the mission statement are beyond the scope of this study. However, the altitude and the inclination of the orbit will play an important role in Chapter V.

B. ORBIT

To describe a specific orbit, one needs five elements: radius, eccentricity, inclination, argument of perigee, and right ascension of the ascending node (RAAN). Furthermore, to specify the satellite's position the sixth element, which is true anomaly, is needed. In the context of this study, we will neglect the orbital perturbations and choose a circular orbit. Therefore, eccentricity will be zero. In addition, RAAN and the argument of perigee will not be selected nor used.

Altitude and the inclination of the orbit will be the main attention. To see the varying effects of these elements, the mission orbit will not have specific altitude and inclination numbers. Altitude and inclination ranges will be used in the simulation.

Altitude range is derived from Chapter II. Two highly populated altitude ranges of 350–500 and 600–700 km will be used as mission altitudes (Figure 19). In addition to those, 200, 250 and 300 km of altitudes will be added to the simulation to see the control authority of the proposed attitude control methodology in harsh environments (high aerodynamic and gravity gradient torques). The overall operational evaluation of the different altitudes will be performed in Chapter V in terms of mission lifetime, coverage, resolution, pointing errors, settling time, and attitude control authority range.

Inclination range of the orbit is selected from the typical inclinations of the LEO. As an imaging satellite, the sun-synchronous orbit (SSO) inclination angle will be used according to the selected altitude. Polar and equatorial orbit inclinations (90^o and 0^o) will also be used to see the extrema. In addition, International Space Station inclination

(51.6°) and Kennedy Space Center latitude (28.5°) were selected due to their higher launch opportunities. Inclination effect will be implemented to the simulation's results along with the orbit altitude (Table 1).

Table 1. Orbit Altitude and Inclination Ranges

Mission Altitudes (km)	Inclination Angles
200	0°-28.5°-51.6°-90°-SSO
250	
300	
350	
450	
600	

C. CUBESAT SUBSYSTEM COMPONENTS SELECTION

The components for the design were selected from COTS options for each subsystem. The compatibility of the selections within each other was considered.

1. Payload

The CubeSat mission was selected as an imaging mission. Therefore, the payload is an imaging camera. NanoCam C1U from GOM Space (Figure 27) was selected due to its compact size and mass properties and high compatibility features with CubeSat structures. Features of the NanoCam C1U [58] are listed in Table 2.

Figure 27. NanoCam C1U

Source [58]: *NanoCam C1U datasheet.* (2011). GOMSPACE. [Online]. Available:http://gomspace.com/documents/GS-DS-NANOCAM-6.2.pdf. Accessed 12 October 2015.

Table 2. NanoCam C1U Features

Feature	Value	Unit
Focal Length	35	mm
F-number	1.9-16	
Spectral Transmission	400-1000	nm
Field of View	9.22	deg
Power (Idle-Image Acq.-Image Process)	360-634-660	mW
Mass	166	g
Price	11500	€

Adapted from [58]: *NanoCam C1U datasheet*. (2011). GOMSPACE. [Online]. Available:http://gomspace.com/documents/GS-DS-NANOCAM-6.2.pdf. Accessed 12 October 2015.

2. Power

In order to provide electrical power to the CubeSat during sunlight and eclipse portions of the orbit, solar panels and batteries were selected along with a power control board.

NanoPower P110 Series Solar Panels (Figure 28) from GOM Space were selected. The main reason for the Solar Panel selection is the built-in features of the NanoPower P110 series. Solar Panel comes with Sun Sensors, Temperature Sensors, Magnetorquers and Gyroscopes. Six solar panels will be used in the Shift-Mass Sat with the embedded ADCS attributes (P110UC model), and four solar panels will be used without ADCS features (P110C Model). Features of a single solar panel [59] are listed in Table 3. Attributes of the embedded ADCS components will be shown in the ADCS section.

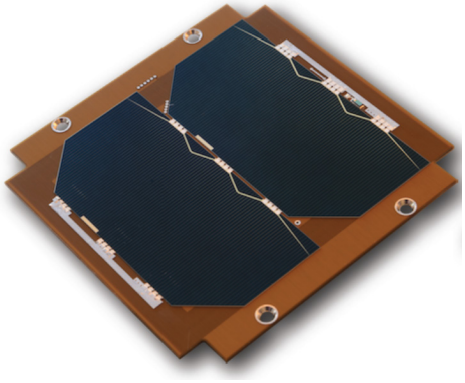

Figure 28. NanoPower P110 Series Solar Panel

Source [59]: *NanoPower P-110 series solar panels datasheet*. (2013). GOMSPACE. [Online]. Available: http://gomspace.com/documents/GS-DS-P110-1.0.pdf. Accessed 12 October 2015.

Table 3. P110 Series Solar Panel Features

Feature	Value	Unit
Solar Cell Assy.	GaInP/GaAs/Ge	Triple Junction
Efficiency	30%	
Effective Cell Area	60.36	cm^2
PCB Thickness	1.6 (P110UC) 1.1 (P110C)	mm
Mass	65 (P110UC) 29 (P110C)	g
Voltage	4.64-4.84	V
Power	2270-2400	mW
Power Consumption due to embedded ADCS	0.31 (P110UC) 2.5×10^{-3} (P110C)	W
Price	2750	€

Adapted from [59]: *NanoPower P-110 series solar panels datasheet*. (2013). GOMSPACE. [Online]. Available: http://gomspace.com/documents/GS-DS-P110-1.0.pdf. Accessed 12 October 2015.

For batteries, a combined component QuadBat BP4 V2.0 was selected (Figure 29) due to its high compatibility features with P110 series solar panels and built-in power board option P31u. According to the CDS, total stored chemical energy must not exceed 100 W-h in CubeSat [57]. The batteries model, which was selected for this design, conforms to that upper boundary with a 38.5 W-h maximum stored energy [60]. The other features are listed in Table 4.

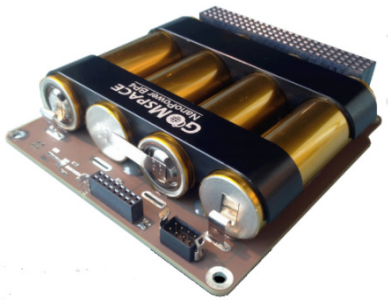

Figure 29. QuadBat BP4 V2.0

Source [60]: *NanoPower BP series datasheet*. (2014). GOMSPACE. [Online]. Available:http://gomspace.com/documents/gs-ds-bp4.pdf. Accessed 12 October 2015.

Table 4. QuadBat BP4 Features

Feature	Value	Unit
Batteries Config.	2 parallels+2 series	
Capacity	38.2	W-h
Voltage	6-8.4	V
Current	5.2	A-h
Mass	240	g
Price	2450	€

Adapted from [60]: *NanoPower BP series datasheet*. (2014). GOMSPACE. [Online]. Available:http://gomspace.com/documents/gs-ds-bp4.pdf. Accessed 12 October 2015.

3. Communication and Command

NanoCom ANT430 omnidirectional CubeSat antenna from GOM Space (Figure 30) was selected for the communication subsystem. The antenna is compatible with CubeSat specifications and other COTS components for communication subsystem. The features of the antenna are listed in Table 5 [61].

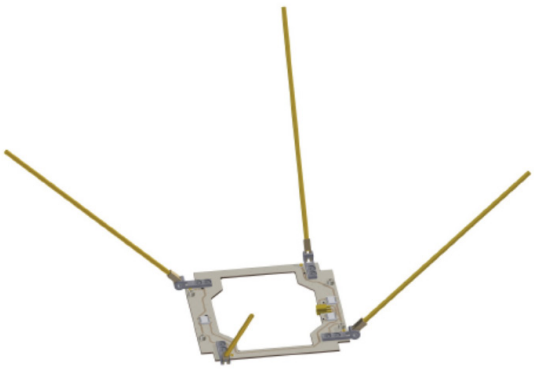

Figure 30. NanoCom ANT430 Omnidirectional Antenna

Source [61]: *NanoCom ANT430 datasheet*. (2014). GOMSPACE. [Online]. Available:http://gomspace.com/documents/GS-DS-NANOCOM-ANT.pdf. Accessed 12 October 2015.

Table 5. Antenna Features

Feature	Value	Unit
Frequency Range	400-550	MHz
Bandwidth @435 MHz	5	MHz
Input RF Power	10	W
Mass	30	g
Price	5500	€

Adapted from [61]: *NanoCom ANT430 datasheet*. (2014). GOMSPACE. [Online]. Available:http://gomspace.com/documents/GS-DS-NANOCOM-ANT.pdf. Accessed 12 October 2015.

NanoCom AX100 from GOM Space (Figure 31) was selected to communicate with a configurable VHF/UHF transceiver. This particular component was selected due to its compatibility features, long-range half-duplex configurable transceiver, and on-orbit frequency and filter-bandwidth configuration attributes [62]. The features of the transceiver are listed in Table 6.

Figure 31. NanoCom AX100 Transceiver

Source [62]: *NanoCom AX100 datasheet*. (2015). GOMSPACE. [Online]. Available:http://gomspace.com/documents/gs-ds-nanocom-ax100-1.7.pdf. Accessed 12 October 2015.

Table 6. NanoCom AX100 Features

Feature	Value	Unit
Data Rates	0.1-115.2	kbps
Output TX Power	30	dBm
Mass	24.5	g
Price	6500	€

Adapted from [62]: *NanoCom AX100 datasheet*. (2015). GOMSPACE. [Online]. Available:http://gomspace.com/documents/gs-ds-nanocom-ax100-1.7.pdf. Accessed 12 October 2015.

4. Onboard Computers

Since all of the subsystem components need an interface and a processor, highly compatible onboard computer selection is justified. Thus, NanoMind A712D from GOM Space (Figure 32) was selected as the flight computer for Shift-Mass Sat. This particular model has embedded 3-axis magnetometer [63]. NanoMind A712D can process the CubeSat health and status information, and provide control input to relevant components with an ARM7 processor. The mass of the daughterboard is 55 g and the price of the component is €4,750 [56]. The features of the NanoMind A712D in relation to the ADCS will be explained in the ADCS section.

Figure 32. NanoMind A712D Flight Computer

Source [63]: *NanoMind A712D datasheet*. (2015). GOMSPACE. [Online]. Available:http://gomspace.com/documents/gs-ds-nanomind-a712d-1.5.pdf. Accessed 12 October 2015.

To carry the daughterboard, the NanoDock Motherboard DMC-3 model from GOM Space (Figure 33) was selected. This particular model can carry four daughterboards. The mass of the motherboard is 51 g and the price is €3000 [64].

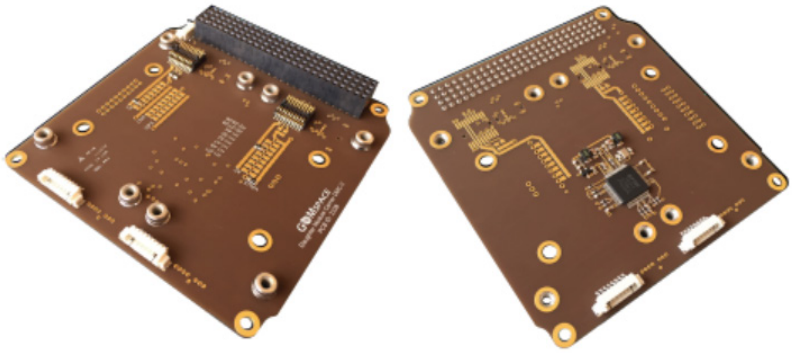

Figure 33. NanoDock Motherboard DMC-3

Source [64]: *NanoDock motherboard DMC-3 datasheet*. (2015). GOMSPACE. [Online]. Available: http://gomspace.com/documents/gs-ds-nanodock-motherboard-dmc-3-1.3.pdf. Accessed 12 October 2015.

In the Shift-Mass Sat design, the example daughterboard configuration demonstrated by GOM Space (Figure 34) is going to be used [64]. The NanoMind A712D Flight Computer and NanoCom AX100 Transceiver will be mounted on top. At the bottom, the OEM615 GPS receiver, from NovAtel, which costs $6495, will be

mounted. The selected GPS receiver's mass is 24 g and the power consumption is less than 1 watt [65].

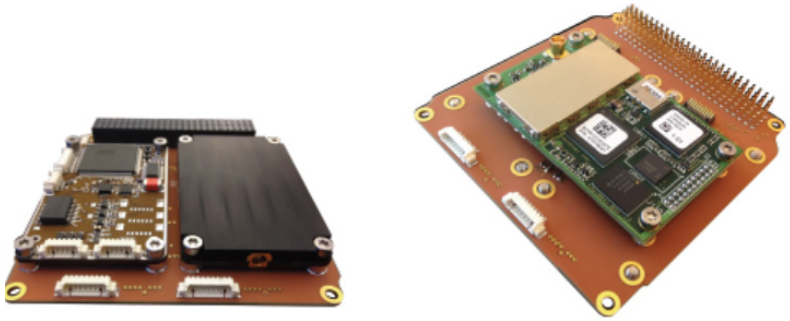

Figure 34. Motherboard Configuration

Source [64]: *NanoDock motherboard DMC-3 datasheet*. (2015). GOMSPACE. [Online]. Available: http://gomspace.com/documents/gs-ds-nanodock-motherboard-dmc-3-1.3.pdf. Accessed 12 October 2015.

5. Structure

The CubeSat configuration was selected a 3U CubeSat, which is the most common configuration with 52% of all configuration sizes (Figure 16). For the structure of the Shift-Mass Sat design, a 3-Unit CubeSat Structure from ISIS (Figure 35) was selected due to its smooth compatibility features with the selected subsystem components. The total mass of the structure is 550 g and the price is €3,650 [66].

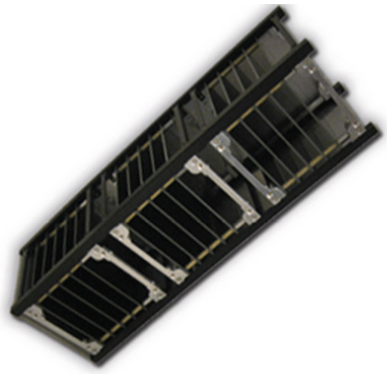

Figure 35. 3-Unit CubeSat Structure

Source [66]: *3-Unit CubeSat structure*. (2015). ISIS. [Online]. Available: http://cubesatshop.com/ index.php?page=shop.product_details&flypage=flypage.tpl&product_id=4&category_id =1&option=com_virtuemart&Itemid=66. Accessed 12 October 2015.

6. ADCS

The main purpose for the design is to simulate a realistic prototype CubeSat design with a novel attitude control methodology. Shifting masses will be used to exploit aerodynamic torque by changing the moment arm between the CoM and CoP. These linearly actuated shifting masses can be custom-built. However, COTS materials are also used for shifting masses to demonstrate the current applicable technology to the proposed method. Before giving the shifting masses component selection's details, the other parts of the ADCS will be explained.

As noted for previous subsystems, some of the ADCS components have already been introduced. Sun Sensors, Gyroscopes and Magnetorquer will be embedded with Solar Panels [59]. A 3-axis Magnetometer will be mounted on a NanoMind A712D flight computer [63]. Since the proposed attitude control methodology aims for better than 1-degree accuracy, attitude knowledge should be more accurate. Therefore, along with the Sun Sensors, one pair of Static Earth Sensors and a Star Tracker are added to the ADCS.

The Static Earth Sensor from Maryland Aerospace (Figure 36) was selected to increase the attitude knowledge accuracy and consistency. The sensor is capable of providing attitude knowledge during both sunlight and eclipse portions of the orbit with four thermopile detectors looking at Earth, dark space, and the disk of Earth, and sensing the angle due to the horizon. Two orthogonal sensors are needed to come up with the nadir vector information in body triad [67].

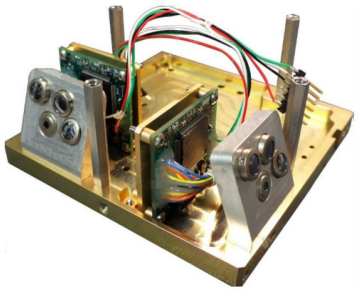

Figure 36. Maryland Aerospace Inc. Static Earth Sensor (MAI SES)

Source [67]: *MAI SES product specification*. (2014). Maryland Aerospace Inc. [Online]. Available:http://d6110363.ozt807.onezerotech.com/wp-content/uploads/2015/08/MAI-SES-Specifications-20150827.pdf. Accessed 12 October 2015.

Star Tracker from Maryland Aerospace (Figure 37) was selected for the higher accuracy in attitude knowledge: 0.013 degrees [68]. Moreover, the sensor requires less than 1 watt for power.

Figure 37. MAI-SS Space Sextant

Source [68]: *MAI-SS space sextant*. (2015). Maryland Aerospace Inc. [Online]. Available:http://cubesatshop.com/ index.php?page=shop.product_details&flypage=flypage.tpl&product_id=130&category_id=7&option=com_virtuemart&Itemid=69. Accessed 12 October 2015.

The 35000 series size 14 non-captive stepper motor from Haydon Kerk Motion Solutions (Figure 38) was selected for actuating the shifting masses [69]. The main parameters that affected the selection decision are the moving motor, power consumption, mass, and useful stroke length.

Figure 38. 35000 Series Size 14 Non-Captive Stepper Motor

Source [69]: *35000 series size 14 stepper motor linear actuators*. Hayden Kerk Motion Solutions.[Online].Available:http://www.haydonkerk.com/LinearActuatorProducts/ StepperMotorLinearActuators/LinearActuatorsHybrid/Size14LinearActuator/tabid/77/ Default.aspx#stepper_motor_linear_actuator_noncaptive. Accessed 12 October 2015.

Some linear actuators in the market move the piston, screw, or the rail; however, those methods come with a static motor, which is actually a mass burden to the CubeSat.

Therefore, non-captive stepper motors provide the most weight-efficient solution to our problem by moving the motor along the screw. In this case, the shifting mass becomes simply the motor itself.

Moreover, COTS linear actuators are mostly designed for ground applications with a relatively high input power opportunities and applicable massive motor selections. Unfortunately, CubeSat is a mass, volume, and power constrained platform. In regard to these three parameters, a 35000 series size 14 non-captive stepper motor from Haydon Kerk Motion Solutions has viable values with relatively low power consumption and optimum weight and volume.

Finally, the useful stroke length of the 35000 series size 14 non-captive stepper motor is applicable to the Shift-Mass Sat model with the small stepper motor width and length.

In addition, the control of the shifting masses' stepper motors is governed by onboard software. The NanoMind Flight computer will be responsible for processing the software and generating the outputs for the motors.

Even though the roll axis actuator in the Shift-Mass Sat design is the magnetorquer, for comparison purposes a reaction wheel is used in the simulation. This configuration uses the Microsatellite Reaction Wheel (-0.060-) by Sinclair Interplanetary (Figure 39). This particular model has 60 mNm-s nominal and 120 mNm-s peak angular momentum capacity at 6500 rpm, 20 mNm peak torque capability, and 0.5 W nominal and 23.4 W peak power consumption [70].

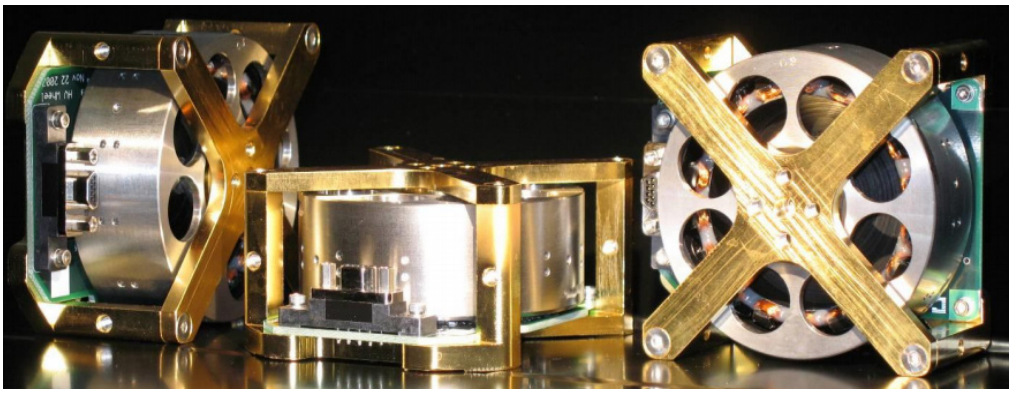

Figure 39. Microsatellite Reaction Wheel

Source [70]: *Sinclair Interplanetary—Reaction Wheels*. (2015). Sinclair Interplanetary. [Online]. Available: http://www.sinclairinterplanetary.com/reactionwheels. Accessed 27 November 2015.

In regard to overall operation concept of the ADCS, Star Tracker is the main attitude-sensing element. Since it will exhibit some discontinuities during its operation due to excessive angular rate, or sun or moon exposure, sun sensors and horizon sensors along with the 3-axis magnetometer will provide attitude information. The gyroscope will provide the angular rates. With the attitude knowledge acquired, shifting masses supplemented with magnetorquers will control the attitude. Since shifting masses control is under-actuated, the magnetorquer is essential to have a full authority over the attitude control of Shift-Mass Sat. In this thesis, the simulation model will study the control segment only. Attitude determination is considered as granted by fully operational sensors. The details of the attitude determination is beyond the scope of this study.

The characteristics of all ADCS components are listed in Table 7.

Table 7. ADCS Components Characteristics

Component	Feature	Value	Unit
Sun Sensor	Current	930	µA
	Cosine Error	1.85-3.5	deg
Gyroscope	Range	80	deg/s
	Sensitivity	0.00458	deg/s
	Voltage	5	V
	Current	44	mA
Magnetorquer	Area	1.55	m^2
	Resistance	120-150	Ohm
	Dipole Momentum at 3.3V	0.034-0.043	$A\text{-}m^2$
Magnetometer	Field Range	-4–4	Gauss (G)
	Measurement Time	10	s
	Resolution	7	mG
IR Earth Sensor	Coarse Field of View	60	deg
	Resolution for coarse FOV	1	deg
	Fine Field of View	7	deg
	Resolution for fine FOV	0.25	deg
	Voltage	3.3	V
	Current	40	mA
	Mass	33	g
	Price	14,900	$
Star Tracker	Accuracy	0.013	deg
	Acquisition time (lost in space)	0.03	s
	Acquisition time (tracking)	0.005	s
	Max tracking rate	1	deg/s
	Update Rate	4	Hz
	Voltage	3.3	V
	Peak Current	0.303	A
	Mass	91	g
	Price	32,500	$
Shifting Mass Linear Actuator	Power Consumption	5.7	W
	Operating Voltage	5	V
	Velocity	10-50	mm/s
	Resolution	0.048	mm
	Useful Stroke Length	70	mm
	Mass	162	g
	Price	125	$
Reaction Wheel	Momentum (nominal/peak)	0.06/0.12	mNm-s
	Torque (peak)	20	mNm
	Dimensions	77x65x38	mm
	Mass	226	g
	Supply Voltage	7.5-34	V
	Power (nominal/peak)	0.5/23.4	W

Adapted from [59], [63], [67], [68], [69], and [70].

D. 3D MODEL AND PLACEMENT OF THE COMPONENTS

As stated, it is crucial to test the placement of the components visually in volume-constrained environments like CubeSat. Therefore, 3D model ".step" files of each component are used to construct Shift-Mass Sat (Figure 40).

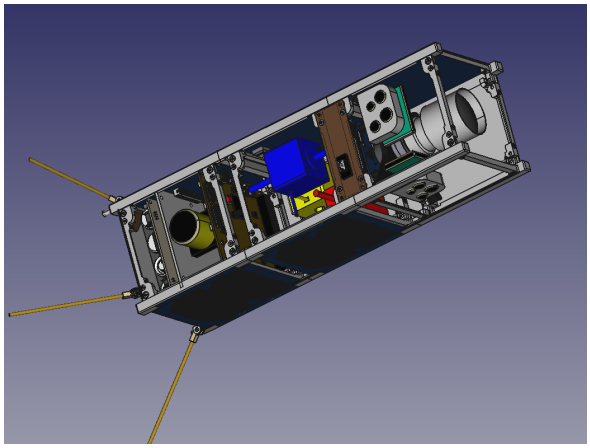

Figure 40. 3D Model of Shift-Mass Sat

Except for the horizon sensors, star tracker, and the shifting masses, all other components' 3D model files are already provided by online catalogs. The remaining components' 3D model files were created from their technical drawings and colored according to their published images. An overview of the components of Shift-Mass Sat is illustrated in Figure 41, and a 3D animation is embedded in Figure 42.

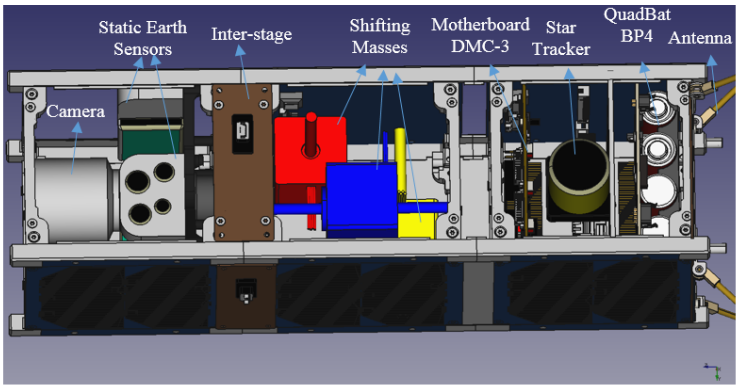

Figure 41. Overview of the Subsystems

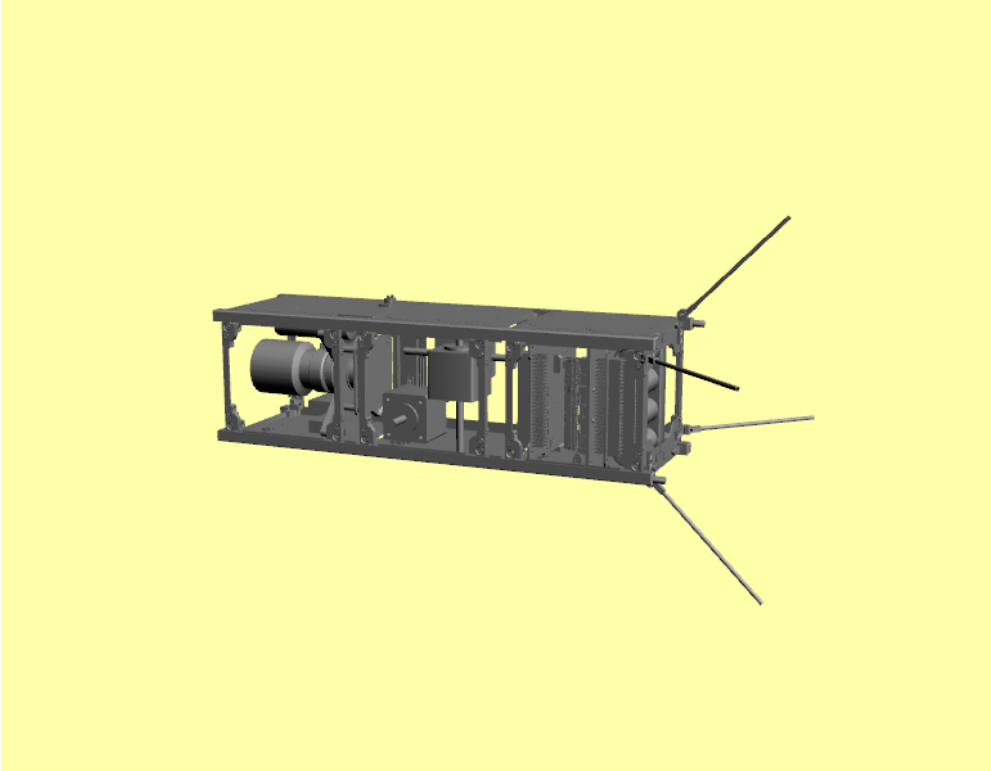

Figure 42. 3D Animation of Shift-Mass Sat[1]

Additionally, shifting masses are colored to distinguish the axes they are assigned to: red for the x-axis, yellow for the y-axis, and blue for the z-axis (Figure 43). All these axes are in the body triad that is aligned with the orbital triad at the desired end state.

[1] At the time of publication, it was necessary to download the document in order to view the 3D animation.

To activate the 3D animation, left-click on the image. There will be a warning, "3D content has been disabled. Enable this feature if you trust this document." Click the "Options" then select "Trust this document one time only."

Now when you click on the image, the image will activate. It may take a few seconds. Once activated, click and hold on the image to rotate, using your mouse wheel to zoom in and out.

(We inserted this 3D animation into the PDF by exporting the CAD model in mesh format and then converting it to .u3d format using MeshLab software.) Adobe Acrobat software version 7.0 or later is needed for full capability. Different versions of Acrobat may have different steps than outlined here.

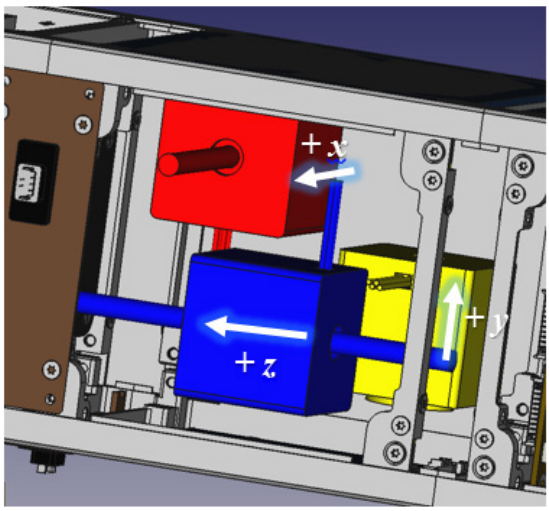

Figure 43. 3-axis Shifting Masses Linear Actuators

E. MASS BUDGET

One aim of the prototype design is to show the range authority of the center of mass with the shifting masses. We need the positions and masses of the individual components. With that information, which are given from the datasheets and the 3D placement design, the center of mass relative position with respect to the geometric center of the CubeSat and the inertial properties are easily calculated under the process named as mass budget.

According to the CDS [57], the maximum allowable mass for a 3U CubeSat is 4 kg. Shift-Mass Sat has 3.1 kg with a 25% margin that conforms to design specifications. In addition to the mass property, CDS [57] has a boundary on the distance between CoM and the geometric center. CDS dictates that the distance shall not exceed 20 mm in x- and y-axes and 70 mm in the z-axis (red cylinder in Figure 44).

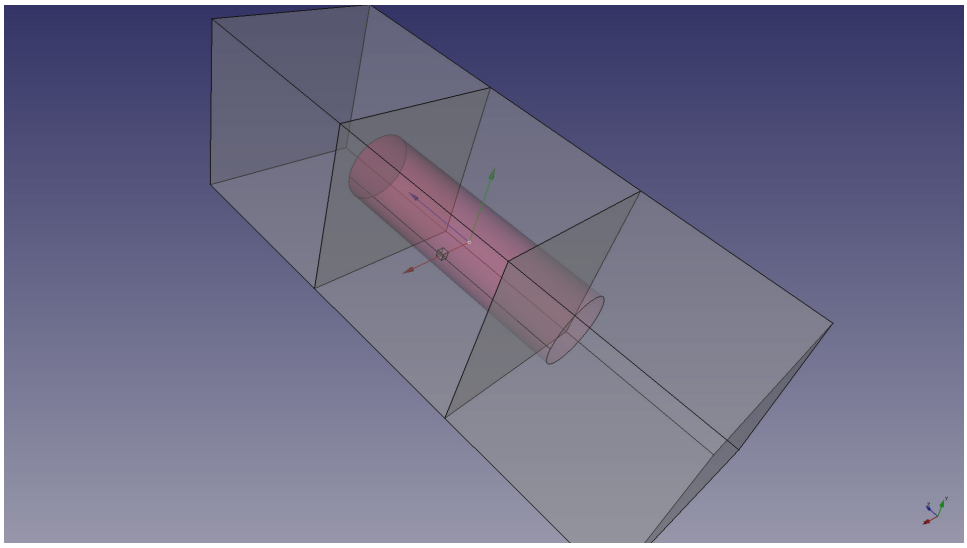

Figure 44. Center of Mass Location Design Specification

The red cylinder is the allowable envelope for the CoM of the CubeSat dictated by the CubeSat Design Specifications: ±2 cm in x- and y-axes, ±7 cm in z-axis.

According to Shift-Mass Sat mass budget calculations, CoM distance from the geometric center is [18.41; -0.4; 0.73] in mm, which is within the specification limits (Figure 45).

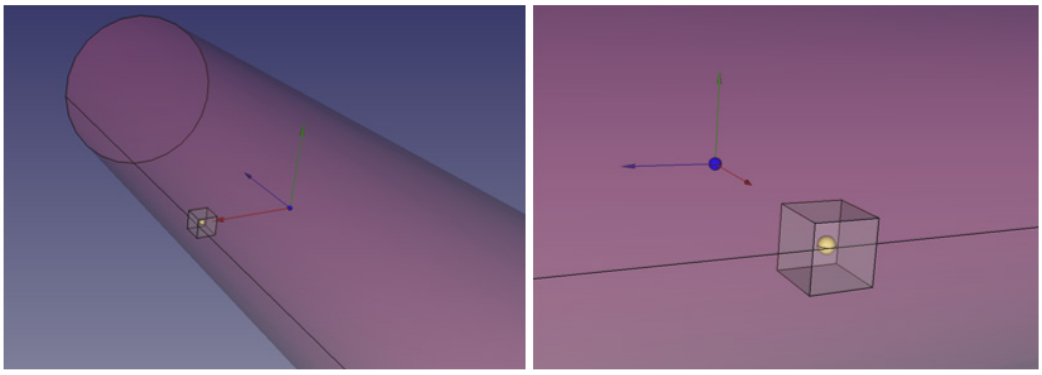

Figure 45. Center of Mass Location within the Design Specification Space

The blue sphere represents the CoP that is at the geometric center. The yellow sphere represents the CoM that is well within the design specification space illustrated by the red cylinder. The cube around the CoM represents the authority of the shifting masses that changes the location of the CoM. The change envelope of the CoM's position by shifting masses is illustrated with a 3.64 mm cube.

With the selected mass ratio between the shifting masses and the total mass in the prototype design, the CoM location range is also illustrated in Figure 45. The ratio in this case will be considered as the nominal ratio, which will be further investigated in the Chapter V for different values. The nominal mass ratio is 5%. Based on the nominal mass ratio, the change in CoM in every axis is ± 1.82 mm. The cube, an illustration of the range, is demonstrated in Figure 45.

In regard to the inertial properties, Shift-Mass Sat design gives more realistic inertial values for the simulation model. Rather than assuming the 3U CubeSat as a homogeneous rectangular prism, considering the positions of each component gives relatively more realistic inertial values. In Shift-Mass Sat, inertial values are listed in Table 8.

Table 8. Inertial Values

Principal Axis	Inertial Value	Units
I_{xx}	0.0059	[kg-m^2]
I_{yy}	0.0009	
I_{zz}	0.0168	

F. OUT-OF-SCOPE DESIGN ATTRIBUTES

This thesis mainly focuses on modeling a new attitude control method and the evaluation of its performance and the practicality in the areas of mission and design. To supplement the simulation model, launched CubeSat mission data analysis was performed and a prototype design of a 3U CubeSat has been demonstrated. However, the detail of the design is at such a level that it gives credible and practical information about the CubeSat for the simulation model. The inertial and mechanical attributes of the shifting masses and the CubeSat as the whole system will be implemented in the software in order to represent the real-world application. Even though the cost was not considered during the design and component selections, Shift-Mass Sat's cost can be calculated with individual component prices and a 20% margin, which results in $150,000.

There are out-of-scope areas that have not been fully investigated by this thesis. The most important out-of-scope design attributes are explained below.

1. Power Budget

CubeSat is a very constrained design platform especially in terms of mass, volume, and power. As discussed, in terms of mass and volume, the Shift-Mass Sat design is well within limitations. The power budget, on the other hand, shows some out-of-boundary outputs due to the shifting mass actuator selection. The power generated by solar panels, assuming that 40% of the panels are exposed to sunlight due to geometry, is 9 watts for typical and 9.6 watts for maximum. The value can be increased with the battery usage to 20 watts for shorter-period-of-time operations that need high power such as the movement of the shifting masses. Again, this power deficit will be present whenever the peak use of the shifting masses is demanded.

The selection of the shifting masses was done to show that commercially available shifting masses actuators can be fit into the CubeSat volume space and within the mass limitations. Also, the supply voltage of the selected actuator is 5 volts, which is achievable. However, the peak power consumption per one actuator is 5.7 watts. This relatively high power requirement is due to the primary design of the COTS material. These actuators are built to move some weights attached to them, not only the motor itself. This particular stepper motor has a force capability reaching 250 N, which is way over for our purposes. Hence, a custom built actuator can be designed for this mode of operation with less force capability and less power consumption, eventually. This is out-of-scope of this study, but it is predicted that the new design of the actuator may solve the power budget issue.

In addition, more advanced solar panels can be designed such as deployable ones in the “Space Dart” concept [71]. With that design, more power can be generated to compensate for the power deficit.

In summary, the detailed power budget and the solutions that may be implemented to overcome the deficit in power requirements are out of scope of this thesis.

2. Attitude Determination and Sun Exclusion

In this thesis, the attitude determination components are selected in consideration of the goal of achieving below 1 degree of control accuracy. To achieve that goal the attitude determination concept and its components should be more accurate. That is the reason of including star trackers (0.013^{o} accuracy) and horizon sensors ($0.25\text{-}1^{o}$ resolution) to the system along with the sun sensors (3^{o} of cosine error), magnetometers (7 mG resolution), and gyroscopes (0.0045^{o}/s accuracy).

The design of the attitude determination concept is out of scope of this study. It is assumed that the absolute accuracy of attitude and its rate is well known from the robust attitude determination hardware and software.

In addition, the sun exclusion maneuvers for the star tracker are out of the scope of this study. The model of the attitude control will only be emphasized on the stabilization of the CubeSat about the nadir-fixed pointing alignment for the imaging mission.

IV. MODELING OF THE PROPOSED ATTITUDE CONTROL METHOD

Up to this point, launched CubeSat missions have been investigated and a prototype CubeSat design has been proposed with key mission attributes. All of the work up to this chapter was done to simulate the environment and space platform in a practical and realistic manner. The parameters that are related to the spacecraft and its orbit will be brought from Shift-Mass Sat and mission design, which are constructed based on CubeSat mission analysis.

An accurate and realistic simulation model is described in this chapter. A closed-loop control methodology will be implemented to achieve modern state-space control over the spacecraft with the proposed attitude control methodology. The model overview is illustrated in Figure 46. Each block in the overview will be explained in this chapter.

MatLab and Simulink have been used as the software to model and run the simulation [72]. The results of various numerical examples will be evaluated in Chapter V.

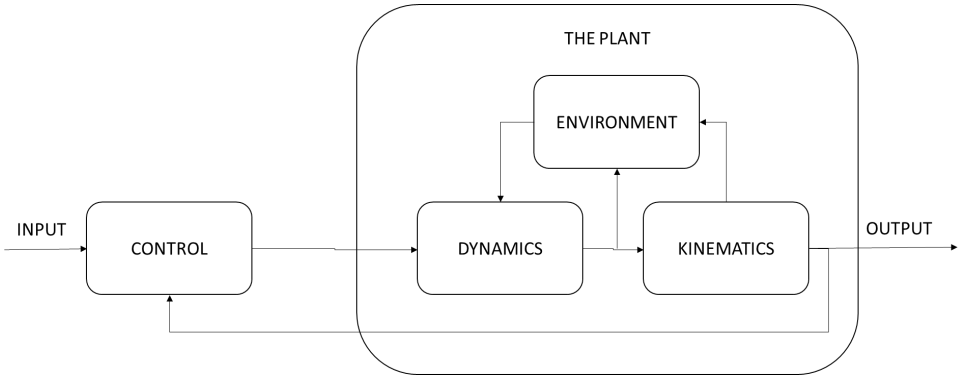

Figure 46. Overview Block Diagram of the Model

A. REFERENCE TRIADS

Before the model demonstration, it is useful to explain the reference triads that are used in this study. It is essential to be careful about the reference triads and the

transformation from one to another, since rotational mechanics equations may change from one reference triad to another. For example, if an angular acceleration in a rotating triad (i.e. Orbital or Body Triad) is under study, one should add the relative acceleration terms with respect to inertial terms. As used in the example, three reference triads have been used in this thesis: Inertial Triad $(\hat{x}_N, \hat{y}_N, \hat{z}_N)$, Orbital Triad $(\hat{x}_O, \hat{y}_O, \hat{z}_O)$, and the Body Triad $(\hat{x}_B, \hat{y}_B, \hat{z}_B)$ (Figure 47).

The inertial triad is the non-accelerating triad in our model. It is needed to perform Newtonian mechanics. The equations of rotational motion, described later in this chapter, are based on the inertial triad. The First Point of Aries, which is the direction from Earth, through the sun, to the constellation of Aries at the vernal equinox when the sun crosses the ecliptic plane from south to north, determines the x-axis. The z-axis is along with the North Pole and y-axis is determined by the righthand rule.

The orbital triad is used for application-oriented purposes. The x-axis is tangential to the orbit in the direction of motion. The z-axis is pointing Earth in nadir direction and the y-axis is at the direction that comes from the righthand rule. The angles around these axes are roll, pitch and yaw angles, respectively. In addition, the axes can be named the same. The terms are analogous to the maneuvers of an aircraft. The orbital triad rotates as the spacecraft moves along the orbit and the axes always point to the directions defined earlier.

Finally, body triad is a fixed triad that is attached to the spacecraft and rotates with it. The direction of the axes are up to the designer; nonetheless, the principal axes of the spacecraft due to its inertial properties are selected as the alignment for the body triad to simplify the dynamics of the motion.

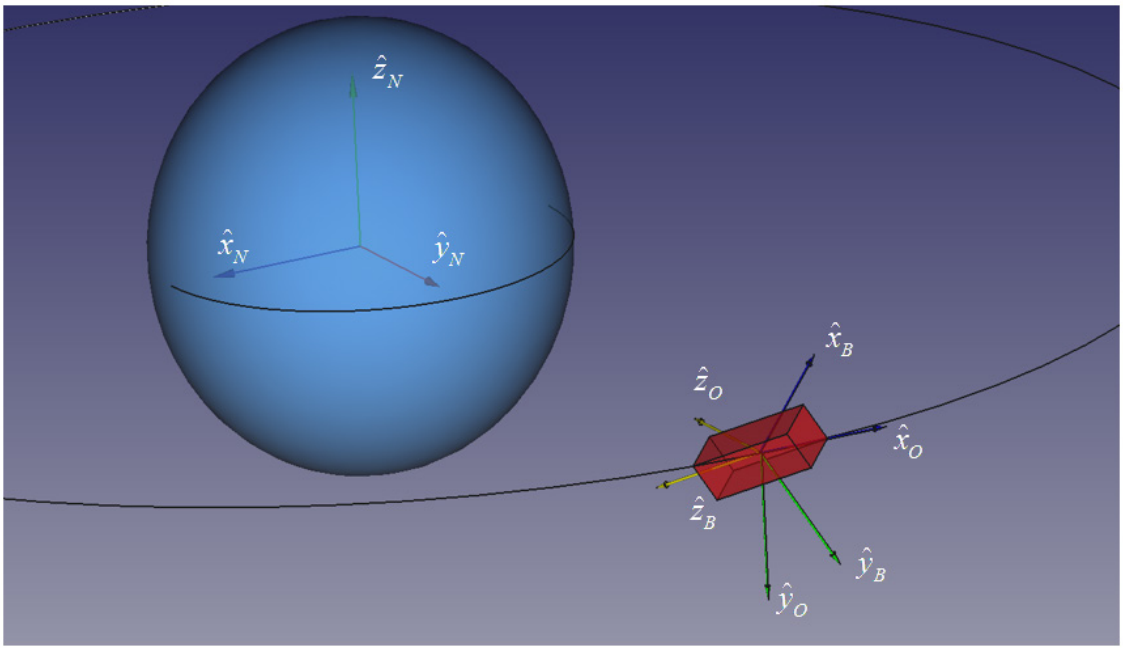

Figure 47. Inertial, Orbital and Body Triads

B. THE ATTITUDE CONTROL METHODOLOGY

The proposed attitude control methodology is to exploit the aerodynamic torque as a control torque by changing the location of the CoM with the shifting masses attached to the spacecraft. By shifting the masses, the position vector from CoP to CoM can be adjusted to change the magnitude and direction of the aerodynamic torque (Figure 48).

The use of shifting masses in attitude control has been previously studied by various researchers: dynamics of systems with moving internal parts [40], internal moving mass actuators for entry or reentry missions [32] and [36], trim control by internal moving masses for precision guidance systems [31], [33], [34], and [35], and attitude stabilization of satellites with shifting masses [41], [42], and [43]. This particular methodology exploiting the aerodynamic torque was only previously introduced by Chesi [3].

In regards to illustration of the methodology, an arbitrary example is presented (Figure 48). As the CoM is shifted from position in Figure 48(a) to a position in Figure 48(b), the distance between CoM and the CoP, which coincides with the geometric center

for a box-shaped body with no moving appendages, decreases. This results in a decrease in the magnitude of the aerodynamic torque. Moreover, if CoM is shifted to the position in Figure 48(c), the position vector from CoP to CoM changes direction. This results in a change of aerodynamic torque direction.

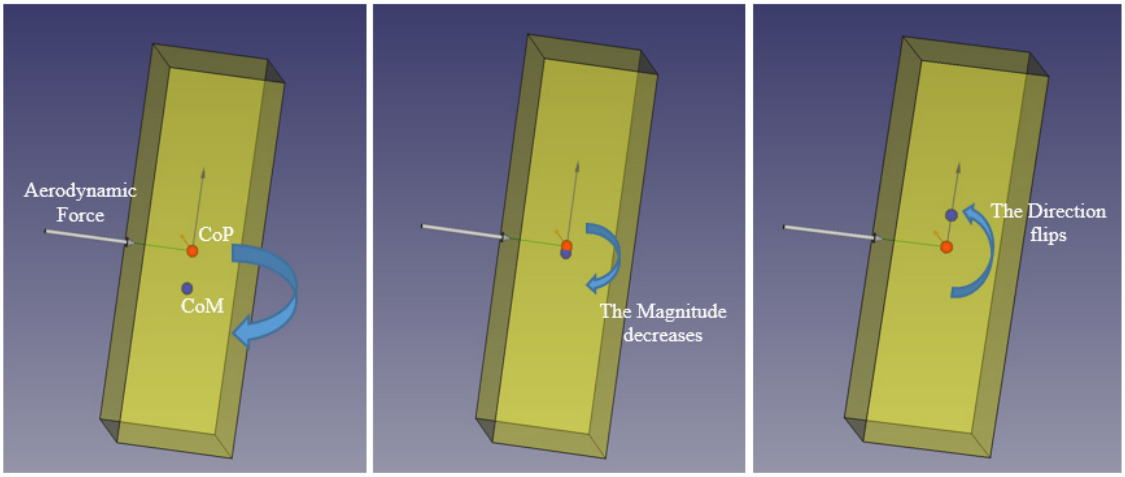

Figure 48. The Illustration of the Methodology

From left to right: Figure 48 (a), (b) and (c). The magnitude and direction of the aerodynamic torque changes as the CoM's position is changed with respect to the CoP.

This basic example uses only one axis shift, the yaw. Since aerodynamic force direction is approximately aligned with the orbital motion direction, the shift of the CoM along the yaw axis results in a change of the aerodynamic torque about the pitch axis. Similarly, the shift in pitch axis results in change of the aerodynamic torque about the yaw axis. Finally, the shift in roll axis creates no change in the aerodynamic torque. It means that the control torque will only be perpendicular to the relative motion's direction (i.e., $\hat{z}_O - \hat{y}_O$ plane) (Figure 49).

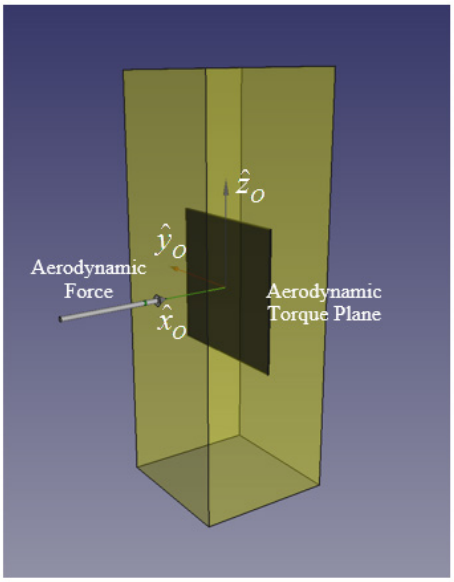

Figure 49. Aerodynamic Torque Plane

Aerodynamic torque is always perpendicular to the aerodynamic force's direction. In this illustration, aerodynamic torque can only be at the black plane, assuming that the CoP is at the geometric center and the aerodynamic force's direction is along the x-axis.

Because of the limitation in the aerodynamic torque direction, the control methodology of using only shifting masses to exploit aerodynamic torque becomes under-actuated [3]. The system can be fully actuated if another actuator that can generate torque about the roll axis is used. Chesi demonstrated the fully actuated control with two different alternatives: Magnetorquer or Reaction Wheel [3].

The approach in this thesis will be to use only the magnetorquer as a supplement. The justification is that a reaction wheel in one axis will still need momentum management, which cannot be generated by an under-actuated shifting masses system. To desaturate the reaction wheel in the roll axis, either another actuator must be added to the system, or two-layer control approaches will be followed such as rotating the spacecraft 90 degrees about the yaw or pitch axis to have authority in the roll axis, then desaturate the wheels. On the other hand, a magnetorquer in the roll axis will make the system fully actuated without any consideration for momentum management.

C. KINEMATICS AND DYNAMICS OF THE PLANT

Rotational kinematics block is responsible for calculating the attitude of the spacecraft by processing the angular velocity information, which is the output of the dynamics block. The dynamics block uses the equations of motion to propagate the angular velocity of the body triad relative to the inertial triad by using external torque and inertial parameters.

1. Rotational Kinematics

In this model, three different representation of attitude have been used: the Direction of Cosine Matrix (DCM), quaternions (q), and Euler Angles of pitch, roll and yaw (ϕ,θ,φ). The propagation of attitude in time is done by using Kinematic Differential Equations. Equation 4.1 shows the relationship between quaternion and angular velocity [20]:

$$\begin{bmatrix}\dot{q}_1\\ \dot{q}_2\\ \dot{q}_3\\ \dot{q}_4\end{bmatrix}_{BN} = \frac{1}{2}\begin{bmatrix} q_4 & -q_3 & q_2 & q_1\\ q_3 & q_4 & -q_1 & q_2\\ -q_2 & q_1 & q_4 & q_3\\ -q_1 & -q_2 & -q_3 & q_4\end{bmatrix}_{BN}\begin{bmatrix}\omega_1\\ \omega_2\\ \omega_3\\ 0\end{bmatrix}_{BN} \tag{4.1}$$

Quaternions are the most practical and fastest choice for the numerical propagation since they do not depend on trigonometric relations like Euler Angles or DCM [20]. With the numerically solved quaternions, we parameterize the DCM in Equation 4.2 [20]:

$$DCM_{BN} = \begin{bmatrix} 1-2(q_2^2+q_3^2) & 2(q_1q_2+q_3q_4) & 2(q_1q_3-q_2q_4)\\ 2(q_2q_1-q_3q_4) & 1-2(q_1^2+q_3^2) & 2(q_3q_2+q_1q_4)\\ 2(q_1q_3+q_2q_4) & 2(q_2q_3-q_1q_4) & 1-2(q_1^2+q_2^2)\end{bmatrix}_{BN} \tag{4.2}$$

Since the DCM can be represented as successive three principal axis rotations, the relationship between Euler angles and DCM can be represented as in Equation 4.3 [20].

$$DCM_{BN} = \begin{bmatrix} \cos\theta\cos\varphi & \cos\theta\sin\varphi & -\sin\theta \\ \sin\phi\sin\theta\cos\varphi - \cos\phi\sin\varphi & \sin\phi\sin\theta\sin\varphi + \cos\phi\cos\varphi & \sin\phi\cos\theta \\ \cos\phi\sin\theta\cos\varphi + \sin\phi\sin\varphi & \cos\phi\sin\theta\cos\varphi - \sin\phi\cos\varphi & \cos\phi\cos\theta \end{bmatrix}_{BN} \quad (4.3)$$

Roll, pitch and yaw angles of the body triad relative to the inertial triad can be calculated from Equation 4.3, which is for the rotational sequence 321. The same equations (4.1-4.3) can be used for the body triad relative to the orbital triad. For that case, the angular velocity of the body triad relative to the orbital triad should be calculated since the dynamics block is only generating the angular velocity of the body triad relative to the inertial triad. We assume that the orbit is circular. Then, the angular velocity of the orbital triad relative to the inertial triad becomes:

$$^{O}\vec{\omega}_{ON} = \begin{bmatrix} 0 \\ -\sqrt{\frac{\mu}{R^3}} \\ 0 \end{bmatrix}, \quad (4.4)$$

where μ is the gravitational constant of Earth and R is the radius of the orbit. Then, $^{O}\vec{\omega}_{ON}$ is transformed into the body triad with DCM_{BO}.

$$^{B}\vec{\omega}_{ON} = DCM_{BO}.{}^{O}\vec{\omega}_{ON} \quad (4.5)$$

After that, the angular velocity of the body triad relative to the orbital triad can be calculated (Equation 4.6). With the calculated angular velocity, the attitude information of the body triad relative to the orbital triad can be obtained from Equations 4.1-4.3.

$$^{B}\vec{\omega}_{BO} = {}^{B}\vec{\omega}_{BN} - {}^{B}\vec{\omega}_{ON} \quad (4.6)$$

2. Equations of Motion

Equations of rotational motion are derived by considering the shifting masses movements, which results in an inertial change. Therefore, we cannot simply use Euler's equations of motion. Instead, we derive the equations of motions by adopting the method presented by Grubin [40] that starts from generalized angular momentum equation, also introduced by Grubin [40]:

$$\underset{\rightarrow}{T} = \dot{\underset{\rightarrow}{H}} + \underset{\rightarrow}{S} \times \underset{\rightarrow}{a}\,, \tag{4.7}$$

where $\underset{\rightarrow}{S}$ is the first moment of mass of the system and $\underset{\rightarrow}{a}$ is the inertial acceleration of the reference point. In this study, the center of mass of the system without the shifting masses is considered as a reference point. The system without the shifting masses will be called the original system after this point. The illustration of the system geometry is shown in Figure 50.

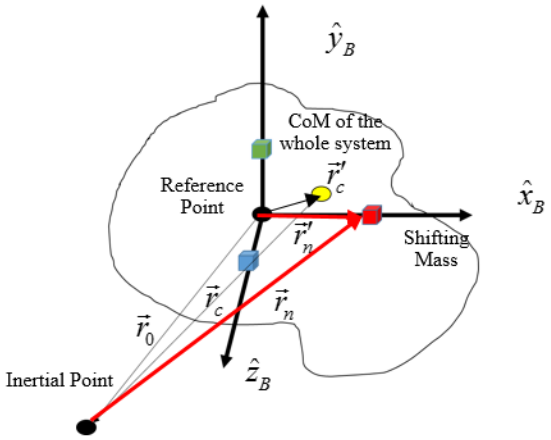

Figure 50. System Geometry

Equation 4.7 then is decomposed and each term is evaluated for both the shifting masses and original system.

$$\underset{\rightarrow}{H} = \underset{\rightarrow}{H}_0 + \sum \underset{\rightarrow}{H}_n\,, \tag{4.8}$$

where $\underrightarrow{H}_0$ is the angular momentum of the original system and $\sum \underrightarrow{H}_n$ is the sum of the angular momentum of each shifting mass. Time derivative of Equation 4.8 is

$$\dot{\underrightarrow{H}} = \dot{\underrightarrow{H}}_0 + \sum \dot{\underrightarrow{H}}_n \tag{4.9}$$

The angular momentum of the original system and the time derivative of it can be written as

$$\underrightarrow{H}_0 = I_0 \underrightarrow{\omega}_0 , \tag{4.10}$$

$$\dot{\underrightarrow{H}}_0 = I_0 \dot{\underrightarrow{\omega}}_0 + \underrightarrow{\omega}_0 \times \underrightarrow{H}_0 , \tag{4.11}$$

where I_0 and $\underrightarrow{\omega}_0$ are the inertia matrix and the angular velocity of the original system, respectively. The angular momentum of the individual shifting masses and the time derivative of it can be written as

$$\underrightarrow{H}_n = I_n \underrightarrow{\omega}_n + m_n \vec{r}_n \times \dot{\vec{r}}_n , \tag{4.12}$$

$$\dot{\underrightarrow{H}}_n = I_n \dot{\underrightarrow{\omega}}_n + \underrightarrow{\omega}_n \times \underrightarrow{H}_n + m_n \vec{r}_n \times \ddot{\vec{r}}_n , \tag{4.13}$$

where I_n, $\underrightarrow{\omega}_n$, m_n and $\vec{r}_n$ are the inertia matrix, inertial angular velocity, mass and the position of the particular shifting mass. Both linear and angular relative velocity and acceleration equations are used to derive inertial velocity and acceleration of shifting masses in Equations 4.14-4.17:

$$\dot{\vec{r}}_n = \dot{\vec{r}}_n' + \underrightarrow{\omega}_0 \times \vec{r}_n , \tag{4.14}$$

$$\ddot{\vec{r}}_n = \underrightarrow{\omega}_0 \times (\underrightarrow{\omega}_0 \times \vec{r}_n) + \dot{\underrightarrow{\omega}}_0 \times \vec{r}_n + 2\underrightarrow{\omega}_0 \times \dot{\vec{r}}_n' + \ddot{\vec{r}}_n' , \tag{4.15}$$

$$\underrightarrow{\omega}_n = \underrightarrow{\omega}_0 + \underrightarrow{\omega}_n' , \tag{4.16}$$

$$\dot{\underset{\rightarrow}{\omega}}_n = \dot{\underset{\rightarrow}{\omega}}_0 + \dot{\underset{\rightarrow}{\omega}}_n', \tag{4.17}$$

where $\dot{\vec{r}}_n'$, $\ddot{\vec{r}}_n'$ and $\underset{\rightarrow}{\omega}_n'$ are the relative linear velocity, acceleration and relative angular velocity of shifting masses with respect to the reference point. The second term of Equation 4.7 can be written as

$$\underset{\rightarrow}{S} = \sum m_n \vec{r}_n, \tag{4.18}$$

$$\vec{a} = \ddot{\vec{r}}_0 = \ddot{\vec{r}}_c - \ddot{\vec{r}}_c', \tag{4.19}$$

where $\ddot{\vec{r}}_0$ is the inertial linear acceleration of the original system, $\ddot{\vec{r}}_c$ is the inertial linear acceleration of the whole system's CoM and $\ddot{\vec{r}}_c'$ is the relative linear acceleration of the whole system's CoM. By definition, $\ddot{\vec{r}}_c$ and $\ddot{\vec{r}}_c'$ are written as

$$\begin{aligned} \ddot{\vec{r}}_c &= \frac{\vec{F}}{M + \sum m_n} \\ \ddot{\vec{r}}_c' &= \frac{\sum (m_n \ddot{\vec{r}}_n)}{M + \sum m_n} \end{aligned}, \tag{4.20}$$

where $\underset{\rightarrow}{F}$ and M are the external force acting on the system and the system's mass without the shifting masses, respectively. After merging Equations 4.8-4.20 into Equation 4.7, we have the general equation of motion:

$$\begin{aligned} I_0 \dot{\underset{\rightarrow}{\omega}}_0 + \underset{\rightarrow}{\omega}_0 \times I_0 \underset{\rightarrow}{\omega}_0 + \sum \left(I_n \dot{\underset{\rightarrow}{\omega}}_n \right) + \sum \left(\underset{\rightarrow}{\omega}_n \times \left(I_n \underset{\rightarrow}{\omega}_n + m_n \vec{r}_n \times \dot{\vec{r}}_n \right) \right) + \sum \left(m_n \vec{r}_n \times \ddot{\vec{r}}_n \right) + \ldots \\ \frac{1}{M + \sum m_n} \left(\sum m_n \ddot{\vec{r}}_n \right) \times \left(\sum m_n \vec{r}_n \right) = \underset{\rightarrow}{T} + \frac{\underset{\rightarrow}{F}}{M + \sum m_n} \times \left(\sum m_n \vec{r}_n \right) \end{aligned} \tag{4.21}$$

The assumption of non-rotational point masses for the shifting mass model simplifies Equation 4.21 to Equation 4.22 that is the equation of rotational motion for this model.

$$I_0\dot{\underrightarrow{\omega}}_0 + \underrightarrow{\omega}_0 \times I_0\underrightarrow{\omega}_0 + \sum\left(m_n\vec{r}_n \times \ddot{\vec{r}}_n\right) + \frac{1}{M+\sum m_n}\left(\sum m_n\ddot{\vec{r}}_n\right)\times\left(\sum m_n\vec{r}_n\right) = \ldots$$
$$\underrightarrow{T} + \frac{\underrightarrow{F}}{M+\sum m_n}\times\left(\sum m_n\vec{r}_n\right) \tag{4.22}$$

3. Rotational Dynamics

Edwards [41] linearizes Equation 4.22 for only single point mass by using the reduced mass parameters. However, the reduced mass parameters are not viable for linearizing Equation 4.22 when there are multiple masses, which is the case for our study.

The solution of Equation 4.22 for $\dot{\underrightarrow{\omega}}_0$ is not available analytically since $\ddot{\vec{r}}_n$ depends on $\dot{\underrightarrow{\omega}}_0$. Thus, an algebraic loop for Equation 4.22 is used to calculate angular velocity iteratively. The time-step of the iterations is adjusted to minimize the relative and absolute errors. The algebraic loop calculates the angular velocity of the body triad relative to inertial triad, which is the input of the kinematics block, as mentioned earlier.

The algebraic loop plant is validated by comparing the results with another dynamics plant that is formed based on the linearized equations of motion presented in Edwards [41]. To validate the algebraic loop, only one shifting mass is moved randomly for comparison of the effects on attitude of the spacecraft. The inertia and mass properties along with the external torque and force values are generated randomly for each validation effort. The results are compared for each axis after more than one hundred simulation runs and the difference between both plants stay under 10^{-6} rad/s, which is an acceptable error for rotational attitude studies (Figure 51).

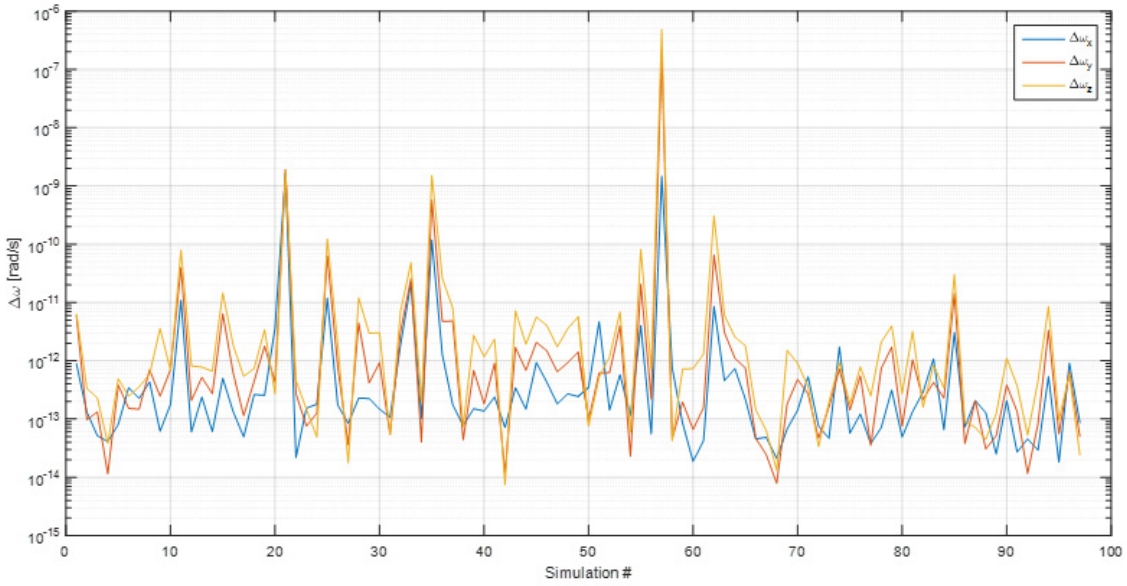

Figure 51. Difference in Angular Velocity

The difference in angular velocity is between the simulation model results based on Edwards's linearized equations of motion [41] and the proposed algebraic loop that solves the nonlinear equation of rotational motion (Equation 4.22).

D. MODELING OF THE DISTURBANCE TORQUES

1. Gravity Gradient Torque

The gravity gradient torque is calculated by using Equation 1.7. As shifting masses move in their assigned axis, the moments of inertia change along with the products of inertia. After each step, the inertia is updated by using the parallel axis theorem.

$$I_{Upd.} = I_0 + \sum \left(m_n \begin{bmatrix} 0 & -r_{n_z} & r_{n_y} \\ r_{n_z} & 0 & -r_{n_x} \\ -r_{n_y} & r_{n_x} & 0 \end{bmatrix}_B \begin{bmatrix} 0 & -r_{n_z} & r_{n_y} \\ r_{n_z} & 0 & -r_{n_x} \\ -r_{n_y} & r_{n_x} & 0 \end{bmatrix}_B \right) \tag{4.23}$$

The summation operator calculates the contribution of the shifting masses to the inertia. The updated inertia is then fed into the gravity gradient calculations to mimic the varying inertial responses of the spacecraft.

2. Aerodynamic Torque

The aerodynamic torque is the most dominant torque in our simulation environment. In addition, the attitude control methodology exploits the aerodynamic torque. Thus, modeling the aerodynamic torque is essential to this study. We start by using Equation 1.3 and integrate it over the CubeSat surface. We take benefit from the geometry of the CubeSat and write the result of the integral with summation operators [73].

$$\underline{\vec{T}}_{aero} = -\rho_a V_R^{\,2} \hat{\underline{\vec{V}}}_R \times \sum_{i=1}^{6} \left(\underline{\vec{c}}_{p_i} \left(\hat{\underline{\vec{V}}}_R \cdot \hat{\underline{\vec{n}}}_i \right) A_i H \left(\hat{\underline{\vec{V}}}_R \cdot \hat{\underline{\vec{n}}}_i \right) \right) \tag{4.24}$$

For every surface, the Heaviside function determines the shadowing status. The drag coefficient equals to 2 for this particular calculation. For the first order approach, atmospheric density is considered constant. Moreover, the orbital velocity is used for the relative velocity of the spacecraft with respect to the atmospheric particles since atmospheric particles are assumed stationary. This means that co-rotation of the atmosphere and high altitude winds are neglected. Equation 4.24 is used as the controller's aerodynamic torque estimator without the high fidelity information about the aerodynamic and atmospheric properties. This approach allowed us to simulate the real-world uncertainties and errors, and demonstrate the robustness of the closed-loop control algorithm.

3. Implementation of the Uncertainties in Atmospheric Attributes

The uncertainties in atmospheric attributes are added to the model in order to test the capability of the control block in terms of disturbance compensation. Since the proposed attitude control methodology seeks to exploit the aerodynamic torque, the aim is to augment a realistic representation of the varying attributes of the atmosphere. Mathematical representation of the 2001 U.S. Naval Research Laboratory Mass Spectrometer and Incoherent Scatter Radar Exosphere (NRLMSISE-00 Empirical Model of the atmosphere) [74], U.S. Naval Research Laboratory Horizontal Wind Model 2007

(HWM07) [75], and co-rotation of the atmosphere are used. The co-rotation of the atmosphere is calculated by using Equation 4.25:

$$\left[\underrightarrow{V}_{Co-Rot} = \underrightarrow{\Omega}_{Earth} \times \underrightarrow{x}_{S/C}\right]_{ECEF}, \tag{4.25}$$

where $\underrightarrow{V}_{Co-Rot}$ is the velocity of the atmospheric particles due to the co-rotation with respect to the orbital position of the spacecraft $\underrightarrow{x}_{S/C}$ and $\underrightarrow{\Omega}_{Earth}$ is the angular velocity of the Earth, which is 7.292×10^{-5} rad/s in magnitude. Every term in Equation 4.25 is in an Earth-Centered, Earth-Fixed (ECEF) coordinate system.

With the augmentations, relative velocity will no longer be the orbital velocity of the spacecraft. The co-rotation of the atmosphere and the horizontal winds change the direction of the relative velocity $\hat{\underrightarrow{V}}_R$ in Equation 4.24, which alters both the shadowing status of each surface and the projected surface area exposed to the flow. Besides, the magnitude of the relative velocity V_R is subjected to change because of the co-rotation and horizontal wind. The varying relative velocity along with non-constant atmospheric density affects the magnitude of the aerodynamic torque.

Solar and geomagnetic activity levels are included in NRLMSISE-00 and HWM07. However, different values for activity levels will not be investigated. Moderate level of solar index ($F_{10.7}$ = 140) and geomagnetic activity (daily planetary geomagnetic index, a_p = 15 nT) are used throughout the study.

Diurnal and seasonal variations are included in the models, so the initial date and hour, argument of latitude and longitude matter. However, these values will not be investigated and are started from 00:00 UTC January 1, 2015 at 0^0 of argument of latitude and longitude. On the contrary the altitude and inclination of the orbit that change the model outputs will be investigated in Chapter V.

E. THE ATTITUDE CONTROL DESIGN

In this section, the mathematical and physical explanation of the control method will be realized. Chesi [3] uses a non-linear adaptive feedback controller to achieve 3-

axis stabilization and analyzes the stability of the closed-loop system according to the Lyapunov Stability Theory. Instead of the nonlinear, a linear closed-loop control approach is adopted in this thesis; a Linear Quadratic Regulator (LQR) control law is used to achieve 3-axis stabilization. In the literature, Kumar [42] also uses LQR control method, but for one movable mass only, with no consideration of the environmental disturbance exploitation. The reason for choosing a linear control method is to demonstrate the capability of controlling non-linear system with a linear control design. With that demonstration, various sets of tools in the literature for linear control systems can be used which are not available for non-linear control methods.

1. Linearization of the Equations of Motion

Since the dynamics of the system is non-linear, the first step in designing the controller is to linearize the equations of motion. Linearized equations of motion then will be used in the control law. Equation 4.22 is an equation with nonlinearities. We started from the terms pertaining to shifting masses. Terms $\sum\left(m_n\vec{r}_n\times\ddot{\vec{r}}_n\right)$ and $\frac{1}{M+\sum m_n}\left(\sum m_n\ddot{\vec{r}}_n\right)\times\left(\sum m_n\vec{r}_n\right)$ are not zero since $\vec{r}_n$ and $\ddot{\vec{r}}_n$ are not aligned. The acceleration of the shifting masses experiences a Coriolis Effect due to the angular velocity of the spacecraft. However, the perpendicular component of the absolute acceleration with respect to the movement of shifting masses can be negligible if the masses' accelerations are very slow relative to the angular velocity. If we neglect the Coriolis Effect in absolute acceleration, both terms become zero. Then, Equation 4.22 becomes

$$I_0\dot{\underline{\vec{\omega}}}_0+\underline{\vec{\omega}}_0\times I_0\underline{\vec{\omega}}_0=\underline{\vec{T}}+\frac{\vec{F}}{M+\sum m_n}\times\left(\sum m_n\vec{r}_n\right) \tag{4.26}$$

If we combine all of the righthand terms and call it $\underline{\vec{T}}_D$ as disturbance torque, Equation 4.26 becomes simply

$$I_0\dot{\underrightarrow{\omega}}_0 + \underrightarrow{\omega}_0 \times I_0\underrightarrow{\omega}_0 = \underline{T}_D \tag{4.27}$$

Then, we extract the gravity gradient torque from $\underline{T}_D$ and write Equation 4.27 with respect to the principal axes of the original system:

$$\begin{aligned} J_x\dot{\omega}_x + (J_z - J_y)\omega_z\omega_y &= \frac{3\mu}{R^3}(J_z - J_y)c_2c_3 + T_x \\ J_y\dot{\omega}_y + (J_x - J_z)\omega_x\omega_z &= \frac{3\mu}{R^3}(J_x - J_z)c_1c_3 + T_y \\ J_z\dot{\omega}_z + (J_y - J_x)\omega_y\omega_x &= \frac{3\mu}{R^3}(J_y - J_x)c_1c_2 + T_z \end{aligned}, \tag{4.28}$$

where $I_0 = \begin{bmatrix} J_x & 0 & 0 \\ 0 & J_y & 0 \\ 0 & 0 & J_z \end{bmatrix}, \underrightarrow{\omega}_0 = \begin{bmatrix} \omega_x \\ \omega_y \\ \omega_z \end{bmatrix}_{BN}, \begin{bmatrix} c_1 \\ c_2 \\ c_3 \end{bmatrix} = DCM_{BO}\begin{bmatrix} 0 \\ 0 \\ 1 \end{bmatrix}, \underline{T}_{aero} = \begin{bmatrix} T_x \\ T_y \\ T_z \end{bmatrix}_B$.

After having Equation 4.28, Wie's method [20] to linearize the equations of motion with using small angles approach is adopted. When we assume that the angles in all axes are small enough to use small angle approach (α<5 degrees) to the system, DCM_{BO} and eventually direction of cosines of the local vertical relative to body triad becomes

$$DCM_{BO} = \begin{bmatrix} 1 & \alpha_z & -\alpha_y \\ -\alpha_z & 1 & \alpha_x \\ \alpha_y & -\alpha_x & 1 \end{bmatrix} \rightarrow \begin{bmatrix} c_1 \\ c_2 \\ c_3 \end{bmatrix} = \begin{bmatrix} -\alpha_y \\ \alpha_x \\ 1 \end{bmatrix}, \tag{4.29}$$

where α_x, α_y and α_z are roll, pitch and yaw angles of body triad relative to orbital triad. If the initial alignments of body and orbital triads are aligned ($\alpha_x = \alpha_y = \alpha_z = 0$ and $\underrightarrow{\omega}_0 = -\hat{j}\omega_{orb}$), after a small perturbation $\underrightarrow{\omega}_0$ becomes

$$\underline{\omega}_0 = \begin{bmatrix} \omega_x \\ \omega_y \\ \omega_z \end{bmatrix} = \begin{bmatrix} \dot{\alpha}_x - \omega_{orb}\alpha_z \\ \dot{\alpha}_y - \omega_{orb} \\ \dot{\alpha}_z + \omega_{orb}\alpha_x \end{bmatrix}, \tag{4.30}$$

where $\omega_x, \omega_y, \omega_z, \dot{\omega}_x, \dot{\omega}_y$ and $\dot{\omega}_z$ are very small with respect to ω_{orb}. When we insert Equations 4.29 and 4.30 into Equation 4.28 and neglect the products of small values, we produce the linearized equations of motion.

$$\begin{aligned} &J_x\ddot{\alpha}_x + \left(-J_x + J_y - J_z\right)\omega_0\dot{\alpha}_z + 4(J_y - J_z)\omega_0{}^2\alpha_x = T_x \\ &J_y\ddot{\alpha}_y + 3(J_x - J_z)\omega_0{}^2\alpha_y = T_y \\ &J_z\ddot{\alpha}_z + \left(-J_y + J_z + J_x\right)\omega_0\dot{\alpha}_x + (J_y - J_x)\omega_0{}^2\alpha_z = T_z \end{aligned} \tag{4.31}$$

In Equation 4.31, the shifting masses effects are embedded in the components of the aerodynamic torque. It will be discussed in the steering logic design. Before relating the control torque with shifting masses, an LQR control law will be designed. Since T_x, T_y and T_z are the aerodynamic torque components and the proposed attitude control methodology is to exploit them, $\underline{T}_{aero}$ can be called as the control torque $\underline{T}_C$.

2. LQR Control Law Design

Equation 4.31 represents a linear time-invariant dynamic system, so we can use a state-space control approach. The dynamics of the system then can be described as

$$\dot{x}(t) = Ax(t) + Bu(t), \tag{4.32}$$

where $x = \begin{bmatrix} \alpha_x \\ \alpha_y \\ \alpha_z \\ \dot{\alpha}_x \\ \dot{\alpha}_y \\ \dot{\alpha}_z \end{bmatrix} \cdots\cdots\rightarrow\cdots\cdots \dot{x} = \begin{bmatrix} \dot{\alpha}_x \\ \dot{\alpha}_y \\ \dot{\alpha}_z \\ \ddot{\alpha}_x \\ \ddot{\alpha}_y \\ \ddot{\alpha}_z \end{bmatrix} \cdots\cdots\& \cdots\cdots u = \begin{bmatrix} T_x \\ T_y \\ T_z \end{bmatrix}.$

State-space representation of angular angles and their rates can be used to generate a feedback to the system via the control input. This method is called a state feedback closed loop control [20]. A block diagram of the system is shown in Figure 52.

$$u(t) = -K \cdot x(t) \tag{4.33}$$

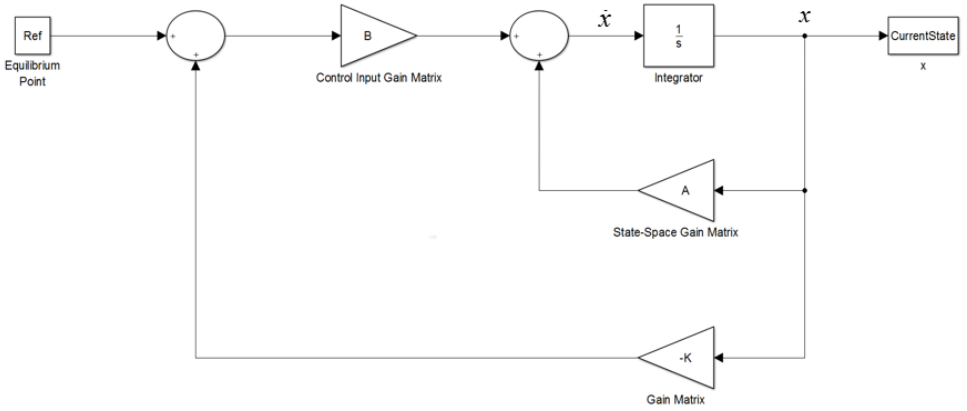

Figure 52. State Feedback Control Block Diagram

Then, Equations 4.31 and 4.32 are used to define matrices A and B.

$$A = \begin{bmatrix} 0 & 0 & 0 & 1 & 0 & 0 \\ 0 & 0 & 0 & 0 & 1 & 0 \\ 0 & 0 & 0 & 0 & 0 & 1 \\ \frac{4(J_z - J_y)\omega_{orb}^2}{J_x} & 0 & 0 & 0 & 0 & \frac{(J_x - J_y + J_z)\omega_{orb}}{J_x} \\ 0 & \frac{3(J_z - J_x)\omega_{orb}^2}{J_y} & 0 & 0 & 0 & 0 \\ 0 & 0 & \frac{(J_x - J_y)\omega_{orb}^2}{J_z} & \frac{(J_y - J_z - J_x)\omega_{orb}}{J_z} & 0 & 0 \end{bmatrix} \tag{4.34}$$

$$B = \begin{bmatrix} 0 & 0 & 0 \\ 0 & 0 & 0 \\ 0 & 0 & 0 \\ \dfrac{1}{J_x} & 0 & 0 \\ 0 & \dfrac{1}{J_y} & 0 \\ 0 & 0 & \dfrac{1}{J_z} \end{bmatrix} \tag{4.35}$$

Then, Equation 4.33 is inserted into Equation 4.32.

$$\dot{x}(t) = x(t)\left(A - BK\right) \tag{4.36}$$

After the Laplace transform, Equation 4.36 becomes the characteristic equation.

$$sI - A + BK = 0 \tag{4.37}$$

There is no unique solution for matrix K in Equation 4.37. Design of a state feedback control requires finding the gain matrix K to stabilize the system about the equilibrium point. In order to find the optimal gain matrix K, a Linear Quadratic Regulator approach will be implemented. The aim of the LQR method is to find a K that minimizes the performance index.

$$J = \int_0^\infty \left(x^T \cdot Q \cdot x + u^T \cdot R \cdot u\right) dt \tag{4.38}$$

where Q and R are positive-definite Hermitian or real symmetric matrices [76]. In Equation 4.38, Q and R matrices act as weight matrices. Q is responsible for weighing the cost of state error and R is responsible for weighing the cost of the control effort. A heuristic method is adopted in this thesis to choose the appropriate Q and R matrices.

$$Q = diag\left[\cdots \quad \left(\frac{\alpha_i^{\,2}}{x_{i\max}^{\,2}}\right) \quad \cdots\right]$$
$$R = diag\left[\cdots \quad \left(\frac{\beta_i^{\,2}}{u_{i\max}^{\,2}}\right) \quad \cdots\right], \tag{4.39}$$

where $x_{i\max}$ is the maximum allowable state and $u_{i\max}$ is the maximum achievable torque (saturation limit). α_i and β_i will be chosen to determine the weight matrices. Let us insert Equation 4.33 into Equation 4.38.

$$J = \int_0^\infty x^T \left(Q + K^T \cdot R \cdot K\right) x dt \tag{4.40}$$

Then, we introduce a new positive-definite matrix P as in Ogata [76].

$$x^T \left(Q + K^T \cdot R \cdot K\right) x = -\frac{d}{dx}\left(x^T \cdot P \cdot x\right) \tag{4.41}$$

By solving P in the reduced-matrix Riccati equation (Equation 4.42) and by using the quadratic optimal equation for K (Equation 4.43), the gain matrix for calculating the optimal control input is acquired [76].

$$A^T \cdot P + P \cdot A - P \cdot B \cdot R^{-1} \cdot B^T \cdot P + Q = 0 \tag{4.42}$$

$$K = R^{-1} \cdot B^T \cdot P \tag{4.43}$$

MatLab Control Toolbox is used to calculate the gain matrix K by using the command line "*K=lqr(A,B,Q,R).*" If eigenvalues of the (A-BK) have negative real parts, which means that the system is stable, an optimal feedback control gain matrix K can be found [76].

As stated in the linearization process, the dynamics of the shifting masses in terms of acceleration and velocity are neglected in the control block. This is true when we assume that the motion of the shifting masses is slow. However, the motion of the shifting masses is highly related to the gain parameter. If the designer chooses an aggressive set of weight matrices (Q>>R), the control effort increases, meaning that shifting masses move with high velocity and acceleration. This particular setting makes the assumption in the linearization invalid and the shifting masses will induce a torque on the CubeSat that is not intended in the control block. Eventually, the stabilization process will be degraded.

To avoid high velocity and acceleration effects of the shifting masses, the control effort is minimized within the state error limitations (Q<<R). With these settings, masses will move slowly and the dynamics effects will be negligible. The downside of this setting is the slow stabilization times and relaxed steady-state error after stabilization. To eliminate the relaxed steady-state error, a gain-scheduling concept is adopted. Two different gain values are used, aggressive and less aggressive. To choose which value is operative at the current state, a decision circle in the phase plane is used (Figure 53). The aggressive gain is used inside the circle and less aggressive gain is used outside the circle. This two-level gain scheduling concept limits the shifting masses in slow motion while meeting the pointing accuracy goal of the system (< 1^{o}). More levels could be designed but in the scope of this study only the two-level gain scheduling concept is used.

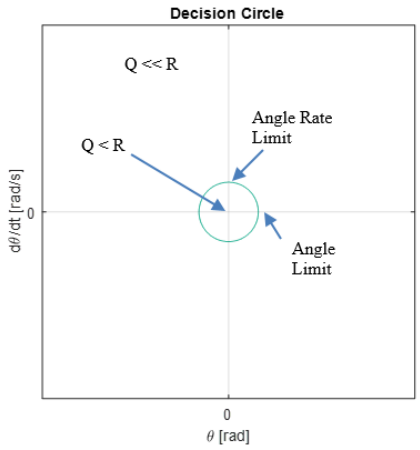

Figure 53. Decision Circle for Gain Scheduling in Phase Plane

3. Steering Logic Design

The LQR Control design provides a control input, which is the righthand side of Equation 4.31. As mentioned earlier, the torque components in Equation 4.31 are aerodynamic torque's components. However, we need a steering logic that gives desired positions of the shifting masses that will cause the requested torque. Therefore, by feeding the non-linear dynamics plant with positions of the shifting masses, the system will experience an aerodynamic torque that stabilizes the spacecraft. Let us examine the aerodynamic torque components closely.

$$\underline{T}_{aero} = \underline{T}_{aero_0} + \underline{T}_{aero_{SM}}, \tag{4.44}$$

where $\underline{T}_{aero_0}$ is the aerodynamic torque acts on the original system and $\underline{T}_{aero_{SM}}$ is the aerodynamic torque change due to the shifting masses effect. $\underline{T}_{aero_0}$ is due to the difference between the CoP and the CoM of the original system which both are assumed constant. Hence, $\underline{T}_{aero_0}$ does not change with varying positions of shifting masses. The effects of the shifting masses on aerodynamic torque can be seen in Equation 4.26 such that:

$$\underline{T}_{aero} - \underline{T}_{aero_0} = \underline{T}_{aero_{SM}} = \frac{\underline{F}_{ext}}{M + \sum m_n} \times \left(\sum m_n \vec{r}_n \right) \tag{4.45}$$

By definition, $\underline{T}_{aero_{SM}}$ can only be in a plane perpendicular to the aerodynamic force, which is $\underline{F}_{ext}$ in this model. However, control torque $\underline{T}_C$ that is requested by the system can be in any direction. This is the reason why the proposed methodology with the shifting masses is under-actuated. Thus, $\underline{T}_C$ should be decomposed into two components. $\vec{T}_{\perp}$, which is perpendicular to the $\underline{F}_{ext}$, will be allocated to the shifting masses control share and $T_{\parallel}$, which is parallel to the $\underline{F}_{ext}$, will be allocated to the other control actuator, which is magnetorquer (Figure 54).

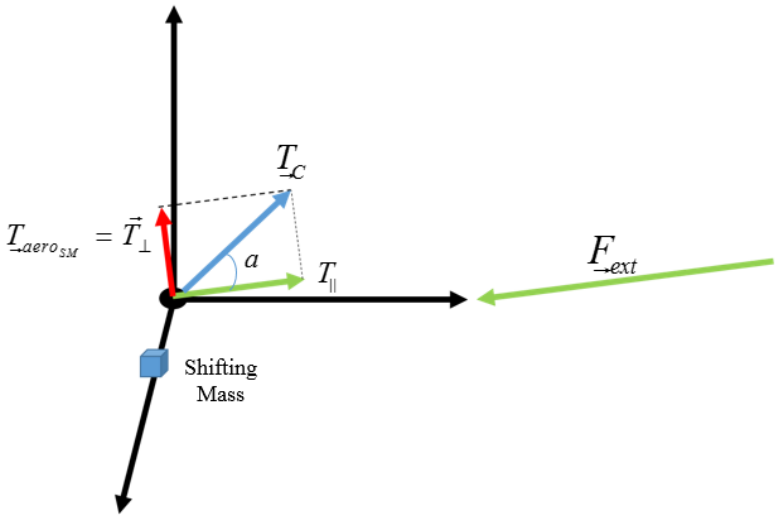

Figure 54. Decomposition of the Control Torque with respect to the External Force

The mathematical representations of both components are:

$$\begin{aligned}
\vec{T}_\perp &= \vec{T}_C - T_\parallel \\
T_\parallel &= \left|\vec{T}_C\right| \cos a \hat{F}_{ext} \\
T_\parallel &= \left|\vec{T}_C\right| \left(\frac{\vec{T}_C \bullet \vec{F}_{ext}}{\left|\vec{T}_C\right|\left|\vec{F}_{ext}\right|} \right) \left(\frac{\vec{F}_{ext}}{\left|\vec{F}_{ext}\right|} \right) \\
\vec{T}_\perp &= \vec{T}_C - \left(\frac{\left(\vec{T}_C \bullet \vec{F}_{ext}\right)\vec{F}_{ext}}{\left|\vec{F}_{ext}\right|^2} \right) = \underset{\rightarrow}{T}_{aero_{SM}}
\end{aligned} \tag{4.46}$$

By design, shifting masses move only in one axis, so Equation 4.45 becomes

$$\frac{M + \sum m_n}{\sum m_n} \begin{bmatrix} T_{aero_{SM_x}} \\ T_{aero_{SM_y}} \\ T_{aero_{SM_z}} \end{bmatrix} = \underset{\rightarrow}{F} \times \begin{bmatrix} r_x \\ r_y \\ r_z \end{bmatrix} \tag{4.47}$$

In Equation 4.47, to solve for position components of each shifting masses, inverse cross product operation must be done, which does not exist unless $\vec{r}$ and $\vec{F}$ are perpendicular. Let us assume that $\vec{r}$ and $\vec{F}$ are perpendicular which is true if body and orbital triads are aligned. Since the equilibrium point of the system is the aligned attitude, the assumption is justifiable. With the assumption, the cross product can be manipulated in such a way that:

$$\begin{aligned} \vec{T} &= \vec{F} \times \vec{r} = -\vec{r} \times \vec{F} \\ \vec{F} \times \vec{T} &= \vec{F} \times \left(-\vec{r} \times \vec{F} \right) \\ \vec{F} \times \vec{T} &= -\left(\left(\vec{F} \bullet \vec{F} \right) \vec{r} - \left(\vec{r} \bullet \vec{F} \right) \vec{F} \right) \end{aligned} \quad , \tag{4.48}$$

where $\left(\vec{r} \bullet \vec{F} \right)$ goes to zero. Hence, Equation 4.49 becomes the particular solution of Equation 4.47 for positions of shifting masses.

$$\vec{r} = \frac{\vec{T}_{aero_{SM}} \times \vec{F}_{ext}}{\vec{F}_{ext} \bullet \vec{F}_{ext}} \left(\frac{M + \sum m_n}{\sum m_n} \right) \tag{4.49}$$

The control block does not have the high fidelity aerodynamic model output information. This means that the aerodynamic torque and force acting on the CubeSat is estimated in the control block. This estimation does not take the horizontal wind model and the co-rotation of the atmosphere into account. In addition, an approximate air density value for the particular altitude is used as a constant unlike the atmosphere model process in the dynamics plant. This difference between the control and the dynamics plant is for testing the control method's capability to handle the disturbances, which is the case in real world applications.

4. Position Tracker Design

The shifting masses have limited travel distances within the CubeSat dimensions. However, the control design calculates the ideal position of the shifting mass, which may

be out of the CubeSat boundaries. To avoid that, the requested position is saturated before the position tracker block at the maximum travel limit of the actual system (Figure 54), which is ± 3.5 cm in Shift-Mass Sat design.

Another constraint of the shifting masses is the velocity and acceleration of shifting mass actuators. The requested position from the control and steering law is fed into a position tracker block. A PD position tracker is used in this study to move the shifting masses (Figure 54). Kp and Kd are selected such that the velocity of the shifting masses is never larger than its maximum value. The limitation of the actuator is given by the specifications of the component [69].

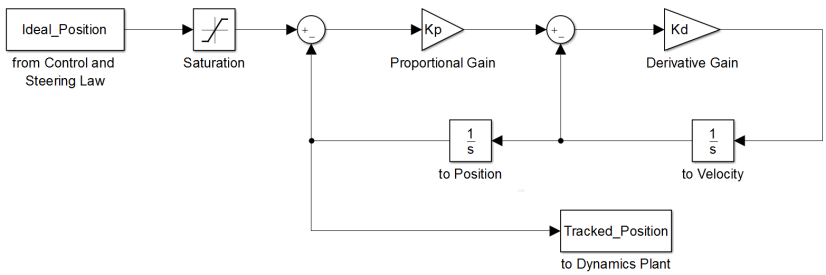

Figure 55. PD Position Tracker

5. Roll Actuator Supplementation

The inherent under-actuated feature of the shifting masses attitude control system exploiting the aerodynamic torque is fully-actuated when a roll actuator is added to the system. As mentioned regarding the Shift-Mass Sat design, a magnetorquer supplements the attitude control system. In order to calculate the necessary magnetic dipole moment of the magnetorquer we revisit Equation 1.9.

$$\vec{T}_{mag} = \vec{m}_m \times \vec{B} \tag{1.9}$$

To solve for the necessary magnetic dipole moment with torque given by the control logic and the magnetic field of the Earth given by the World Magnetic Model

2015 [77], we manipulate the equation with the same operations that we did in Equations 4.47-4.49, assuming that magnetic dipole moment and the magnetic field of the Earth is perpendicular to each other. After that the magnetic dipole moment becomes

$$\underset{\rightarrow}{m}_m = \frac{\underset{\rightarrow}{B} \times \vec{T}_{mag}}{\underset{\rightarrow}{B} \bullet \underset{\rightarrow}{B}}, \tag{4.50}$$

where $\underset{\rightarrow}{m}_m$ is limited to ±0.258 A-m^2 according to Shift-Mass Sat design component selections.

For comparison reasons, a reaction wheel is also added. The reaction wheel in the simulation has the initial wheel speed as 100 rpm to avoid zero-crossing issues. In addition, the angular momentum accumulation is monitored to check the saturation of the wheel even though the accumulation is very slow.

V. NUMERICAL TESTS AND EVALUATIONS

The simulation model has been tested with different configurations to see the behavior of Shift-Mass Sat in the orbital environments that most CubeSats are exposed to. As mentioned earlier, to accomplish a realistic simulation, Shift-Mass Sat design and CubeSat mission data analysis have been integrated into the simulation.

The ultimate goal of the simulation tests is to acquire realistic system behavior with shifting masses system as the attitude control actuator.

A. MEASURE OF EVALUATIONS

During the simulation runs for different configurations, metrics, which reflect the performance of the control methodology, have been used as measures of evaluations (MoE). The MoEs are used to see the effects of different configuration and compare them.

1. The first MoE is the settling time for the stabilization of the CubeSat's angular velocity. Settling time is compared in order to see the response of the system with the tested environment or actuator configuration. The unit of the settling time in this study is the fraction of an orbit.

2. The second MoE is the steady-state error or the pointing accuracy in degrees. Euler angles in orbital triad are used for the computation of the pointing accuracy since the mission of Shift-Mass Sat is an Earth-imaging mission with fixed-nadir pointing. Pointing accuracy is used to see how well the shifting masses actuator system copes with the disturbances and uncertainties after the stabilization.

3. The third MoE is the travel distance of the shifting masses in meters. This MoE is computed to compare the usage of the shifting masses by calculating the total distance that a shifting mass travels throughout the simulation time. Total distance is the summation of the absolute displacements in each time-step.

B. DETERMINATION OF THE BASELINE CONFIGURATION AND THE DEMONSTRATION OF THE PROPOSED ATTITUDE CONTROL METHOD

Before comparing different configurations and their MoE values, demonstration of the proposed attitude control methodology is presented with three baseline

configuration candidates. The difference between baseline candidates is the number of shifting masses and the supplementing roll actuator type.

For the simulations, initial angular velocity of the body triad relative to the inertial triad is 0.01 rad/s (0.57 deg/s) in every axis while the orbital and body triads are aligned. The mass of the shifting masses are 150 grams and maximum travel distance and velocity values are ± 35 mm and 5 cm/s, respectively. The altitude and inclination of the orbit are 300 km and 0 degree, respectively. The CubeSat is at the 0-degree longitude at the ascending node. The starting time is January 1, 2015 00:00 UTC. Inertial parameters and CoM position are [0.00598; 0.00089; 0.01679] kg-m^2 and [0.0184; -0.0004; 0.0007] m, respectively. Simulation time is 10 orbits.

First, three shifting masses and magnetorquer are used (Figures 56–59). Then, two shifting masses with magnetorquer are used (Figures 60–63). Finally, two shifting masses with a reaction wheel at roll axis are used (Figures 64–67). For all three, the detumbling of the spacecraft is achieved within one orbit and stable pointing (under 0.4 degrees) is maintained throughout the simulation.

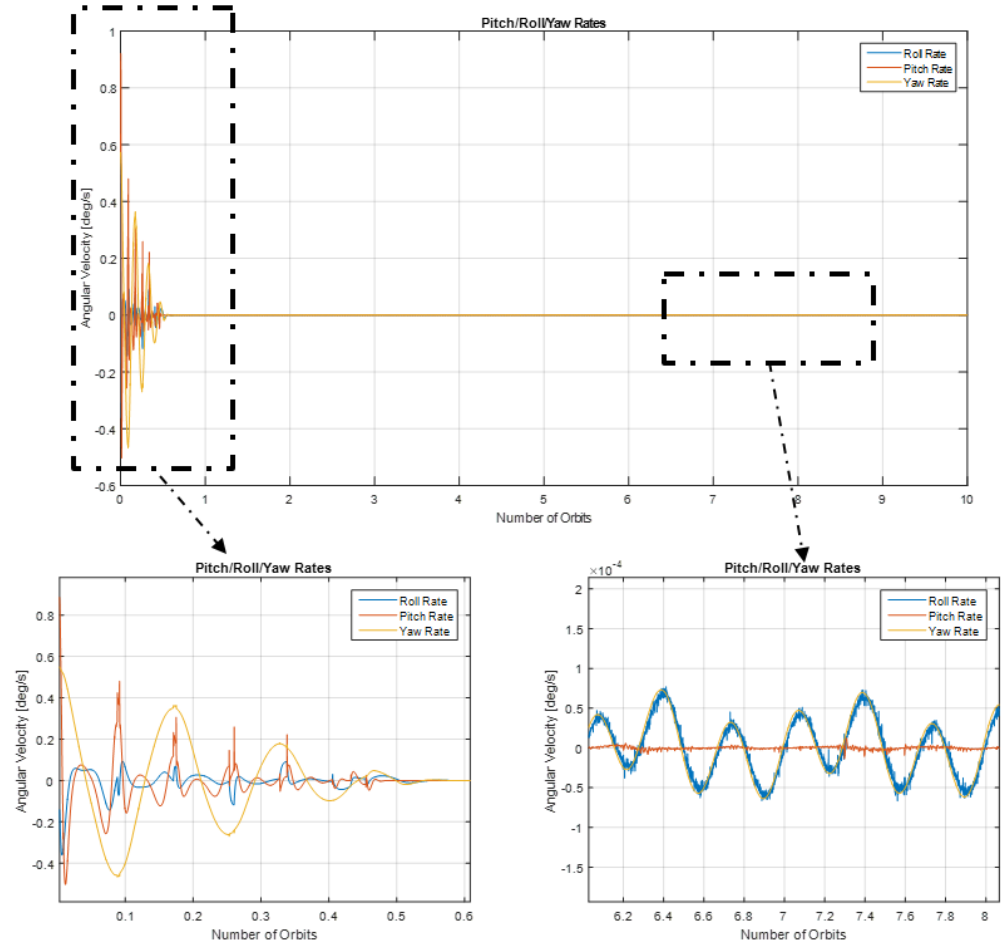

Figure 56. Angular Rate of the Body Triad Relative to Orbital Triad (Three Shifting Masses with Magnetorquer)

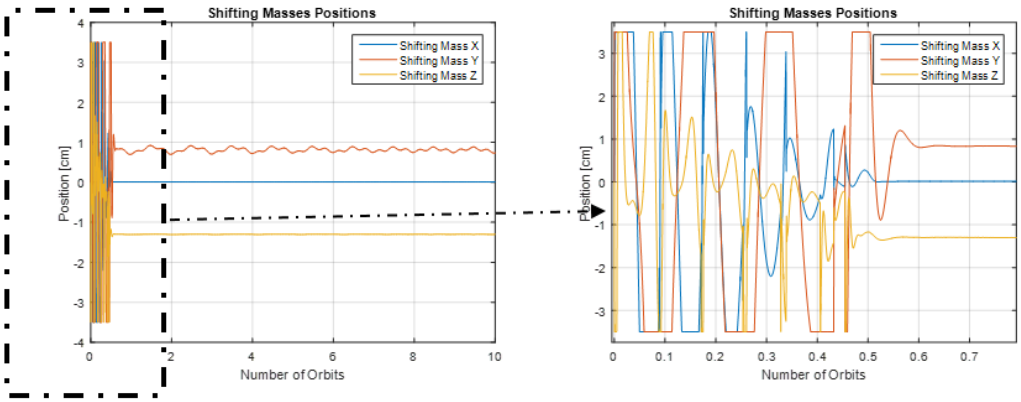

Figure 57. Shifting Masses Positions (Three Shifting Masses with Magnetorquer)

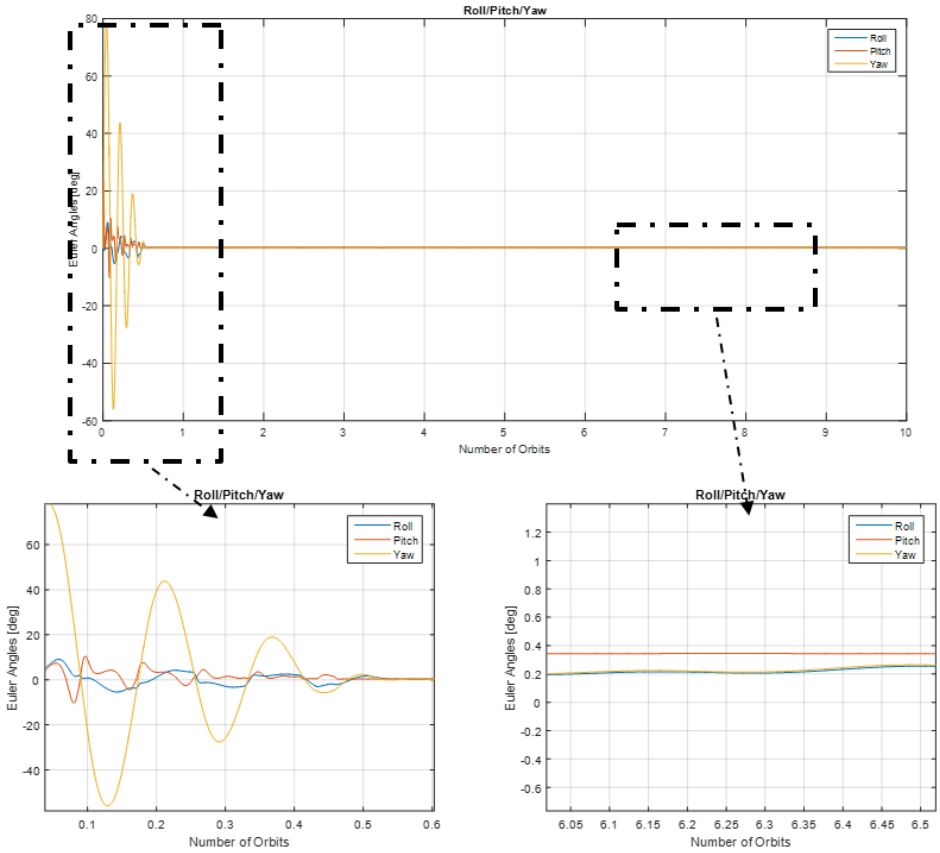

Figure 58. Euler Angles of the Body Triad Relative to Orbital Triad (Three Shifting Masses with Magnetorquer)

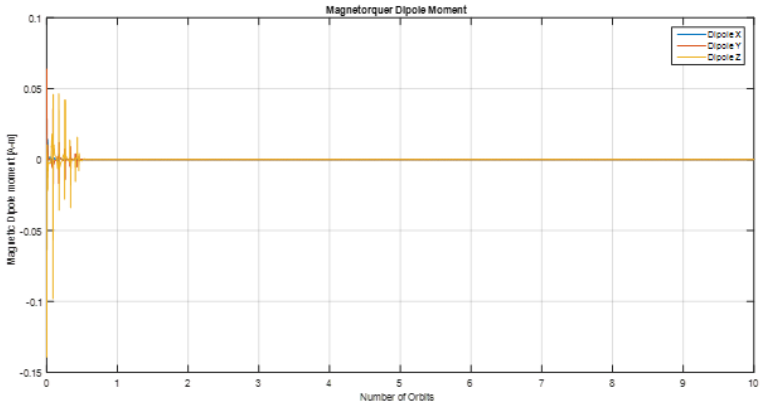

Figure 59. Dipole Moment of the Magnetorquer (Three Shifting Masses with Magnetorquer)

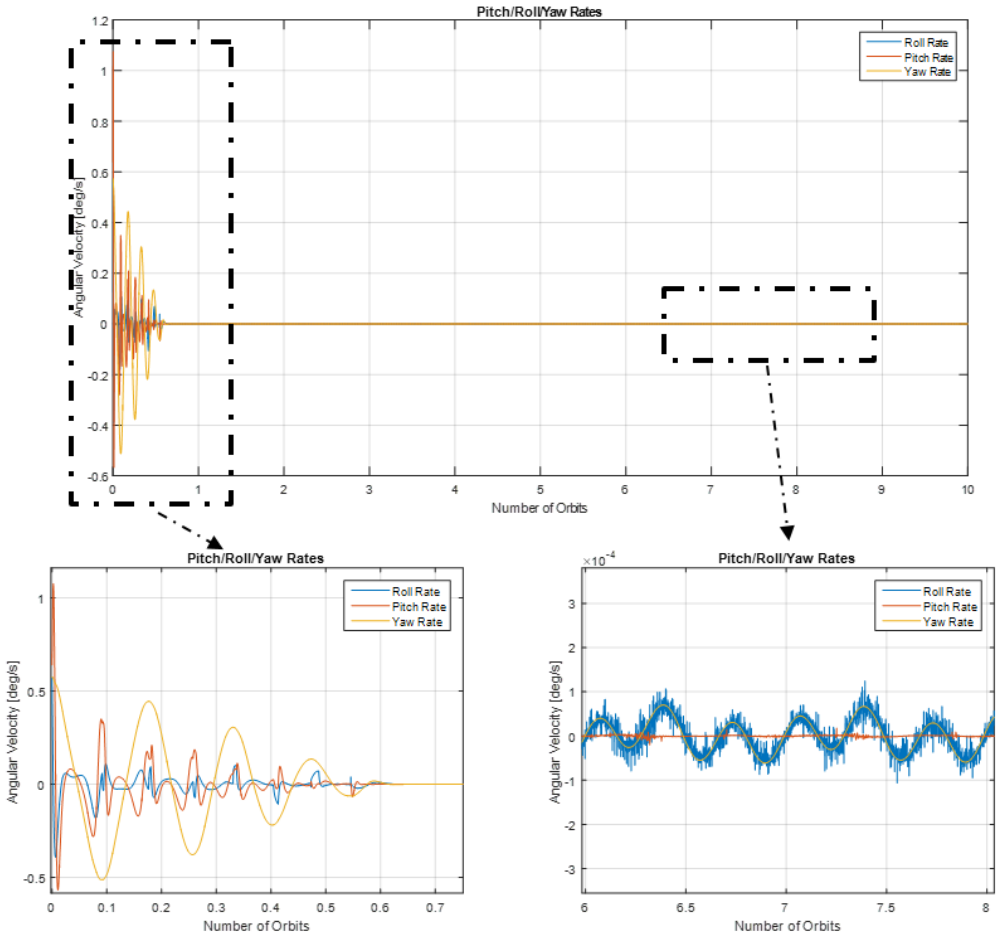

Figure 60. Angular Rate of the Body Triad Relative to Orbital Triad (Two Shifting Masses with Magnetorquer)

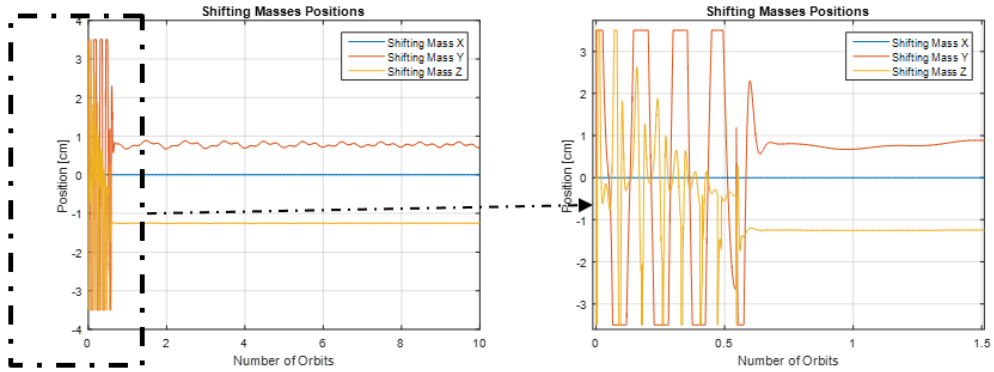

Figure 61. Shifting Masses Positions (Two Shifting Masses with Magnetorquer)

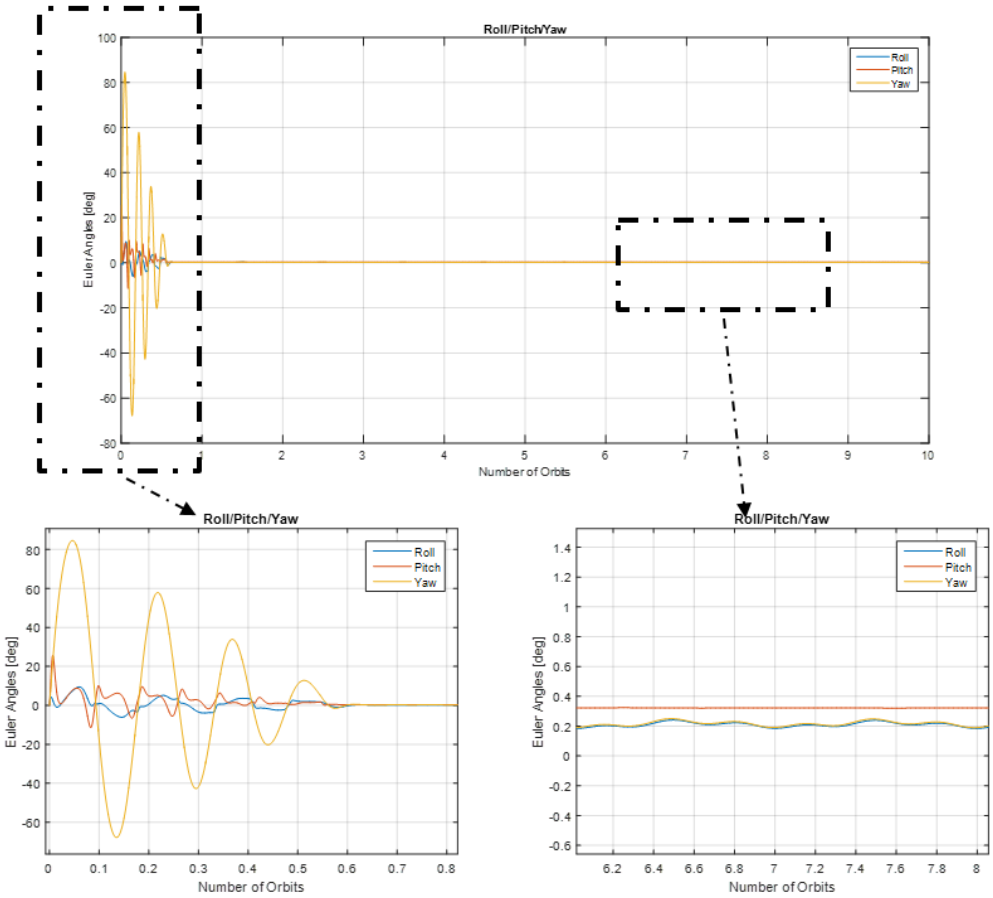

Figure 62. Euler Angles of the Body Triad Relative to Orbital Triad (Two Shifting Masses with Magnetorquer)

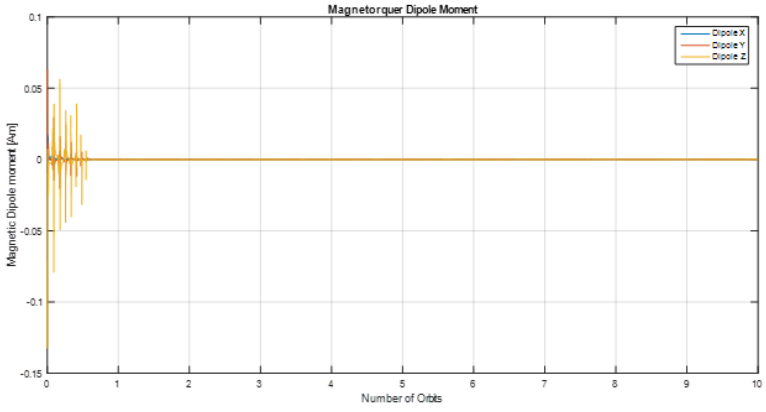

Figure 63. Dipole Moment of the Magnetorquer (Two Shifting Masses with Magnetorquer)

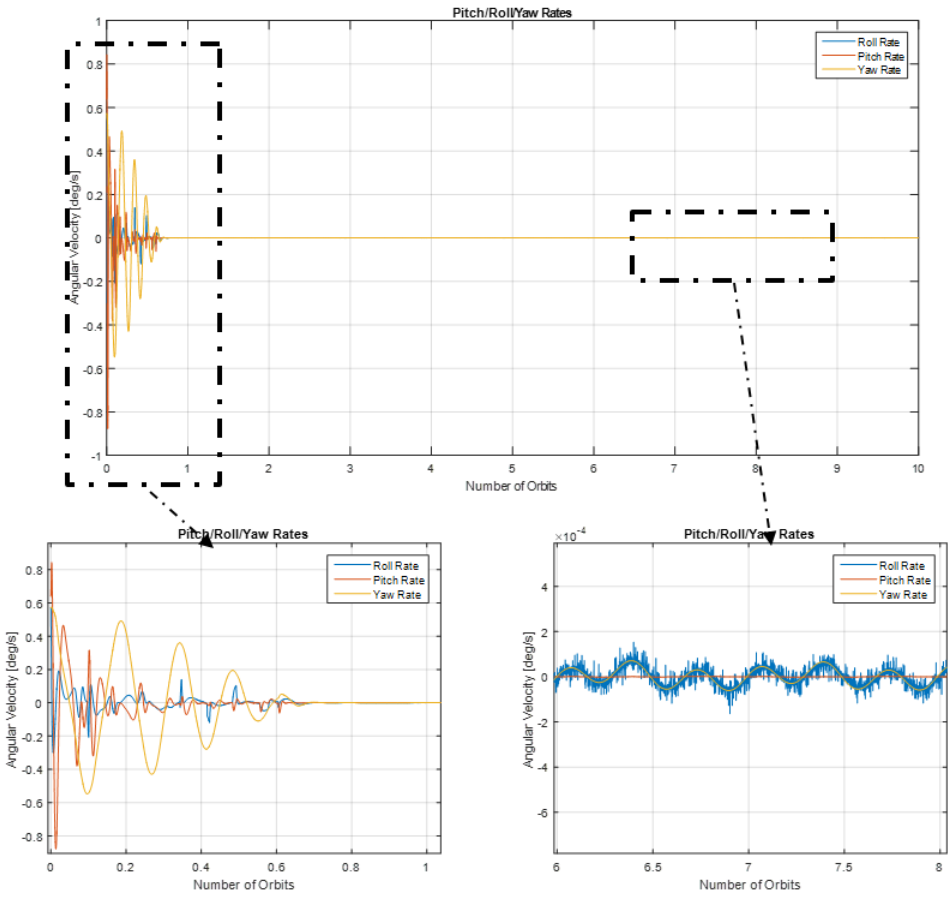

Figure 64. Angular Rate of the Body Triad Relative to Orbital Triad (Two Shifting Masses with a Reaction Wheel)

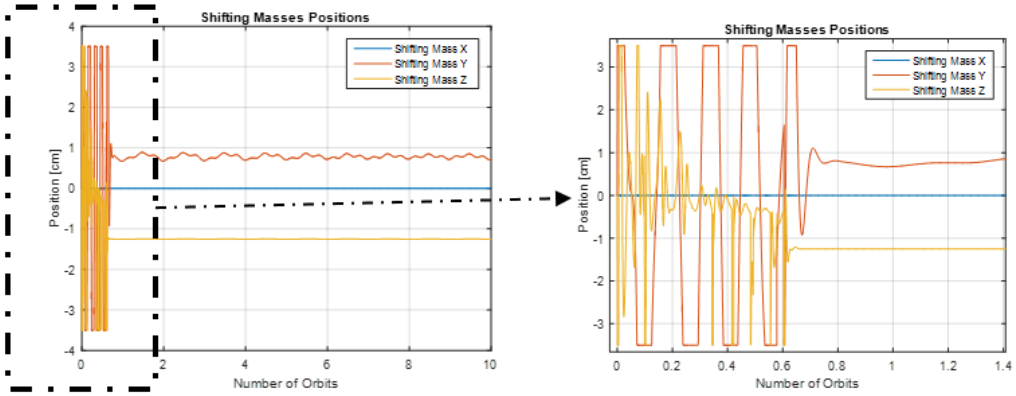

Figure 65. Shifting Masses Positions (Two Shifting Masses with a Reaction Wheel)

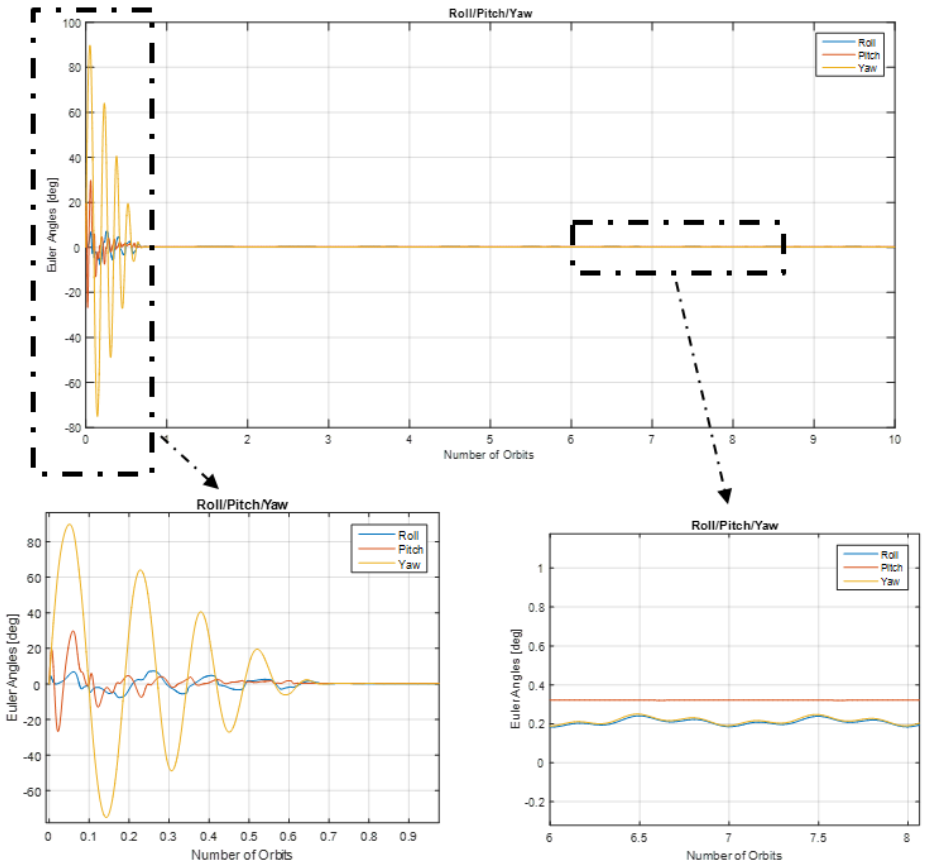

Figure 66. Euler Angles of the Body Triad Relative to Orbital Triad (Two Shifting Masses with a Reaction Wheel)

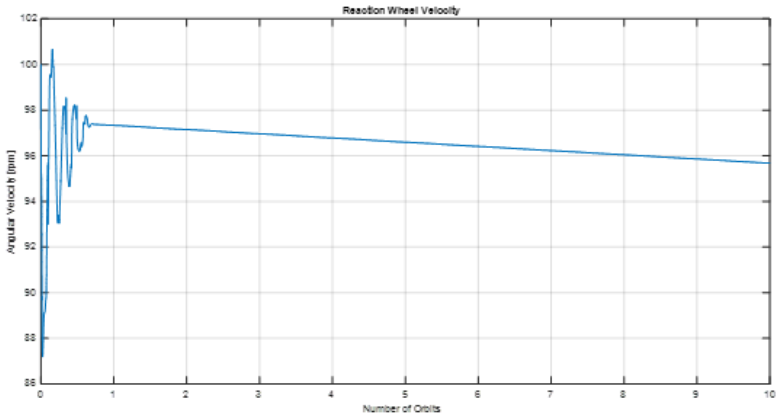

Figure 67. Angular Velocity of the Reaction Wheel (Two Shifting Masses with a Reaction Wheel)

In Table 9, comparison between baseline candidates is shown with respect to different MoEs. In regard to settling time, the three shifting masses configuration is better than the others. However, the shifting mass at x axis is merely active after stabilization as the x-axis is aligned with the orbital motion direction (Figure 56). The maintained pointing accuracy difference is less than 0.07 degrees among all three.

Table 9. Comparison Between Baseline Candidates

	Angular Rate Settling Time [Orbits]			Steady State Error [deg]			Shifting Masses Travel Distance [m]		
	Roll	Pitch	Yaw	Roll	Pitch	Yaw	X-axis	Y-axis	Z-axis
3 Shifting Masses with Magnetorquer	0.50	0.46	0.53	0.26	0.35	0.27	0.97	0.98	0.67
2 Shifting Masses with Magnetorquer	0.57	0.55	0.59	0.25	0.33	0.26	0	1.07	0.44
2 Shifting Masses with a Reaction Wh.	0.64	0.61	0.67	0.19	0.32	0.21	0	1.36	0.48

It is worth elaborating on the steady-state error results. As explained earlier, roll axis is stabilized by a complementary traditional attitude control actuator. However, there is still an attitude error due to the gain parameter selections in the LQR control law. As stated in Chapter IV, the dynamics of the shifting masses are neglected in the control assuming that they are relatively slow. Therefore, if we increase the gain and request a faster shifting mass movement, the shifting mass dynamics that we neglected induce a disturbing torque on the spacecraft. Thus, the stabilization will not be achieved. This is the reason of the gain scheduling implementation in Chapter IV. The limitation over the gain parameters results in a steady-state error.

The extra factor of the steady-state error in pitch and yaw angles is the aerodynamic equilibrium attitude. In aerodynamic equilibrium, there is no aerodynamic torque on the spacecraft meaning that CoM and CoP are aligned with relative wind direction. Since LQR law is based on achieving equilibrium point where there is no disturbances, shifting masses try to hold the attitude in aerodynamic equilibrium resulting in a residual state error. This concept is explained in detail later.

After the demonstration of the success of the proposed attitude control methodology with three fundamental configurations, three shifting masses with magnetorquer is chosen as the baseline configuration. The following explorations of design space will be based on this configuration.

C. EXPLORATION OF THE ALTITUDE AND INCLINATION EFFECTS ON THE CONTROL

Since the proposed attitude control methodology exploits the aerodynamic torque, the altitude is crucial to the performance of the attitude control. In addition, the inclination of the orbit affects the performance as the relative wind direction changes due to the co-rotation of the atmosphere and horizontal winds. In order to compare different altitude and inclination values effectively, the control gain parameters are kept the same for all. The altitude and inclination values are derived from the mission and orbit design section in Chapter III (Table 1). However, the control system is not successful for altitudes of 450 and 600 km due to the dramatic decrease in aerodynamic force, so they are left out of the comparisons.

Settling time increases almost linearly with the altitude in all axes (Figure 68) as the aerodynamic torque decreases with the atmospheric density. According to the results, the steady-state error decreases with the increasing altitude (Figure 68), which at first looks odd. However, the control gain parameters are kept constant for all configurations. At 200 km altitude, the control system could achieve better than 1.5 degrees of pointing accuracy with different control gains, but that would make the comparison ineffective. The reason for the decrease in steady-state error with altitude, even though the control system becomes weaker, is the environmental disturbances. Environmental disturbances weaken as the altitude increases. Thus, it is easier to maintain narrower pointing.

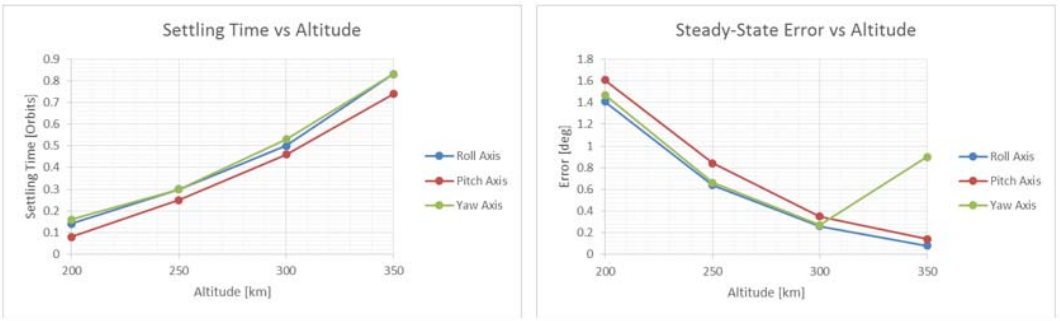

Figure 68. Settling Time and Steady-State Error versus Altitude

Regarding inclination, settling time is not affected much (Figure 69). However, the pointing error after stabilization increases as inclination goes to 90 degrees, especially in roll and yaw axes due to the co-rotation of the atmosphere and the horizontal winds. The dramatic increase in the travel distance of the shifting mass in Y-axis is another implication of the inclination effect on the CubeSat (Figure 70).

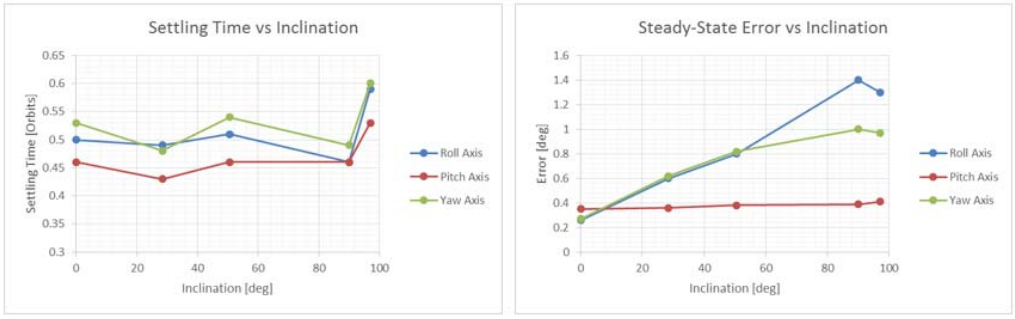

Figure 69. Settling Time and Steady-State Error versus Inclination

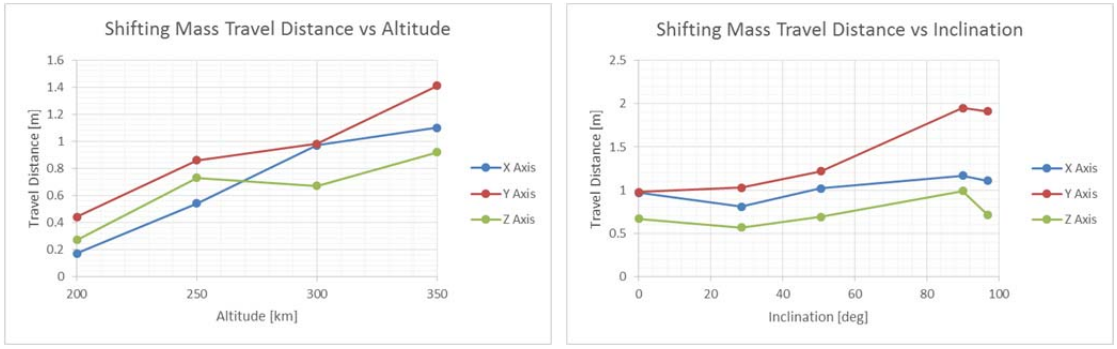

Figure 70. Shifting Mass Travel Distance versus Altitude and Inclination

Travel distances of all shifting masses increase as the altitude increases (Figure 70) due to longer detumbling maneuver times (Figure 68).

Even though the proposed attitude control methodology is better at lower altitudes, one should consider the other varying mission parameters with the decreasing altitude. First, the mission lifetime gets shorter as altitude decreases. To give some metric values, the ballistic coefficient of Shift-Mass Sat is used for lifetime calculations [19]. The lifetime drops from three months to a couple of days as altitude goes from 350 to 200 km (Figure 71). On the other hand, the resolution of the imaging payload improves. With the attributes of the camera used in Shift-Mass Sat, GSD changes from 5.3 to 9.3 meters as altitude rises from 200 to 350 km (Figure 71).

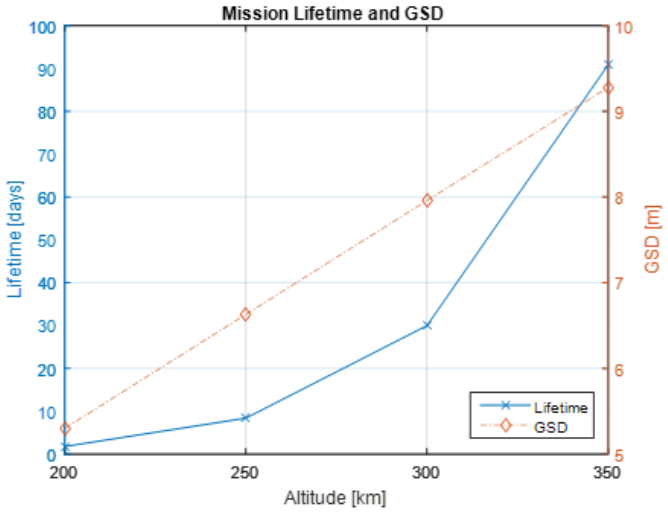

Figure 71. Mission Lifetime and GSD versus Altitude

The other varying parameters can be categorized as advantageous and disadvantageous with decreasing altitude. In the advantageous category, the pointing error's effect on GSD, revisit times, signal-to-noise ratio, launch costs, and orbital debris considerations can be added. In the disadvantageous category, coverage on ground, exposure time, and average time in view can be counted.

Overall, the effect of the altitude on mission is highly dependent on the mission characteristics. However, one should consider the effects mentioned above under the fact that shifting masses control system is highly effective at very low altitudes.

D. EXPLORATION OF THE MASS FRACTION OF THE SHIFTING MASSES

One of the main design attributes of the proposed attitude control methodology is the mass of the shifting masses. By definition with larger masses, the system can shift the CoM position in greater amounts which results in better control authority over the aerodynamic torque. However, in satellite designs, mass is crucial and should be minimized, especially in CubeSat. The mass of the CubeSat without the shifting masses is 2.6 kg as noted in the Shift-Mass Sat design. Different masses (50, 100, 150, 300 and 500 grams) are used to compare the performance of the attitude control.

Settling time decreases as the mass becomes larger. However, after 150 grams, the slope of decrease in settling time gets smaller (Figure 72). On the contrary, the steady-state error stays relatively similar (Figure 72) due to the same control parameter and equilibrium attitude as mentioned earlier.

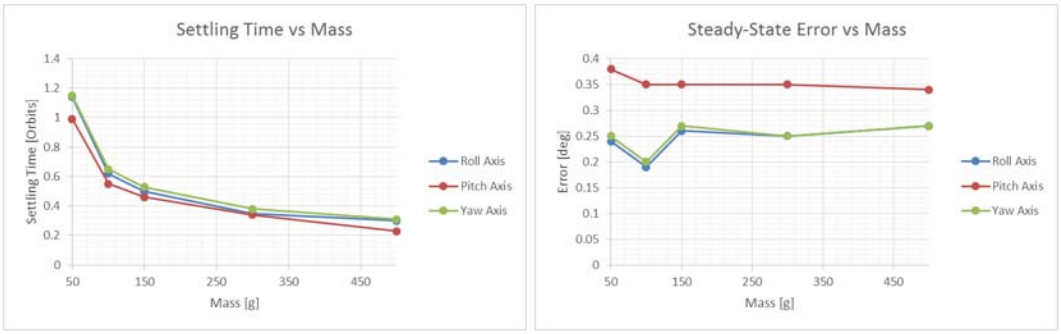

Figure 72. Settling Time and Steady-State Error versus Mass

Besides the faster detumbling, the other exploitable feature of the increasing mass is the travel distance. Travel distances in the x- and y-axes decrease dramatically with larger masses whereas the distance in the z-axis increases (Figure 73).

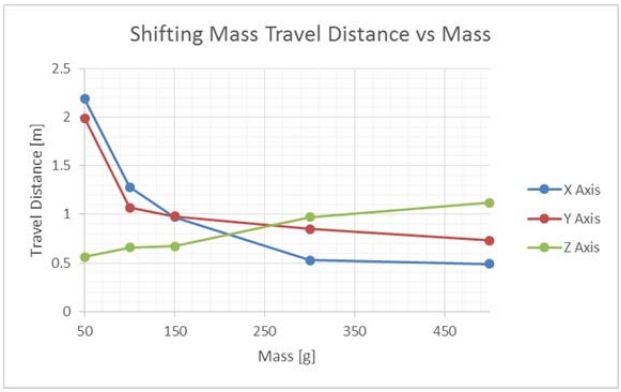

Figure 73. Shifting Mass Travel Distance versus Mass

The interesting result of different masses in terms of travel distance is more noticeable, when figures of shifting masses after stabilization are compared. As shown in Figure 73, after-stabilization shifting masses (150 grams) use ± 12 mm, while 300-gram-masses use ± 8 mm, which is 25% less (Figure 74). This means that if volume constraints are more important than the mass constraints in a particular CubeSat design, masses of the shifting masses should be increased to use shorter travel distances and eventually smaller volume.

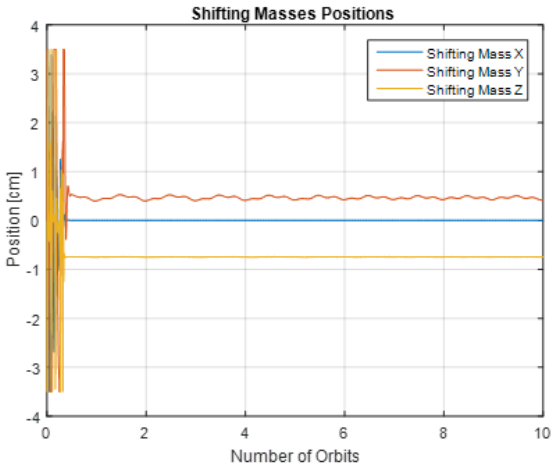

Figure 74. Shifting Masses Positions with 300-gram-Masses

E. THE EFFECTS OF THE ORIENTATION OF THE CUBESAT

In the baseline configuration orientation (vertical), the CubeSat's longitudinal axis (z-axis) is aligned with local vertical direction. For comparison purposes, the baseline configuration is simulated with a different orientation (horizontal) where longitudinal axis is aligned with local horizontal axis (Figure 75).

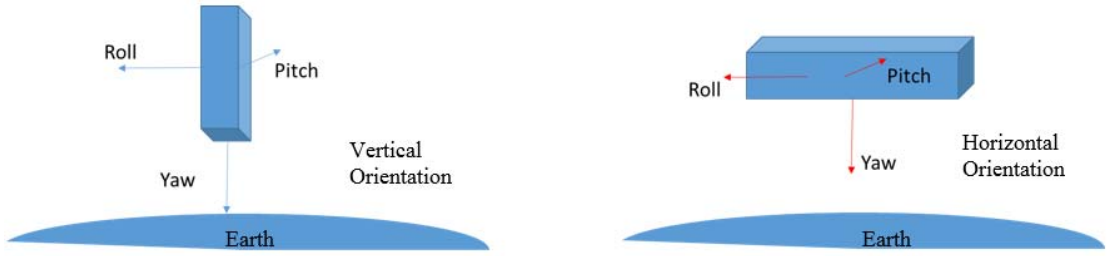

Figure 75. Vertical and Horizontal CubeSat Orientations

The horizontal orientation performs better by faster stabilization and better pointing accuracies at the expense of longer shifting masses travel distances (Table 10). Horizontal orientation is inherently aero-stable resulting in less disturbance effects on CubeSat. However, due to the smaller exposure area, aerodynamic torque is smaller resulting in more shifting mass travel distance than the vertical orientation (Table 10).

Table 10. Comparison between different CubeSat Orientations

	Angular Rate Settling Time [Orbits]			Steady State Error [deg]			Shifting Masses Travel Distance [m]		
	Roll	Pitch	Yaw	Roll	Pitch	Yaw	X-axis	Y-axis	Z-axis
Vertical Orientation	0.50	0.46	0.53	0.26	0.35	0.27	0.97	0.98	0.67
Horizontal Orientation	0.35	0.37	0.44	0.04	0.13	0.11	1.12	1.86	1.02

In addition to attitude control advantages, with a smaller area of exposure to the drag, the horizontal orientation's lifetime is longer than the vertical orientation (Figure

76). Lifetime considerations are very important in VLEO altitudes since lifetimes are only several months long.

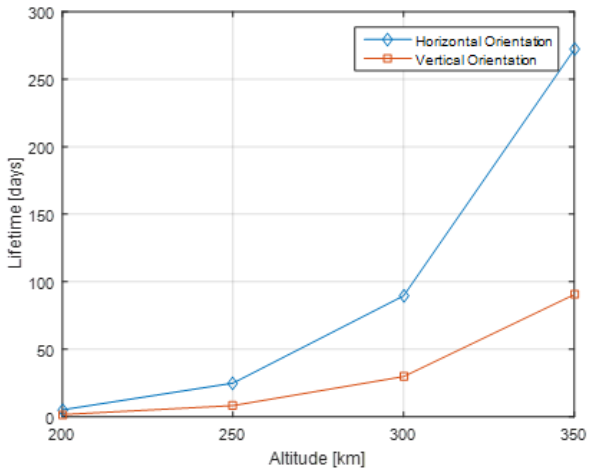

Figure 76. Mission Lifetime for Different CubeSat Orientations

F. THE EFFECTS OF INERTIAL PARAMETERS

Regarding inertial properties, as mentioned earlier, the baseline configuration uses the Shift-Mass Sat inertial parameters ($I_z>I_x>I_y$). To examine the inertial parameter's effects on the control methodology, one homogeneous 3U CubeSat (Ix=Iy>Iz) and one homogeneous 6U CubeSat ($I_y>I_x>I_z$) are simulated. In the 6U configuration, mass, inertia, and geometric parameters are scaled up.

Table 11. Comparison of CubeSat Configurations with Different Inertial Parameters

	Angular Rate Settling Time [Orbits]			Shifting Masses Travel Distance [m]		
	Roll	Pitch	Yaw	X-axis	Y-axis	Z-axis
Shift-Mass Sat	0.50	0.46	0.53	0.97	0.98	0.67
Homogeneous 3U	0.50	0.59	0.50	0.88	2.17	1.10
Homogeneous 6U	1.32	1.45	1.32	2.49	4.19	1.18

The higher inertias have more kinetic energy when initial angular velocities are the same. Higher kinetic energy means longer damping times, noticeable in Table 11. Between 3U configurations, a homogeneous CubeSat has a larger inertia at the pitch axis that results in an increase in both settling time and shifting mass travel distance. The obvious example is the 6U configuration; all MoE values are dramatically increased. Because scaling up the mass and area exposed to the aerodynamic force does not compensate, the inertia grows. This means that the proposed attitude control methodology is feasible when the spacecraft has small inertia parameters. In other words, the method is more effective for small spacecraft.

G. THE EFFECT OF THE COM LOCATION OF THE ORIGINAL SYSTEM

The CoM of a satellite can be at any location with respect to the geometric center of the structure. For reduction in the environmental disturbances, designers aim the location of the CoM at the geometric center. Due to the uncertainties and tolerances of the manufacturing process and inevitable component placements, the CoM is generally out of the geometric center.

With the proposed attitude control methodology, the CoM is adjustable. However, the envelope of the shift in CoM is very limited due to the small mass fraction of shifting masses to the satellite. As shown in Chapter III, in this study the range is ±1.82 mm (Figure 44). Therefore, for the configurations having a CoM within that envelope, shifting masses can alter both direction and magnitude of the aerodynamic torque. Otherwise, they can only change the magnitude while being able to damp the rotational kinetic energy to an attitude in which CoM and CoP is aligned with aerodynamic force direction where torque is zero. This results in a biased equilibrium attitude (Figure 77) that may be used for the targeting or tracking maneuvers.

The equilibrium attitude can be found in the geometry of the structure (Figure 77). Regarding the aerodynamic torque, when CoM and CoP are aligned with the relative wind direction, the system does not experience any aerodynamic torque. Since our control logic is based on the elimination of the aerodynamic torque, the final attitude of

the satellite is expected to be in such an orientation that the CoM and CoP are aligned with relative wind direction. The equilibrium attitude is calculated using trigonometry.

$$\theta_{equlibrium} = \tan^{-1}(CoM_Z / CoM_X)$$
$$\psi_{equlibrium} = -\tan^{-1}(CoM_Y / CoM_X) \quad (4.51)$$

Equation 4.51 shows that the relatively larger CoM position at the x-axis decreases the $\theta_{equlibrium}$ and $\psi_{equlibrium}$; in other words, making the satellite more aero-stable. The basic geometry calculation is consistent with the simulation results for different y- and z-axes CoM locations (Figure 78).

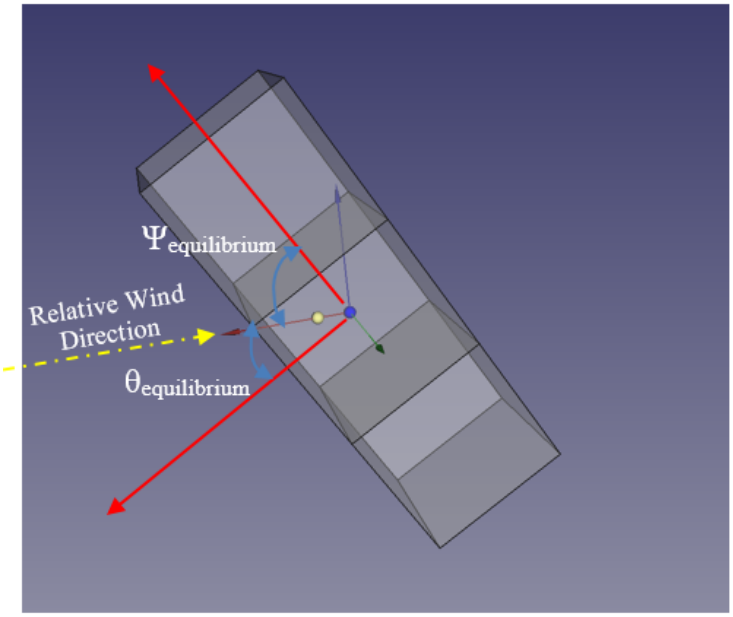

Figure 77. Geometric Illustration of the CoM Displacement Effect on Attitude Equilibrium Point

The blue sphere is used for CoP location and the yellow sphere for CoM location. The system finds its equilibrium point when CoM and CoP are aligned with relative wind direction. Then, pitch and yaw equilibrium angles are calculated using trigonometry.

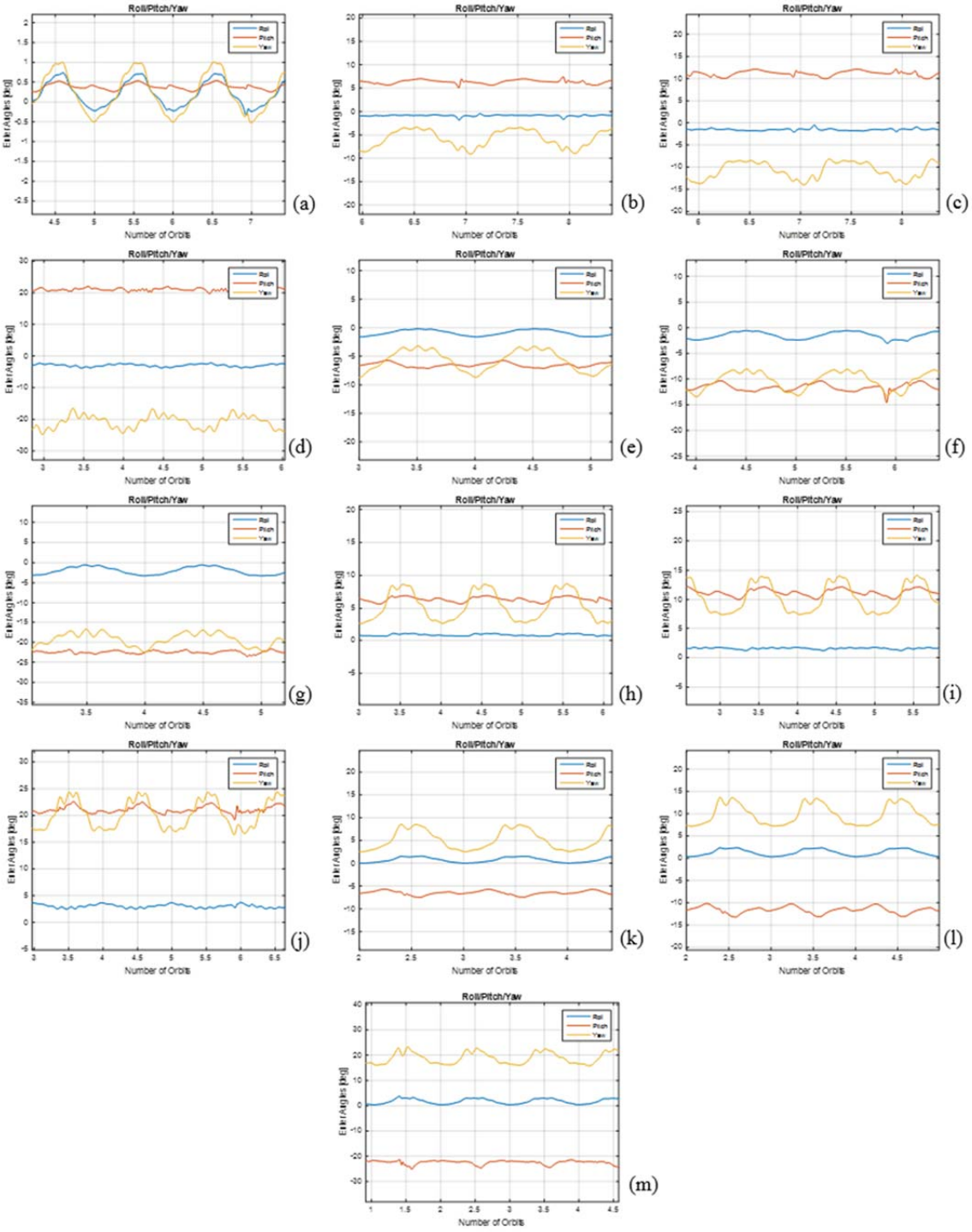

Figure 78. The Effect of CoM Location of the Original System on Equilibrium Attitude

CoM Locations in mm: (a) [18; 0; 0], (b) [18; 2; 2], (c) [18; 4; 4], (d) [18; 8; 8], (e) [18; 2; -2], (f) [18; 4; -4], (g) [18; 8; -8], (h) [18; -2; 2], (i) [18; -4; 4], (j) [18; -8; 8], (k) [18; -2; -2], (l) [18; -4; -4], and (m) [18; -8; -8].

H. BEHAVIOR OF THE SYSTEM WITH DIFFERENT INITIAL ANGULAR DISPLACEMENT AND RATE

In the baseline configuration, it is assumed that body and orbital triads are aligned, meaning that there is no angular displacement between both reference triads, but in reality, this is a hard assumption. So, the behavior of the system with an initial displacement angle is explored in this part of the study. During the angular displacement trials, the initial angular rate between body and orbital triads is zero, meaning that initial angular velocity of body triad relative to inertial triad is

$$\vec{\omega}_{BN_0} = \begin{bmatrix} 0 & -\sqrt{\mu / R_{Orbit}^3} & 0 \end{bmatrix}$$

where the y-component of angular velocity is the pitching movement of the orbital triad itself. Moreover, with the angular displacement angles greater than 5 degrees, the system's response is tested out of the small angle area, where all linearization processes took place. Displacement angles shown in Table 12 are in every axis. As shown in Table 12, the nadir-fixed pointing is achieved with a final stable attitude. Settling times and shifting masses travel distances increase, as the displacement angle gets larger.

Table 12. Behavior of the System with Different Initial Displacement Angles

	Angular Rate Settling Time [Orbits]			Steady State Error [deg]			Shifting Masses Travel Distance [m]		
	Roll	Pitch	Yaw	Roll	Pitch	Yaw	X-axis	Y-axis	Z-axis
0 degree	0.09	0.03	0.09	0.27	0.35	0.28	0.002	0.077	0.078
5 degrees	0.15	0.05	0.15	0.38	0.24	0.39	0.11	0.73	0.66
15 degrees	0.15	0.07	0.20	0.59	0.10	0.61	0.01	0.81	0.66
30 degrees	0.18	0.12	0.24	0.82	0.45	0.85	0.32	1.17	0.87
60 degrees	0.22	0.19	0.56	1.02	0.57	1.06	0.97	1.52	1.35

In regard to initial angular rate of the spacecraft, different orders of magnitudes are tested to see the detumbling performance and authority of the attitude control system. The baseline configuration's angular rate was 0.01 rad/s in every axis, 0.1 and 1 rad/s angular rates are also tested in this part of the study (Figure 79).

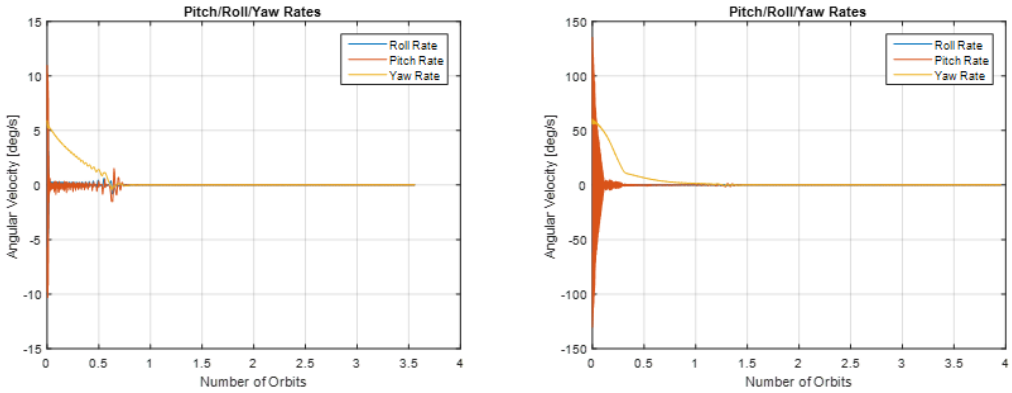

Figure 79. Initial Angular Rate Trials

The left and right figures represent 0.1 and 1 rad/s initial angular rate in every axis, respectively.

The settling time of the system is 0.73 orbits for 0.1 rad/s initial angular rate (Figure 79) which is 38% longer than the baseline configuration's settling time (Figure 55). For 1 rad/s initial angular rate (Figure 79), the settling time of the system becomes 1.4 orbits that are 164% longer than the settling time of baseline configuration. Overall, the attitude control system is capable of detumbling the CubeSat from angular velocities up to 1 rad/s and maintain the pointing with less than 1-degree pointing accuracy.

THIS PAGE INTENTIONALLY LEFT BLANK

VI. CONCLUSION AND FUTURE RECOMMENDATIONS

In this study, an attitude control methodology exploiting the aerodynamic disturbance torque with shifting masses was studied. The attitude methodology was developed and tested with a high fidelity simulation environment and model. In the simulation environment, aerodynamic force attributes were modeled to mimic real life by using atmospheric density and horizontal wind models along with the co-rotation of the Earth's atmosphere. In addition, the dynamics of the model were formed considering the dynamics of the shifting masses along with the satellite's rotational dynamics that resulted in nonlinear equations of motion.

The nonlinear equations of motion were linearized to implement a linear control law with optimal gain parameters of LQR control. In addition, the gain scheduling concept was adopted to cover the entire spectrum of initial conditions and to maintain better pointing accuracy after detumbling. In the control block, the dynamics of the shifting masses and high fidelity aerodynamic information were kept unknown. The system's capability to compensate those disturbances and uncertainties were tested with various simulations.

After all, the proposed attitude control methodology with shifting masses using a linear control law was able to detumble the CubeSat from the various initial angular displacement and rates. The mission orbit's characteristics were successful up to 350 km for all inclinations. In addition, the mass fraction of the system was shown to be scalable in the expense of the settling time and steady-state error for small spacecraft. For volume-constrained missions, higher mass fractions were proved to be more viable.

CubeSat mission analysis showed that the number of the launched CubeSats has been increasing and will likely continue to increase in the future. In addition, the variety of the missions has increased, and they have become more demanding missions in terms of ADCS performances. The altitude choice of a particular mission is not in the scope of this study; however, the launched CubeSat mission analysis showed that all CubeSats launched into LEO and a significant number of them are below 450 km, which is

considered as VLEO. The proposed attitude control methodology is becoming more effective as altitude decreases which is consistent with the CubeSat mission analysis results. Even though the lifetime and external disturbances get disadvantageous for satellite operations, the resolution, revisit times, and launch costs get advantageous. Moreover, the higher the external disturbances are, the better the proposed attitude control methodology is. This particular attitude control system may suit well for short-lived, dedicated, fast, and low-altitude missions that may be requested from the commercial imaging or tactical-level military worlds.

In addition, the use of shifting masses instead of reaction wheels for less than 1-degree pointing accuracy will eliminate the jitter issue due to the rotation of the wheels with a relatively less expensive and lighter solution. The Shift-Mass Sat design study showed that three COTS shifting mass linear actuators could fit within 1U of a CubeSat with 70 mm of useful travel distance. The proof of the practicality and realization of the shifting masses use as a control actuator in a fully-designed 3U CubeSat enabled us to process the simulation and modeling phases with more accurate CubeSat and shifting masses parameters.

For further study and recommendations, the dynamics of shifting masses can be integrated into the control law for making the shifting masses control system fully-actuated. Kumar's method [42] of using movable masses can be used for the roll axis (under-actuated axis) while the proposed attitude control method in this thesis can be used for the pitch and yaw axes, even though the dynamics of shifting masses impose a conservative force over the spacecraft. The dynamics effect can be used not just for full actuation but also for better estimating the response of the system. In addition, the CoM dislocation for tracking or targeting purposes can be studied with the use of shifting masses as the control actuator.

Moreover, reaction wheels can be used as shifting masses by mounting the reaction wheels on linear actuators. Shifting reaction wheels, in this configuration, can relieve reaction wheels' burden for counteracting the disturbance torques or be used as momentum dumping solutions.

In addition, the control system can be tested with hardware-in-the-loop simulations. A floating CubeSat with shifting mass actuators can be tested on a zero-friction testbed. Aerodynamic force can be derived from the simulation model and realized by different means of apparatus such as weights and pulleys, and magnetic torquers.

THIS PAGE INTENTIONALLY LEFT BLANK

APPENDIX A. LAUNCHED CUBESAT MISSION ANALYSIS DATA

As stated in Chapter II, all individual launched CubeSat missions were studied in terms of their sizes, attitude control methodologies, mission types and altitudes in order to cue our simulation environment and the Shift-Mass Sat design.

The baseline of the CubeSat mission analysis is the work of Swartwout from Saint Louis University Space Systems Research Laboratory [44]. The Swartwout database is used for satellite names, launch years, sizes, and mission status. Even though the database has mission types, some mission types are changed according to this analysis's classification rules (Chapter II). In addition, Swartwout's mission status enumeration is adopted as is (Chapter II).

The information about the individual missions were gathered from official mission websites or relevant academic publications, if present, otherwise from online databases [45], [46], and [47]. There is some missing information in the analysis data that could not be found on publicly accessible documents. Thus, those cells were called N/A (not available). In addition, the altitude information for those missions that did not reach into orbit were entered as planned mission altitude.

Table 13. Launched CubeSat Missions List

S/N	Launch Year	Satellite Name	Mission Type	Size	Attitude Control System	Orbit Altitude	Mission Status	Remarks
1	2002	MEPSI	Tech Demo	2U	Cold Gas Propulsion	225 km	2	Two-tethered CubeSat
2	2003	AAU CUBESAT 1	Tech Demo	1U	3 x Torque Coils	900 km	2	Imaging
3	2003	CANX-1	Tech Demo	1U	3 x Torque Coils	650 km	2	ADS, OBC and imaging
4	2003	CUBESAT XI-IV	N/A	1U	N/A	820 km	4	N/A
5	2003	CUTE-1	Tech Demo	1U	No ACS	820 km	3	Solar Deployment, Sensors, COMM
6	2003	DTUSAT 1	Tech Demo	1U	3 x Torque Coils	820 km	2	Changing altitude with mag. forces of tethers
7	2003	QUAKESAT 1	Scientific	3U	Passive Magnetic Control	820 km	5	Observing ELF EMW to study earthquakes
8	2005	CUBESAT XI-V	N/A	1U	N/A	700 km	5	N/A
9	2005	NCUBE 2	Tech Demo	1U	Gravity Gradient	686 km	2	AIS
10	2005	UWE-1	Tech Demo	1U	Spin Stab., Passive Magnetic Control	700 km	3	Internet protocol networking
11	2006	CUTE 1.7	Tech Demo	2U	3 x Torque Coils	185x800 km	2	ACS, APD Sensor Payload
12	2006	AEROCUBE 1	N/A	1U	N/A	500 km	1	N/A
13	2006	CP 1	Tech Demo	1U	3 x Torque Coils	500 km	1	Sun sensor, ACS
14	2006	CP 2	N/A	1U	N/A	500 km	1	N/A
15	2006	HAUSAT 1	Tech Demo	1U	N/A	500 km	1	Formation flight, Sun sensor, GPS

16	2006	ICECUBE 1	Scientific	1U	N/A	500 km	1	Ionospheric scintillation
17	2006	ICECUBE 2	Scientific	1U	N/A	500 km	1	Ionospheric scintillation
18	2006	ION	Scientific Tech Demo	2U	3 x Torque Coils	500 km	1	Micro-vacuum arc thruster
19	2006	KUTESAT Pathfinder	Tech Demo	1U	3 x Torque Coils	500 km	1	CubeSat operation
20	2006	MEA HUAKA'L	Tech Demo	1U	Passive Magnetic Control	500 km	1	Active antenna use in space
21	2006	MEROPE	Scientific	1U	Passive Magnetic Control	500 km	1	Van Allen radiation belts
22	2006	NCUBE 1	Tech Demo	1U	Gravity Gradient	500 km	1	AIS
23	2006	RINCON 1	Tech Demo	1U	Spin Stabilized	500 km	1	COMM, relay satellite
24	2006	SACRED	Tech Demo	1U	Spin Stabilized	500 km	1	Radiation effects on electronics
25	2006	SEEDS	Tech Demo	1U	N/A	500 km	1	COMM
26	2006	HITSAT	Tech Demo	1U	Spin Stabilized 3 x Torque Coils	279x 648 km	4	On-orbit test of future MicroSat project
27	2006	GENESAT	Scientific	3U	Passive Magnetic Control	460 km	5	Microlab for bacteria
28	2006	MARSCOM	COMM	1U	Passive Magnetic Control	310 km	5	COMM
29	2006	MEPSI 2A	Tech Demo	2U	Cold Gas Propulsion	N/A	5	Two-tethered CubeSat
30	2006	RAFT	COMM	1U	Passive Magnetic Control	300 km	5	COMM
31	2007	AEROCUBE 2	Tech Demo	1U	N/A	640x757 km	2	N/A
32	2007	CAPE 1	Tech Demo	1U	3 x Torque Coils	646x793 km	3	COMM
33	2007	CP 3	Tech Demo	1U	3 x Torque Coils	646x793 km	2	ADCS
34	2007	CP 4	Tech Demo	1U	N/A	650 km	3	Energy dissipation
35	2007	CSTB 1	Tech Demo	1U	3 x Torque Coils	745 km	5	Standardized bus
36	2007	LIBERTAD 1	N/A	1U	N/A	646x792 km	2	N/A
37	2007	MAST	Tech Demo	3U	Cold Gas Thrusters	647x782 km	2	3-tethered CubeSat
38	2008	AAUSAT 2	Tech Demo Scientific	1U	3 x Torque Coils 3 x Momentum Wh.	635 km	5	ADCS, gamma-ray detector
39	2008	CANX 2	Tech Demo	3U	3 x Torque Coils 1 x Reaction Wheel	635 km	5	Cold gas propulsion for formation flight
40	2008	COMPASS 1	Tech Demo	1U	3 x Torque Coils	635 km	5	Imaging
41	2008	DELFI C3	Tech Demo	3U	Passive Magnetic Control	635 km	5	Solar cells, wireless sun sensor
42	2008	SEEDS 2	Tech Demo	1U	No ACS	635 km	5	COMM
43	2008	NANOSAIL D	Tech Demo	3U	Passive Magnetic Control	685x330 km	1	Solar Sail
44	2008	PRESAT	Tech Demo	3U	N/A	685 km	1	Pre-mission of PharmaSat
45	2008	PSSC-1 TESTBED 1	Tech Demo	2U	Spin Stabilized Momentum Wheel 3 x Torque Coils	N/A	5	Solar cell tester
46	2009	KKS-1	Tech Demo	1U	3-axis Micro-thruster	670 km	3	3-axis attitude control, micro-thrusters
47	2009	AEROCUBE 3	Tech Demo	1U	1-axis Reaction Wheel	432x467 km	3	Imaging final stage of launch
48	2009	CP 6	Tech Demo	1U	N/A	432x467 km	4	ADS, electron counting mechanism
49	2009	HAWKSAT 1	Tech Demo	1U	N/A	432x467 km	2	Space qualification of COTS materials
50	2009	PHARMASAT	Scientific	3U	N/A	432x467 km	5	Monitoring yeast properties
51	2009	BEVO 1	Tech Demo	1U	N/A	325x332 km	2	Docking and rendezvous
52	2009	DRAGONSAT 2	Tech Demo	1U	N/A	325x332 km	4	Docking and rendezvous
53	2009	BEESAT	Tech Demo	1U	3 x Reaction Wheels 6 x Torque Coils	720 km	5	Microwheels for ADCS
54	2009	ITU-PSAT 1	Tech Demo	1U	Passive Magnetic Control	720 km	2	Imaging, ADCS
55	2009	SWISSCUBE	Scientific	1U	3 x Torque Coils	720 km	4	Oxygen airglow
56	2009	UWE-2	Tech Demo	1U	Passive Magnetic Control	720 km	2	ADS
57	2010	HAYATO	N/A	1U	N/A	N/A	2	N/A
58	2010	NEGAI-STAR	Tech Demo	1U	N/A	300 km	5	On-board processing
59	2010	WASEDA-SAT2	Tech Demo	1U	N/A	300 km	2	Moving paddles to change CoP and drag

60	2010	STUDSAT	Tech Demo	1U	3 x Torque Coils	635 km	2	CubeSat operations
61	2010	TISAT 1	Tech Demo	1U	Passive Magnetic Control	635 km	5	Material degradation
62	2010	O/OREOS	Scientific	3U	Passive Magnetic Control	650 km	5	Astrobiology
63	2010	RAX 1	Scientific	3U	Passive Magnetic Control	650 km	4	Magnetic field-aligned irregularities
64	2010	MAYFLOWER-CAERUS	Tech Demo	3U	4 x Torque Coils	300 km	2	N/A
65	2010	PERSEUS 000	Tech Demo	1.5U	N/A	279x308 km	5	Fast delivery to space
66	2010	PERSEUS 001	Tech Demo	1.5U	N/A	279x308 km	5	Fast delivery to space
67	2010	PERSEUS 002	Tech Demo	1.5U	N/A	279x308 km	5	Fast delivery to space
68	2010	PERSEUS 003	Tech Demo	1.5U	N/A	279x308 km	5	Fast delivery to space
69	2010	QBX 1	Tech Demo	3U	3 x Reaction Wheels 3 x Torque Coils	300 km	5	On-orbit experimentation
70	2010	QBX 2	Tech Demo	3U	3 x Reaction Wheels 3 x Torque Coils	300 km	5	On-orbit experimentation
71	2010	SMDC-ONE 1	COMM	3U	Passive Magnetic Control	300 km	5	Relay satellite constellation
72	2011	NANOSAIL-D-002	Tech Demo	3U	Passive Magnetic Control	650 km	5	Solar sail deployment
73	2011	E1P	Scientific	1U	Passive Magnetic Control	820 km	1	Explorer mission
74	2011	HERMES	Tech Demo	1U	Passive Magnetic Control	N/A	1	High speed COMM
75	2011	KYSAT 1	Tech Demo	1U	N/A	705 km	1	Educational
76	2011	PSSC-2	Tech Demo	2U	3 x Reaction Wheels 3 x Torque Coils Thrusters	350 km	5	Thrusters, MTV, CTECS
77	2011	JUGNU	Earth Observation	3U	4 x Reaction Wheels 3 x Torque Coils	860 km	4	N/A
78	2011	AUBIESAT1	Tech Demo	1U	N/A	N/A	3	Solar panels
79	2011	DICE 1	Scientific	1.5U	Spin Stabilized 3 x Torque Coils	820x400 km	5	Ionosphere plasma density and electric field
80	2011	DICE 2	Scientific	1.5U	Spin Stabilized 3 x Torque Coils	820x400 km	5	Ionosphere plasma density and electric field
81	2011	HRBE	Scientific	1U	Passive Magnetic Control	820 km	1	Explorer mission
82	2011	M-CUBED	Earth Observation	2U	Passive Magnetic Control	458x816 km	2	Mid-resolution imaging
83	2011	RAX-2	Scientific	3U	Passive Magnetic Control	820x400 km	5	Space weather
84	2012	E-ST@R	Tech Demo	1U	3 x Torque Coils	354x1450km	2	ADCS
85	2012	GOLIAT	Scientific	1U	2 x Momentum Wheel	354x1450km	2	Radiation, micrometeorites
86	2012	MASAT-1	Tech Demo	1U	3 x Torque Coils	354x1450km	5	On-board avionics
87	2012	PW-SAT 1	N/A	1U	N/A	N/A	2	N/A
88	2012	ROBUSTA	Tech Demo	1U	N/A	N/A	2	Low dose radiation
89	2012	UNICUBESAT-GGS	Tech Demo	1U	Gravity Gradient Boom	N/A	2	Gravity Gradient
90	2012	XATCOBEO	Tech Demo	1U	No ACS	354x1450km	5	Deployable solar panel, measuring ionizing radiation
91	2012	AENEAS	Earth Observation	3U	3 x Reaction Wheels 3 x Torque Coils	770x480 km	3	Tracking containers
92	2012	AEROCUBE 4.0	Tech demo	1U	3 x Reaction Wheels 3 x Torque Coils	770x480 km	5	Formation flight, imaging
93	2012	AEROCUBE 4.5A	Tech demo	1U	3 x Reaction Wheels 3 x Torque Coils	770x480 km	5	Movement of solar panels for altering ballistic coefficient
94	2012	AEROCUBE 4.5B	Tech demo	1U	3 x Reaction Wheels 3 x Torque Coils	770x480 km	5	Movement of solar panels for altering ballistic coefficient
95	2012	CINEMA 1	Scientific	3U	Spin Stabilized 2 x Torque Coils	770x480 km	3	Stereo ENA imaging of ring current
96	2012	CP 5	Tech Demo	1U	N/A	770x480 km	3	Deorbiting with deployable thin film
97	2012	CSSWE	Scientific	3U	Passive Magnetic Control	770x480 km	5	Space weather
98	2012	CXBN	Scientific	2U	Spin Stabilized 3 x Torque Coils	770x480 km	3	Cosmic x-ray background

99	2012	RE (STARE)	Tech Demo	3U	3 x Reaction Wheels 3 x Torque Coils	500 km	3	Space situational awareness
100	2012	SMDC ONE 1.1	COMM	3U	Passive Magnetic Control	770x480 km	5	Relay satellite constellation
101	2012	SMDC ONE 1.2	COMM	3U	Passive Magnetic Control	770x480 km	5	Relay satellite constellation
102	2012	F1	Earth Observation	1U	Passive Magnetic Control	420 km	2	Low-resolution imaging
103	2012	FITSAT-1	Tech Demo	1U	Passive Magnetic Control	420 km	5	COMM
104	2012	RAIKO	Tech Demo	2U	3 x Torque Coils	420 km	5	Fisheye camera
105	2012	TECHEDSAT	Tech Demo	1U	Passive Magnetic Control	350 km	4	Satellite-to-satellite COMM
106	2012	WE WISH	Tech Demo	1U	N/A	420 km	2	IR Camera
107	2013	AAUSAT 3	Earth Observation	1U	3 x Torque Coils	780 km	5	AIS
108	2013	STRAND-1	Tech Demo	3U	3 x Reaction Wheels 3 x Torque Coils	786 km	4	Smartphone technology in space
109	2013	BEESAT 2	Tech Demo	1U	3 x Reaction Wheels 3 x Torque Coils	557x581 km	4	Improve the RWs control in CubeSat
110	2013	BEESAT 3	Tech Demo	1U	Passive Magnetic Control	557x581 km	2	Highly integrated S-band transmitter
111	2013	DOVE 2	Tech Demo	3U	3 x Torque Coils	575 km	5	Remote sensing (4.4 m GSD)
112	2013	OSSI 1	COMM	1U	N/A	600 km	2	Open source satellite Comm initiative
113	2013	SOMP	Scientific	1U	3 x Torque Coils Passive Magnetic Control	600 km	3	Measuring Oxygen in upper atmosphere
114	2013	ALEXANDER (PHONESAT 1A)	COMM	1U	N/A	250 km	5	Smartphone technology in space
115	2013	BELL (PHONESAT 1C)	COMM	1U	N/A	250 km	5	Smartphone technology in space
116	2013	DOVE 1	Tech Demo	3U	3 x Reaction Wheels 3 x Torque Coils	250 km	5	Remote sensing
117	2013	GRAHAM (PHONESAT 1B)	COMM	1U	N/A	250 km	5	Smartphone technology in space
118	2013	CUBEBUG-1	Tech Demo	2U	Nano Reaction Wheel	630 km	4	Open source demo
119	2013	NEE 01 PEGASO	Tech Demo	1U	N/A	630 km	4	Transmission of video/ audio
120	2013	TURKSAT 3USAT	COMM	3U	Passive Magnetic Control	630 km	3	COMM
121	2013	ESTCUBE-1	Tech Demo	1U	3 x Torque Coils	670 km	4	Electronic solar wind test
122	2013	POPACS 1/2/3	Tech Demo	3U	N/A	324x1480 km	4	Launch platform
123	2013	ARDUSAT 1	Scientific	1U	N/A	N/A	3	Open source on-board experiments (Sandbox)
124	2013	ARDUSAT X	Scientific	1U	N/A	N/A	4	Open source on-board experiments (Sandbox)
125	2013	PICODRAGON	Tech Demo	1U	N/A	410 km	4	Imaging, COMM, telemetry
126	2013	BLACK KNIGHT	Tech Demo	1U	N/A	500 km	2	Education in CubeSat
127	2013	CAPE 2	Tech Demo	1U	N/A	400 km	4	Text to speech, digipeater COMM
128	2013	CHARGERSAT	Tech Demo	1U	Gravity Gradient	500 km	2	COMM, passive nadir axis stabilization
129	2013	COPPER	Earth Observation	1U	N/A	500 km	2	Micro bolometers, rad. measurements
130	2013	DRAGONSAT	Earth Observation	1U	Gravity Gradient	350 km	2	Imaging, auroras Rad. measurements due to solar activity
131	2013	FIREFLY	Scientific	3U	Gravity Gradient 3 x Torque Coils	500 km	4	Lightning related gamma-ray bursts
132	2013	HO'OPONOPONO-2	Military	3U	Deployable Boom	330 km	2	Radar calibrating service
133	2013	HORUS	Military	3U	3 x Reaction Wheels	770x480km	2	Space situational awareness
134	2013	KYSAT II	Earth Obsv.	1U	Passive Magnetic Control	500 km	4	Imaging

135	2013	LUNAR	Tech Demo	1U	Gimbaled Ion Thruster, Differential Chemical Thruster	500 km	4	Possible Lunar orbits or/and landing
136	2013	NPS-SCAT	Tech Demo	1U	N/A	500 km	3	Solar cell tester
137	2013	ORS TECH 1	Military	3U	Pitch-axis Momentum Wheel, 4 x Torque Coils	500 km	4	ORS
138	2013	ORS TECH 2	Military	3U	Pitch-axis Momentum Wheel, 4 x Torque Coils	500 km	4	ORS
139	2013	ORSES	Military	3U	N/A	500 km	4	SATCOMM
140	2013	PHONESAT 2.4	COMM	1U	6 x Torque Coils 3 x Reaction Wheels	N/A	3	Smartphone technology in space
141	2013	PROMETHEUS 1.1	Military	1.5U	N/A	500 km	4	Special-ops COMM, deployable helix antenna
142	2013	PROMETHEUS 1.2	Military	1.5U	N/A	500 km	4	Special-ops COMM, deployable helix antenna
143	2013	PROMETHEUS 2.1	Military	1.5U	N/A	500 km	4	Special-ops COMM, deployable helix antenna
144	2013	PROMETHEUS 2.2	Military	1.5U	N/A	500 km	4	Special-ops COMM, deployable helix antenna
145	2013	PROMETHEUS 3.1	Military	1.5U	N/A	500 km	4	Special-ops COMM, deployable helix antenna
146	2013	PROMETHEUS 3.2	Military	1.5U	N/A	500 km	4	Special-ops COMM, deployable helix antenna
147	2013	PROMETHEUS 4.1	Military	1.5U	N/A	500 km	4	Special-ops COMM, deployable helix antenna
148	2013	PROMETHEUS 4.2	Military	1.5U	N/A	500 km	4	Special-ops COMM, deployable helix antenna
149	2013	SENSE SV1	Military	3U	4 x Reaction Wheels 3 x Torque Coils	500 km	4	Space weather
150	2013	SENSE SV2	Military	3U	4 x Reaction Wheels 3 x Torque Coils	500 km	4	Space weather
151	2013	SPA-1 TRAILBLAZER	Tech Demo	1U	Passive Magnetic Control	500 km	2	Bus design
152	2013	SWAMPSAT	Tech Demo	1U	4 x single gimbaled CMGs in pyramidal structure	500 km	2	Pyramidal CMGs
153	2013	TECHEDSAT-3	Tech Demo	3U	N/A	N/A	4	Exosphere brake passive de-orbit system
154	2013	TJSAT	Tech Demo	1U	N/A	500 km	2	Educational high school project
155	2013	CINEMA 2 (KHUSAT-1)	Scientific	3U	Spin Stabilized 2 x Torque Coils	N/A	2	High sensitivity mapping of ENA
156	2013	CINEMA 3 (KHUSAT-2)	Scientific	3U	Spin Stabilized 2 x Torque Coils	N/A	2	High sensitivity Mapping of ENA
157	2013	CUBEBUG 2	Tech Demo	2U	N/A	N/A	4	Antenna, solar panels, camera, GPS
158	2013	DELFI-N3XT	Tech Demo	3U	3 x Reaction Wheels 3 x Torque Coils	N/A	4	ADCS, COMM
159	2013	DOVE 4	Tech Demo	3U	3 x Torque Coils	700 km	1	Remote sensing
160	2013	FIRST-MOVE	Tech Demo	1U	Passive Magnetic Cont	630 km	3	Standard bus modules
161	2013	FUNCUBE 1	COMM	1U	N/A	670 km	4	Educational
162	2013	GATOS (GOMX 1)	Earth Observation	2U	3 x Torque Coils	600 km	4	Air traffic control surveillance
163	2013	HINCUBE	Earth Observation	1U	3 x Torque Coils	N/A	2	AIS, imaging
164	2013	HUMSAT D	COMM	1U	No ACS	N/A	4	Relay satellite
165	2013	ICUBE 1	Earth Observation	1U	Passive Magnetic Cont	N/A	2	Low Resolution Imaging
166	2013	NEE 02 KRYSAOR	N/A	1U	N/A	N/A	4	N/A

167	2013	OPTOS-26	Tech Demo	3U	5 x Torque Coils 2 x Reaction Wheels	670 km	2	Imaging (30 m GSD), data handling
168	2013	PUCP-SAT 1	Tech Demo	1U	N/A	600 km	3	Deploy pocket satellites
169	2013	TRITON 1	Earth Observation	3U	N/A	N/A	3	AIS
170	2013	UWE 3	Tech Demo	1U	3 x Torque Coils 3 x Reaction Wheels	N/A	4	ADCS
171	2013	VELOX-P 2	Tech Demo	1U	3 x Torque Coils	N/A	4	N/A
172	2013	ZACUBE 1	Scientific	1U	3 x Torque Coils	N/A	4	Ionospheric UHF testing, Radar calibration
173	2013	AERO-CUBE 5A	Tech Demo	1U	N/A	N/A	4	N/A
174	2013	AERO-CUBE 5B	Tech Demo	1U	N/A	N/A	4	N/A
175	2013	ALICE	Tech Demo	3U	N/A	N/A	4	Orbital maneuver with electric propulsion
176	2013	CUNYSAT	Tech Demo	1U	N/A	N/A	2	Spins and propulsion systems
177	2013	FIREBIRD 1	Scientific	1.5U	Passive Magnetic Control	467x883km	4	Magnetospheric microbursts in Van Allen radiation belts
178	2013	FIREBIRD 2	Scientific	1.5U	Passive Magnetic Control	467x883km	4	Magnetospheric microbursts in Van Allen radiation belts
179	2013	IPEX	Tech Demo	3U	Passive Magnetic Control	N/A	4	N/A
180	2013	M-CUBED-2	Earth Observation	1U	Passive Magnetic Control	N/A	4	Mid-resolution images (200 m)
181	2013	SMDC-ONE 2.3	Military	3U	Passive Magnetic Control	300 km	4	COMM relay satellite
182	2013	SMDC-ONE 2.4	Military	3U	Passive Magnetic Control	300 km	4	COMM relay satellite
183	2013	SNAP 1	Tech Demo	1U	3 x Torque Coils Momentum Wheel	N/A	4	Orbit maneuvering
184	2013	TACSAT-6	Military	3U	N/A	N/A	4	ORS COMM
185 210	2014	FLOCK-1-01 FLOCK-1-26	Earth Observation	3U	3 x Torque Coils 3 x Reaction Wheels	370x430km	5	Imaging (3-5 m Res), largest constellation
211	2014	IFT 1(YUI)	Tech Demo	1U	N/A	N/A	2	Amateur radio COMM
212	2014	INVADER (CO-77)	Tech Demo	1U	N/A	N/A	5	Amateur Radio COMM, Imaging
213	2014	INVADER (CO-77)	Tech Demo	1U	N/A	N/A	5	Amateur Radio COMM, Imaging
214	2014	KSAT 2 (HAYATO 2)	Scientific	1U	N/A	N/A	3	Radio frequency water vapor detector
215	2014	OPUSAT (COSMOZ)	Tech Demo	1U	2 x Torque Coils Spin Stabilized	N/A	3	Hybrid solar systems, deployable panels
216	2014	ARDUSAT 2	Tec Demo	2U	N/A	N/A	2	Test-bed for software in space
217 218	2014	FLOCK-1-27 FLOCK-1-28	Earth Observation	3U	3 x Torque Coils 3 x Reaction Wheels	370x430km	5	Imaging (3-5 m Res), largest constellation
219	2014	LITSAT 1	Tech Demo	1U	N/A	N/A	5	Amateur radio COMM
220	2014	LITUANICAS AT 1	Tech Demo	1U	Passive Magnetic Control	N/A	4	COMM, imaging
221	2014	SKYCUBE	Earth Observation	1U	Passive Magnetic Control	N/A	2	COMM, imaging
222	2014	UAPSAT	Earth Observation	1U	Passive Magnetic Control	800 km	2	Meteorology
223	2014	ALL-STAR/ THEIA	Tech Demo	3U	3 x Reaction Wheels 3 x Torque Coils	300x400km	2	Optical imaging
224	2014	KICKSAT 1	Tech Demo	3U	Spin Stabilized	325x315km	3	Launching more small satellites (FemtoSats)
225	2014	PHONESAT 2.5	Tech Demo	1U	3 x Torque Coils 3 x Reaction Wheels	N/A	5	Smartphone technology in space
226	2014	SPORESAT	Scientific	3U	Passive Magnetic Control	400 km	5	Biology, gravity effects on spores
227	2014	TSAT	Scientific	2U	Using Booms for Aerodynamic Stab.	N/A	4	Low-altitude, ionosphere
228	2014	AEROCUBE 6A	Scientific	0.5U	3 x Torque Coils	620x480km	4	Radiation measurements with dosimeters
229	2014	AEROCUBE 6B	Scientific	0.5U	3 x Torque Coils	620x480km	4	Rad. Measurements with dosimeters

230	2014	ANTELSAT	Earth Observation	2U	3 x Torque Coils	630 km	4	Visible and near IR imaging
231	2014	DTUSAT 2	Earth Observation	1U	Gravity Gradient 3 x Torque Coils	400 km	2	Tracking small birds from space
232	2014	DUCHIFAT 1	COMM	1U	N/A	630 km	4	Omnidirectional antenna
233 243	2014	FLOCK-1C-01 FLOCK-1C-11	Earth Observation	3U	3 x Torque Coils 3 x Reaction Wheels	605x620km	4	Imaging (3-5 m Res), largest constellation
244	2014	LEMUR 1	Earth Observation	3U	N/A	630 km	N/A	Visible (5 meter), IR (1 km)
245	2014	NANOSATC-BR 1	Scientific	1U	Passive Magnetic Control	630 km	3	South Atlantic Anomaly, equatorial electro-jets
246	2014	PACE	Tech Demo	2U	3 x Torque Coils Momentum Wheel	600 km	2	Attitude control experimentation
247	2014	PERSEUS-M 1	Earth Observation	6U	N/A	620 km	4	Small maritime surveillance, AIS, (22 m Res.)
248	2014	PERSEUS-M 2	Earth Observation	6U	N/A	620 km	4	Small maritime surveillance, AIS, (22 m Res.)
249	2014	POLYITAN 1	Tech Demo	1U	N/A	620 km	4	ADS
250	2014	POPSAT-HIP	Earth Observation	3U	3 x Torque Coils 12 x Micro Thrusters	600 km	4	High-resolution optical payload, attitude control w/ propulsion
251	2014	QB50P1 (EO-79)	Tech Demo	2U	3 x Torque Coils Momentum Wheel	200 km	4	ADCS, lower Thermosphere observer
252	2014	QB50P2 (EO-80)	Tech Demo	2U	3 x Torque Coils Momentum Wheel	200 km	4	ADCS, lower thermosphere observer
253	2014	TIGRISAT	Tech Demo	3U	3 x Torque Coils	600x700km	4	Nadir pointing attitude control
254	2014	VELOX I-NSAT	Tech Demo	3U	3 x Torque Coils 3 x Reaction Wheels	650x700km	3	Imaging with extended aperture (20-meter Res.)
255	2014	UKUBE 1	Tech Demo	3U	3 x Torque Coils	635 km	4	Plasma sphere imaging, random number generator
256	2014	CHASQUI 1	Tech Demo	1U	3 x Torque Coils	N/A	2	Imaging
257 274	2014	FLOCK-1B	Earth Observation	3U	3 x Torque Coils 3 x Reaction Wheels	370x430km	4	Imaging (3-5 m Res.), largest constellation
275	2014	ARKYD-3	Tech Demo	3U	N/A	N/A	1	Space telescope
276 301	2014	FLOCK-1D	Earth Observation	3U	3 x Torque Coils 3 x Reaction Wheels	370x430km	1	Imaging (3-5 m Res.), largest constellation
302	2014	GOMX 2	Tech Demo	2U	N/A	N/A	1	De-orbit system, optical COMM
303	2014	RACE	Tech Demo	3U	Spin Stabilized	415 km	1	Radiometer
304	2015	EXOCUBE (CP10)	Scientific	3U	Gravity Gradient Momentum Wheel 3 x Torque Coils	400x670km	3	Measuring the elemental composition of exosphere
305	2015	FIREBIRD-IIA	Scientific	1.5U	Passive Magnetic Control	467x883km	4	Magnetospheric microbursts in Van Allen radiation belts
306	2015	FIREBIRD-IIB	Scientific	1.5U	Passive Magnetic Control	467x883km	4	Magnetospheric microbursts in Van Allen radiation belts
307	2015	GRIFEX	Tech Demo	3U	N/A	460x670km	4	High throughput circuit for GEO satellite
308	2015	AESP-14	Scientific	1U	N/A	397x450 km	2	Measuring electron density and temperature of ionospheric plasma
309 318	2015	FLOCK-1B FLOCK-1D	Earth Observation	3U	3 x Torque Coils 3 x Reaction Wheels	370x430km	4	Imaging (3-5 m Res.), largest constellation
319	2015	GEARRSAT	Tech Demo	3U	N/A	395x404 km	2	C2 in Space
320	2015	LAMBDASAT	Tech Demo	1U	N/A	N/A	3	N/A
321	2015	MICROMAS	Scientific	3U	Dual-Spin Stabilized 3 x Reaction Wheels	400 km	2	Radiometer for collecting atmospheric profile data
322	2015	TECHEDSAT 4 (TES 4)	Tech Demo	3U	N/A	393x402 km	2	N/A

323 324	2015	FLOCK-1B	Earth Observation	3U	3 x Torque Coils 3 x Reaction Wheels	370x430km	4	Imaging (3-5 m Res.), largest constellation
325	2015	USS LANGLEY	Tech Demo	3U	3 x Torque Coils 3 x Reaction Wheels	300 km	2	Host a web server
326 328	2015	OPTICUBE 1–2-3	Tech Demo	3U	N/A	355x700 km	N/A	Calibration service for orbital debris tracking
329	2015	PSAT A	COMM	3U	3 x Torque Coils	355x700 km	4	COMM payload with 2 transponders for AMSAT
330	2015	BRICSAT-P	Tech Demo	1.5U	4 x Thrusters Passive Magnetic Control	500 km	3	Propulsion test for miniature pulse plasma thruster
331	2015	GEARRS 2	Tech Demo	3U	N/A	N/A	N/A	C2 in Space
332 333	2015	AEROCUBE 8A-8B	Tech Demo	1.5U	N/A	390x700 km	N/A	Ion electrospray propulsion system
334	2015	LIGHTSAIL A	Tech Demo	3U	3 x Torque Coils Momentum Wheel	800 km	5	Solar sail
335 342	2015	FLOCK-1F 1 FLOCK-1F 8	Earth Observation	3U	3 x Torque Coils 3 x Reaction Wheels	370x430km	1	Imaging (3-5 m Res.), largest constellation
343 356	2015	FLOCK-1E 1 FLOCK-1E 14	Earth Observation	3U	3 x Torque Coils 3 x Reaction Wheels	370x430km	1	Imaging (3-5 m Res.), largest constellation
357	2015	CENTENNIAL-1	Tech Demo	1U	N/A	400 km	1	SSA/photon detector
358	2015	SERPENS	Tech Demo	3U	Electric Propulsion	400 km	2	Data collection
359	2015	S-CUBE	Scientific	3U	3 x Torque Coils Gravity Gradient	400 km	2	Observation of meteors
360	2015	DCBB (CAS 3G)	COMM	2U	N/A	N/A	N/A	Amateur Radio
361	2015	NJFA (TW 1C)	Tech Demo	3U	N/A	481 km	3	Space networking
362	2015	NJUST 2 (TW 1B)	Tech Demo	2U	N/A	481 km	3	Space networking
363	2015	SHANGKEDA 2 (TW 1A)	Tech Demo	2U	N/A	481 km	3	Space networking
364	2015	LEMUR 2 JOEL	Earth Observation	3U	N/A	650 km	2	Maritime surveillance/ AIS
365	2015	LEMUR 2 PETER	Earth Observation	3U	N/A	650 km	2	Maritime surveillance/ AIS
366	2015	LEMUR 2 JEROEN	Earth Observation	3U	N/A	650 km	2	Maritime surveillance/ AIS
367	2015	LEMUR 2 CHRIS	Earth Observation	3U	N/A	650 km	2	Maritime surveillance/ AIS
368	2015	GOMX-3	COMM	3U	3 x Reaction Wheels 3 x Torque Coils	400 km	3	High data rate communication
369	2015	AAUSAT-5	Tech Demo	3U	3 x Torque Coils	400 km	3	AIS
370 379	2015	FLOCK 2B (01-10)	Earth Observation	3U	3 x Reaction Wheels 3 x Torque Coils	400 km	4	Imaging
380	2015	AEROCUBE 5C	Tech Demo	1.5U	N/A	500x800km	3	Tracking, optical/laser COMM
381	2015	AEROCUBE 7	Tech Demo	1.5U	3 x Reaction Wheels 3 x Torque Coils	500x800km	3	Tracking, optical/laser COMM
382	2015	FOX 1A	COMM	1U	Passive Magnetic Control	500x800km	4	Analog FM Repeater
383	2015	BISONSAT	Scientific	1U	Passive Magnetic Control	500x800km	4	Atmospheric aerosols and cloud formations
384	2015	ARC-1	Tech Demo	1U	3 x Torque Coils	500x800km	3	Low Power ADCS
385	2015	SNAP-3 ALICE	Military	3U	Thrusters	500x800km	3	Beyond line-of-sight communication
386	2015	LMRST	Tech Demo	2U	Passive Magnetic Cont	500x800km	2	Tracking/navigation
387	2015	SNAP-3 EDDIE	Military	3U	Thrusters	500x800km	3	Beyond line-of-sight Communication
388	2015	PROPCUBE MERRYWEATHER	Scientific	1U	N/A	500x800km	2	Electron density and irregularities in ionosphere
389	2015	SINOD-D-1	Tech Demo	2U	N/A	500x800km	2	High-speed data downlink
390	2015	SNAP-3 JIMI	Military	3U	Thrusters	500x800km	3	Beyond line-of-sight COMM
391	2015	PROPCUBE FLORA	Scientific	1U	N/A	500x800km	2	Electron density and irregularities in ionosphere

392	2015	SINOD-D-3	Tech Demo	2U	N/A	500x800km	2	High-speed data downlink
393 394	2015	FLOCK 2B (13-14)	Earth Observation	3U	3 x Reaction Wheels 3 x Torque Coils	400 km	4	Imaging (3-5 m Res.), largest constellation
395	2015	ARGUS	Tech Demo	2U	Passive Magnetic Control	430x500km	1	Radiation effects
396	2015	PRINTSAT	Tech Demo	1U	Passive Magnetic Control	430x500km	1	3D printed material test in space
397 404	2015	EDSN 1–7	Tech Demo	1.5U	3 x Reaction Wheels 3 x Torque Coils	430x500km	1	Cross-link COMM, Multi-point scientific measurements
405	2015	SUPERNOVA -BETA	Tech Demo	6U	N/A	430x500km	1	Subsystem test in space
406	2015	STACEM	Earth Observation	3U	N/A	430x500km	1	Imaging
407 408	2015	FLOCK 2B (11-12)	Earth Observation	3U	3 x Reaction Wheels 3 x Torque Coils	430x500km	1	Imaging

Adapted from [44], [45], [46], and [47].

THIS PAGE INTENTIONALLY LEFT BLANK

APPENDIX B. CUBESAT DESIGN SPECIFICATION

The CubeSat prototype design in this study considered the CDS [57] during the component selections and mechanical and electrical designs. In order to keep the latest version of the CDS for this study, a digital public access document [57], minus the appendices, is added here as an appendix. Therefore, if the CDS is changed completely or abolished, readers will have access to the particular revision of the CDS, which the Shift-Mass Sat design was based on.

	Document Classification
X	Public Domain
	ITAR Controlled
	Internal Only

CubeSat Design Specification

(CDS)
REV 13

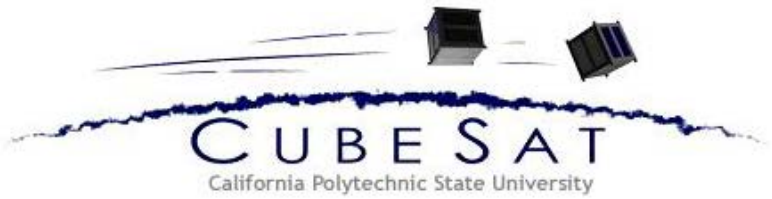

CHANGE HISTORY LOG

Effective Date	Revision	Author	Description of Changes
N/A	8	Simon Lee	N/A
5/26/05	8.1	Amy Hutputanasin	Formatting updated.
5/15/06	9	Armen Toorian	Information and presentation revised.
8/2/07	10	Wenschel Lan	Information updated.
10/02/08	11	Riki Munakata	Format, Design specification and Mk.III P-POD compatibility update.
8/1/09	12	Riki Munakata	Requirements update, waiver form requirements, and 3U CubeSat Specification drawing.
3/30/12	12.1	Justin Carnahan	Reformatted document to improve readability, updated to include 1.5U, 2U, and 3U+. Added and modified some req.
7/12/13	13-draft	David Pignatelli	Added applicable documents section. Removed restrictions on propulsion, added guidance for propulsion systems and hazardous materials. Added magnetic field restrictions and suggestions. Cleaned Section 3.2. Added custom spring plunger specs and recommendation. Extended restrictions on inhibits. Added links to outside resources. Cleaned Section 4.
2/20/14	13	Arash Mehrparvar	Fixed page numbering, error in spring plunger thread callout, other minor edits based on external suggestions.

TABLE OF CONTENTS

List of Acronyms

AFSPCMAN	Air Force Space Command Manual
CAC	CubeSat Acceptance Checklist
Cal Poly	California Polytechnic State University, San Luis Obispo
CDS	CubeSat Design Specification
cm	Centimeters
CVCM	Collected Volatile Condensable Mass
DAR	Deviation Wavier Approval Request
FCC	Federal Communication Commission
GSFC	Goddard Space Flight Center
IARU	International Amateur Radio Union
kg	Kilogram
LSP	Lunch Services Program
LV	Launch Vehicle
MIL	Military
mm	Millimeters
NASA	National Aeronautics and Space Administration
NPR	NASA Procedural Requirements
P-POD	Poly Picosatellite Orbital Deployer
RBF	Remove Before Flight
Rev.	Revision
RF	Radio Frequency
SLO	San Luis Obispo
SSDL	Space Systems Development Lab
STD	Standard
TML	Total Mass Loss
µm	Micrometer

Applicable Documents

The following documents form a part of this document to the extent specified herein. In the event of conflict between the documents referenced herein and the contents of this document, the contents of this document shall take precedence.

LSP Program Level P-POD and CubeSat Requirements Document (LSP-REQ-317.01)

General Environmental Verification Standard for GSFC Flight Programs and Projects (GSFC-STD-7000)

Military Standard Test Requirements for Launch, Upper-stage, and Space Vehicles (MIL-STD-1540)

Air Force Space Command Manual 91-710, Range Safety User Requirements Manual (AFSPCMAN 91-710)

Metallic Material Properties (MIL-HDBK-5)

Standard Materials and Processes Requirements for Spacecraft (NASA-STD-6016)

NASA Procedural Requirements for Limiting Orbital Debris (NPR 8715.6)

Introduction

1.1 Overview

Started in 1999, the CubeSat Project began as a collaborative effort between Prof. Jordi Puig-Suari at California Polytechnic State University (Cal Poly), San Luis Obispo, and Prof. Bob Twiggs at Stanford University's Space Systems Development Laboratory (SSDL). The purpose of the project is to provide a standard for design of picosatellites to reduce cost and development time, increase accessibility to space, and sustain frequent launches. Presently, the CubeSat Project is an international collaboration of over 100 universities, high schools, and private firms developing picosatellites containing scientific, private, and government payloads. A CubeSat is a 10 cm cube with a mass of up to 1.33 kg. Developers benefit from the sharing of information within the community. If you are planning to start a CubeSat project, please contact Cal Poly. Visit the CubeSat website at http://cubesat.org for more information.

Figure 1: Six CubeSats and their deployment systems.

1.2 Purpose

The primary mission of the CubeSat Program is to provide access to space for small payloads. The primary responsibility of Cal Poly, as the developer of the Poly Picosatellite Orbital Deployer (P-POD), is to ensure the safety of the CubeSat and protect the launch vehicle (LV), primary payload, and other CubeSats. CubeSat developers should play an active role in ensuring the safety and success of CubeSat missions by implementing good engineering practice, testing, and verification of their systems. Failures of CubeSats, the P-POD, or interface hardware can damage the LV or a primary payload and put the entire CubeSat Program in jeopardy. As part of the CubeSat Community, all participants have an obligation to ensure safe operation of their systems and to meet the design and minimum testing requirements outlined in this document. Requirements in this document may be superseded by launch provider requirements.

1.3 Waiver Process

Developers will fill out a "Deviation Waiver Approval Request (DAR)" (see appendix A) if their CubeSat is in violation of any requirements in sections 2 or 3. The waiver process is intended to be quick and easy. The intent is to help facilitate communication and explicit documentation

between CubeSat developers, P-POD integrators, range safety personnel, and launch vehicle providers. This will help to better identify and address any issues that may arise prior to integration and launch. The DAR can be found at http://www.cubesat.org/ and waiver requests should be sent to standards@cubesat.org.

Upon completion of the DAR, the P-POD Integrator will review the request, resolve any questions, and determine if there are any additional tests, analyses or costs to support the waiver. If so, the Developer, with inputs from the P-POD Integrator, will write a test plan and perform the tests before the waiver is conditionally accepted by the P-POD Integrator. Waivers can only be conditionally accepted by the P-POD Integrator until a launch has been identified for the CubeSat. Once a launch has been identified, the waiver becomes mission specific and passes to the launch vehicle Mission Manager for review. The launch vehicle Mission Manager has the final say on acceptance of the waiver, and the Mission Manager may require more corrections and/or testing to be performed before approving the waiver. Developers should realize that each waiver submitted reduces the chances of finding a suitable launch opportunity.

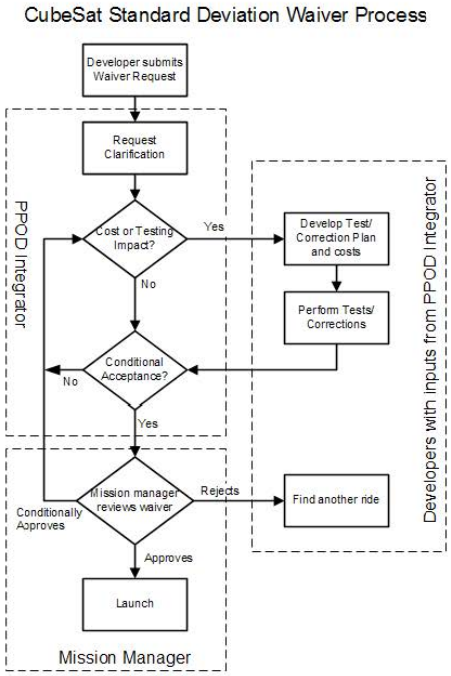

Figure 2: CubeSat Standard Deviation Wavier Process Flow Diagram

2. Poly Picosatellite Orbital Deployer

2.1 Interface

The Poly Picosatellite Orbital Deployer (P-POD) is Cal Poly's standardized CubeSat deployment system. It is capable of carrying three standard CubeSats and serves as the interface between the CubeSats and LV. The P-POD is a rectangular box with a door and a spring mechanism. Once the release mechanism of the P-POD is actuated by a deployment signal sent from the LV, a set of torsion springs at the door hinge force the door open and the CubeSats are deployed by the main spring gliding on its rails and the P-PODs rails (P-POD rails are shown in Figure 3b). The P-POD is made up of anodized aluminum. CubeSats slide along a series of rails during ejection into orbit. CubeSats will be compatible with the P-POD to ensure safety and success of the mission by meeting the requirements outlined in this document. The P-POD is backward compatible, and any CubeSat developed within the design specification of CDS rev. 9 and later will not have compatibility issues. Developers are encouraged to design to the most current CDS to take full advantage of the P-POD features.

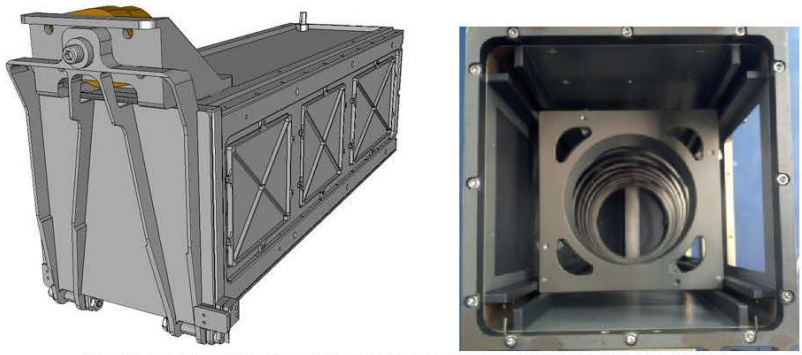

Figure 3a and 3b: Poly Picosatellite Orbital Deployer (P-POD) and cross section

3. CubeSat Specification

3.1 General Requirements

3.1.1 CubeSats which incorporate any deviation from the CDS will submit a DAR and adhere to the waiver process (see Section 1.3 and Appendix A).

3.1.2 All parts shall remain attached to the CubeSats during launch, ejection and operation. No additional space debris will be created.

3.1.3 No pyrotechnics shall be permitted.

3.1.4 Any propulsion systems shall be designed, integrated, and tested in accordance with AFSPCMAN 91-710 Volume 3.

3.1.5 Propulsion systems shall have at least 3 inhibits to activation.

3.1.6 Total stored chemical energy will not exceed 100 Watt-Hours.

3.1.6.1 Note: Higher capacities may be permitted, but could potentially limit launch opportunities.

3.1.7 CubeSat hazardous materials shall conform to AFSPCMAN 91-710, Volume 3.

3.1.8 CubeSat materials shall satisfy the following low out-gassing criterion to prevent contamination of other spacecraft during integration, testing, and launch. A list of NASA approved low out-gassing materials can be found at: http://outgassing.nasa.gov

3.1.8.1 CubeSats materials shall have a Total Mass Loss (TML) $\leq$ 1.0 %

3.1.8.2 CubeSat materials shall have a Collected Volatile Condensable Material (CVCM) $\leq$ 0.1%

3.1.9 The latest revision of the CubeSat Design Specification will be the official version which all CubeSat developers will adhere to. The latest revision is available at http://www.cubesat.org.

3.1.9.1 Cal Poly will send updates to the CubeSat mailing list upon any changes to the specification. You can sign-up for the CubeSat mailing list here: www.cubesat.org/index.php/about-us/how-to-join

3.1.10 Note: Some launch vehicles hold requirements on magnetic field strength. Additionally, strong magnets can interfere with the separation between CubeSat spacecraft in the same P-POD. As a general guideline, it is advised to limit magnetic field outside the CubeSat static envelope to 0.5 Gauss above Earth's magnetic field.

3.1.11 The CubeSat shall be designed to accommodate ascent venting per ventable volume/area $<$ 2000 inches.

3.2 CubeSat Mechanical Requirements

CubeSats are cube shaped picosatellites with dimensions and features outlined in the CubeSat Specification Drawing (Appendix B). The PPOD coordinate system is shown below in Figure 4 for reference. General features of all CubeSats include:

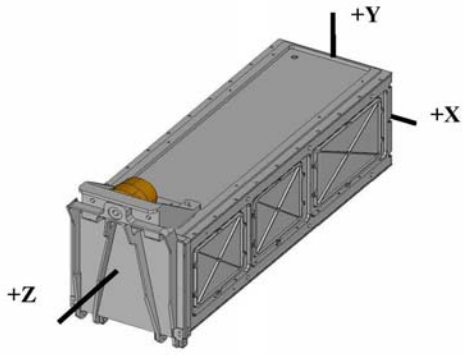

Figure 4: PPOD Coordinate System

3.2.1 The CubeSat shall use the coordinate system as defined in Appendix B for the appropriate size. The CubeSat coordinate system will match the P-POD coordinate system while integrated into the P-POD. The origin of the CubeSat coordinate system is located at the geometric center of the CubeSat.

3.2.1.1 The CubeSat configuration and physical dimensions shall be per the appropriate section of Appendix B.

3.2.1.2 The extra volume available for 3U+ CubeSats is shown in Figure 6.

3.2.2 The –Z face of the CubeSat will be inserted first into the P-POD.

3.2.3 No components on the green and yellow shaded sides shall exceed 6.5 mm normal to the surface.

3.2.3.1 When completing a CubeSat Acceptance Checklist (CAC), protrusions will be measured from the plane of the rails.

3.2.4 Deployables shall be constrained by the CubeSat, not the P-POD.

3.2.5 Rails shall have a minimum width of 8.5mm.

3.2.6 Rails will have a surface roughness less than 1.6 µm.

3.2.7 The edges of the rails will be rounded to a radius of at least 1 mm

3.2.8 The ends of the rails on the +/- Z face shall have a minimum surface area of 6.5 mm x 6.5 mm contact area for neighboring CubeSat rails (as per Figure 6).

3.2.9 At least 75% of the rail will be in contact with the P-POD rails. 25% of the rails may be recessed and no part of the rails will exceed the specification.

3.2.10 The maximum mass of a 1U CubeSat shall be 1.33 kg.

3.2.10.1 Note: Larger masses may be evaluated on a mission to mission basis.

3.2.11 The maximum mass of a 1.5U CubeSat shall be 2.00 kg.

3.2.11.1 Note: Larger masses may be evaluated on a mission to mission basis.

3.2.12 The maximum mass of a 2U CubeSat shall be 2.66 kg.

3.2.12.1 Note: Larger masses may be evaluated on a mission to mission basis.

3.2.13 The maximum mass of a 3U CubeSat shall be 4.00 kg.

3.2.13.1 Note: Larger masses may be evaluated on a mission to mission basis.

3.2.14 The CubeSat center of gravity shall be located within 2 cm from its geometric center in the X and Y direction.

3.2.14.1 The 1U CubeSat center of gravity shall be located within 2 cm from its geometric center in the Z direction.

3.2.14.2 The 1.5U CubeSat center of gravity shall be located within 3 cm from its geometric center in the Z direction.

3.2.14.3 The 2U CubeSat center of gravity shall be located within 4.5 cm from its geometric center in the Z direction.

3.2.14.4 3U and 3U+ CubeSats' center of gravity shall be located within 7 cm from its geometric center in the Z direction.

3.2.15 Aluminum 7075, 6061, 5005, and/or 5052 will be used for both the main CubeSat structure and the rails.

3.2.15.1 If other materials are used the developer will submit a DAR and adhere to the waiver process.

3.2.16 The CubeSat rails and standoff, which contact the P-POD rails and adjacent CubeSat standoffs, shall be hard anodized aluminum to prevent any cold welding within the P-POD.

3.2.17 The 1U, 1.5U, and 2U CubeSats shall use separation springs to ensure adequate separation.

3.2.17.1 Note: Recommended separation spring specifications are shown below in Table 1. **These are a custom part available through Cal Poly. Contact cubesat@gmail.com in order to obtain these separation springs.**

3.2.17.2 The compressed separation springs shall be at or below the level of the standoff.

3.2.17.3 The 1U, 1.5U, and 2U CubeSat separation spring will be centered on the end of the standoff on the CubeSat's –Z face as per Figure 7.

3.2.17.4 Separation springs are not required for 3U CubeSats.

Table 1: CubeSat Separation Spring Characteristics

Characteristics	***Value***
Plunger Material	*Stainless Steel*
End Force Initial/Final	*0.14 lbs. / 0.9 lbs.*
Throw Length	*0.16 inches minimum above the standoff surface*
Thread Pitch	*8-36 UNF-2B*

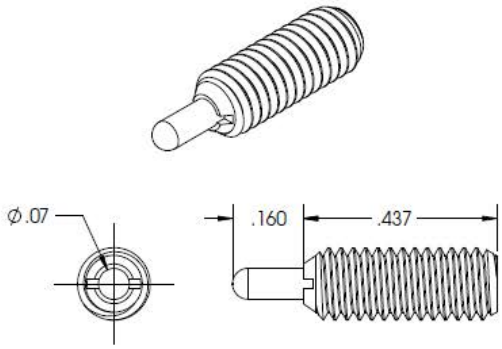

Figure 5: Custom Spec Spring Plunger (Separation Spring)

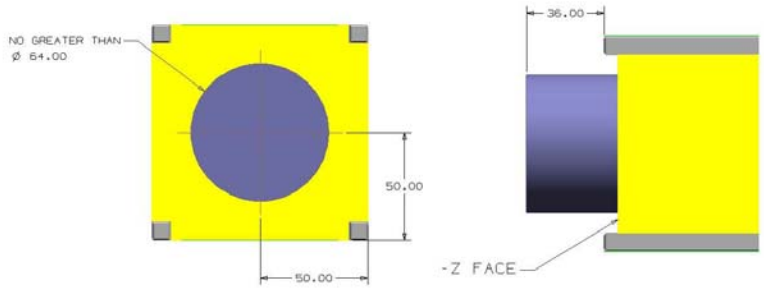

Figure 6: 3U+ Extra Volume ("Tuna Can")

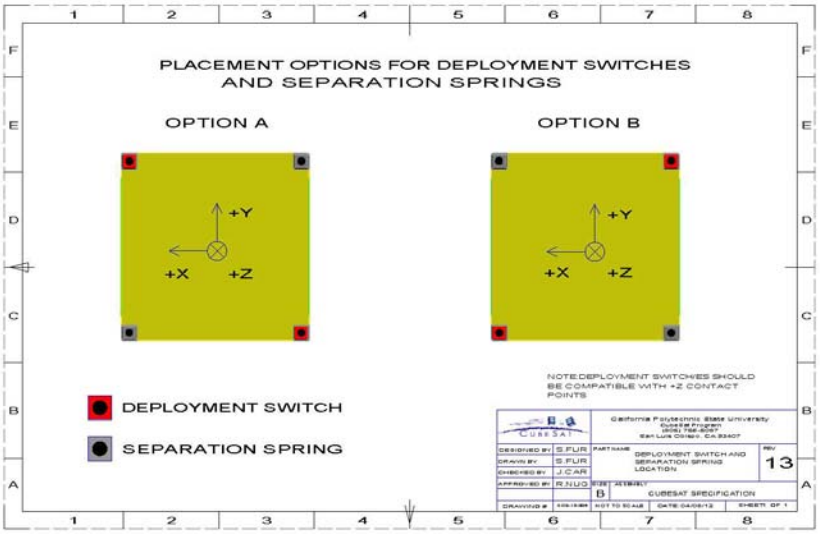

Figure 7: Deployment Switches and Separation Spring Locations

3.3 *Electrical Requirements*

Electronic systems will be designed with the following safety features.

3.3.1 The CubeSat power system shall be at a power off state to prevent CubeSat from activating any powered functions while integrated in the P-POD from the time of delivery to the LV through on-orbit deployment. CubeSat powered function include the variety of subsystems such as Command and Data Handling (C&DH), RF Communication, Attitude Determine and Control (ADC), deployable mechanism actuation. CubeSat power systems include all battery assemblies, solar cells, and coin cell batteries.

3.3.2 The CubeSat shall have, at a minimum, one deployment switch on a rail standoff, per Figure 7.

3.3.3 In the actuated state, the CubeSat deployment switch shall electrically disconnect the power system from the powered functions; this includes real time clocks (RTC).

3.3.4 The deployment switch shall be in the actuated state at all times while integrated in the P-POD.

3.3.4.1 In the actuated state, the CubeSat deployment switch will be at or below the level of the standoff.

3.3.5 If the CubeSat deployment switch toggles from the actuated state and back, the transmission and deployable timers shall reset to t=0.

3.3.6 The RBF pin and all CubeSat umbilical connectors shall be within the designated Access Port locations, green shaded areas shown in Appendix B.

3.3.6.1 Note: All diagnostics and battery charging within the P-POD will be done while the deployment switch is depressed.

3.3.7 The CubeSat shall include an RBF pin.

3.3.7.1 The RBF pin shall cut all power to the satellite once it is inserted into the satellite.

3.3.7.2 The RBF pin shall be removed from the CubeSat after integration into the P-POD.

3.3.7.3 The RBF pin shall protrude no more than 6.5 mm from the rails when it is fully inserted into the satellite.

3.3.8 CubeSats shall incorporate battery circuit protection for charging/discharging to avoid unbalanced cell conditions.

3.3.9 The CubeSat shall be designed to meet at least one of the following requirements to prohibit inadvertent radio frequency (RF) transmission. The use of three independent inhibits is highly recommended and can reduce required documentation and analysis.

An inhibit is a physical device between a power source and a hazard. A timer is not considered an independent inhibit.

3.3.9.1 The CubeSat will have one RF inhibit and RF power output of no greater than 1.5W at the transmitting antenna's RF input.

3.3.9.2 The CubeSat will have two independent RF inhibits

3.4 Operational Requirements

CubeSats will meet certain requirements pertaining to integration and operation to meet legal obligations and ensure safety of other CubeSats.

3.4.1 Operators will obtain and provide documentation of proper licenses for use of radio frequencies.

3.4.1.1 For amateur frequency use, this requires proof of frequency coordination by the International Amateur Radio Union (IARU). Applications can be found at www.iaru.org.

3.4.2 CubeSats will comply with their country's radio license agreements and restrictions.

3.4.3 CubeSats mission design and hardware shall be in accordance with NPR 8715.6 to limit orbital debris.

3.4.3.1 Any CubeSat component shall re-enter with energy less than 15 Joules.

3.4.3.2 Developers will obtain and provide documentation of approval of an orbital debris mitigation plan from the FCC (or NOAA if imager is present).

3.4.3.2.1 Note: To view FCC amateur radio regulations, go to http://www.arrl.org/part-97-amateur-radio

3.4.3.3 Note: Analysis can be conducted to satisfy the above with NASA DAS, available at http://orbitaldebris.jsc.nasa.gov/mitigate/das.html

3.4.4 All deployables such as booms, antennas, and solar panels shall wait to deploy a minimum of 30 minutes after the CubeSat's deployment switch(es) are activated from P-POD ejection.

3.4.5 No CubeSats shall generate or transmit any signal from the time of integration into the P-POD through 45 minutes after on-orbit deployment from the P-POD. However, the CubeSat can be powered on following deployment form the P-POD.

3.4.6 Private entities (non-U.S. Government) under the jurisdiction or control of the United States who propose to operate a remote sensing space system (satellite) may need to have a license as required by U.S. law. For more information visit http://www.nesdis.noaa.gov/CRSRA/licenseHome.html. Click on the Application Process link under the Applying for a License drop down section to begin the process.

3.4.7 Cal Poly will conduct a minimum of one fit check in which developer hardware will be inspected and integrated into the P-POD or TestPOD. A final fit check will be conducted prior to launch. The CubeSat Acceptance Checklist (CAC) will be used to verify compliance of the specification (Found in the appendix of this document or online at http://cubesat.org/index.php/documents/developers).

4. Testing Requirements

Testing will be performed to meet all launch provider requirements as well as any additional testing requirements deemed necessary to ensure the safety of the CubeSats, P-POD, and the primary mission. If the launch vehicle environment is unknown, The General Environmental Verification Standard (GEVS, GSFC-STD-7000) and MIL-STD-1540 can be used to derive testing requirements. GSFC-STD-7000 and MIL-STD-1540 are useful references when defining testing environments and requirements, however the test levels defined in GSFC-STD-7000 and MIL-STD-1540 are not guaranteed to encompass or satisfy all LV testing environments. Test requirements and levels that are not generated by the launch provider or P-POD Integrator are considered to be unofficial. The launch provider testing requirements will supersede testing environments from any other source. The P-POD will be tested in a similar fashion to ensure the safety and workmanship before integration with the CubeSats. At the very minimum, all CubeSats will undergo the following tests.

4.1 Random Vibration

Random vibration testing shall be performed as defined by the launch provider

4.2 Thermal Vacuum Bakeout

Thermal vacuum bakeout shall be performed to ensure proper outgassing of components. The test specification will be outlined by the launch provider.

4.3 Shock Testing

Shock testing shall be performed as defined by the launch provider.

4.4 Visual Inspection

Visual inspection of the CubeSat and measurement of critical areas will be performed per the appropriate CAC (Appendix C).

4.5 CubeSat Testing Philosophy

The CubeSat shall be subjected to either a qualification or protoflight testing as defined in the CubeSat Testing Flow Diagram, shown in Figure 88. The test levels and durations will be supplied by the launch provider or P-POD integrator.

4.5.1 Qualification

Qualification testing is performed on an engineering unit hardware that is identical to the flight model CubeSat. Qualification levels will be determined by the launch vehicle provider or P-POD integrator. Both MIL-STD-1540 and LSP-REQ-317.01 are used as guides in determining testing levels. The flight model will then be tested to Acceptance levels in a TestPOD then integrated into the flight P-POD for a final acceptance/workmanship random vibration test. **Additional testing may be required if modifications or changes are made to the CubeSats after qualification testing.**

4.5.2 Protoflight

Protoflight testing is performed on the flight model CubeSat. Protoflight levels will be determined by the launch vehicle provider or P-POD integrator. Both MIL-STD-1540 and LSP-REQ-317.01 are used as guides in determining testing levels. The flight model will be tested to Protoflight levels in a TestPOD then integrated into the flight P-POD for a final acceptance/workmanship random vibration test. The flight CubeSat **SHALL NOT** be disassembled or modified after protoflight testing. Disassembly of hardware after protoflight testing will require the developer to submit a DAR and adhere to the waiver process prior to disassembly. **Additional testing will be required if modifications or changes are made to the CubeSats after protoflight testing.**

4.5.3 Acceptance

After delivery and integration of the CubeSat into the P-POD, additional testing will be performed with the integrated system. This test ensures proper integration of the CubeSat into the P-POD. Additionally, any unknown, harmful interactions between CubeSats may be discovered during acceptance testing. The P-POD Integrator will coordinate and perform acceptance testing. Acceptance levels will be determined by the launch vehicle provider or P-POD integrator. Both MIL-STD-1540 and LSP-REQ-317.01 are used as guides in determining testing levels. The P-POD **SHALL NOT** be deintegrated at this point. If a CubeSat failure is discovered, a decision to deintegrate the P-POD will be made by the developers, in that P-POD, and the P-POD Integrator based on safety concerns. The developer is responsible for any additional testing required due to corrective modifications to deintegrated P-PODs and CubeSats.

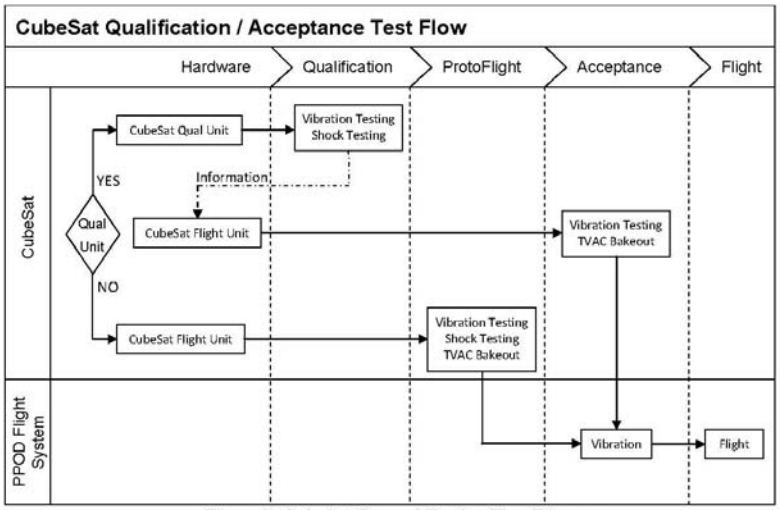

Figure 8: CubeSat General Testing Flow Diagram

5. Contacts

Cal Poly - San Luis Obispo
Prof. Jordi Puig-Suari
Aerospace Engineering Dept.
(805) 756-5087
(805) 756-2376 fax
jpuigsua@calpoly.edu

SRI International
Dr. Scott Williams, Program Manager
Engineering Systems Division
(650) 859-5057
(650) 859-3919 fax
scott.williams@sri.com

Cal Poly Program Manager
Roland Coelho
(805) 756-5087
(805) 756-5165 fax
rcoelho@calpoly.edu

Cal Poly Student Contacts
(805) 756-5087
(805) 756-5165 fax
cubesat@gmail.com

LIST OF REFERENCES

[1] H. Helvajian and S. W. Janson, *Small Satellites: Past, Present, and Future*, Reston, VA: AIAA, 2009.

[2] J. Puig-Suari, "The CubeSat: The picosatellite standard for research and education," presented at AIAA SPACE 2008 Conference & Exposition, San Diego, CA, 2008.

[3] S. Chesi, "Attitude control of nanosatellite using shifting masses," PhD Dissertation, Graduate Division of the University of California, Santa Cruz, CA, 2014.

[4] R. S. Jakhu and J. N. Pelton, "The development of small satellite systems and technologies," in *Small Satellites and Their Regulations*, New York, NY: Springer, 2014, pp 13-20.

[5] *Smallsat deployment*. (2015). NanoRacks LLC. [Online]. Available: http://nanoracks.com/products/smallsat-deployment/. Accessed 30 January 2016.

[6] *Nanosatellite Launch Adapter System (NLAS)*. (2013, Apr. 30). NASA. [Online]. Available:http://www.nasa.gov/centers/ames/engineering/projects/nlas.html#.Vqx19rIrIgs. Accessed 30 January 2016.

[7] A. DeJesus, C. Hicks, M. Crook, A. Harris, and J. Newman, "NPS CubeSat launcher (NPSCuL) program update," presented at 2009 CubeSat Developers Workshop, San Luis Obispo, CA, 2009. [Online]. Available: http://mstl.atl.calpoly.edu/~bklofas/Presentations/DevelopersWorkshop2009/8_Access_to_Space/1_Tito-NPSCuL.pdf. Accessed 30 January 2016.

[8] *ISIPOD CubeSat deployer*. (2016). ISIS. [Online]. Available: http://www.isispace. nl/brochures/ISIS_ISIPOD_Brochure_v.7.11.pdf. Accessed 30 January 2016.

[9] R. Hevner, W. Holemans, J. Puig-Suari, and R. Twiggs, "An Advanced Standard for CubeSats," in 25th Annual AIAA/USU Conference on Small Satellites, Logan, UT, 2011, pp. 9.

[10] R. Sandau, "High resolution imaging with small satellites: what are the possibilities and limitations," in *Sensors and Systems for Space Applications*, Orlando, FL, 2007.

[11] R. Sandau, R. Hans-Peter, and V. Arnoldo, *Small Satellites for Earth Observation*, London, UK: Springer, 2008.

[12] F. Stesina, S. Corpino, R. Mozzillo, and R. G. Obiols, “Design of the active attitude determination and control system for the e-st@r CubeSat,” in 63rd International Astronautical Congress, Naples, Italy, 2012.

[13] *Microspace*. (n.d.). Microspace Rapid Pte Ltd. [Online]. Available: http://pop-sat.com/. Accessed 30 July 2015.

[14] J. D. Munoz, V. Nagabhushan, S. Asundi, and N. Fitz-Coy, “High fidelity simulation of SwampSat attitude determination and control system,” in 21st AAS/ AIAA Space Flight Mechanics Meeting, New Orleans, Louisiana, 2011.

[15] H. Kayal and K. Briess, “Pico satellite concept of TU Berlin,” in *Small Satellites for Earth Observation: Selected Proceedings of the 5th International Symposium of the International Academy of Astronautics*, Berlin, Germany, 2005.

[16] C. Venturini, “Small satellite technology: Industry update” presented at Advisory Committee on Commercial Remote Sensing (ACCRES), The Aerospace Corporation, 2014.

[17] J. J. Sellers, *Understanding Space an Introduction to Astronautics*, 2nd ed. New York, NY: McGraw-Hill Companies, 2005.

[18] P. C. Hughes, *Spacecraft Attitude Dynamics*, Mineola, NY: Dover Publications, 2004.

[19] J. R. Wertz and W. J. Larson, *Space Mission Analysis and Design*, 3rd ed. Boston, MA: Microcosm, 1999.

[20] B. Wie, *Space Vehicle Dynamics and Control*, 2nd ed. Reston, VA: AIAA, 2008.

[21] C. Cappelletti, G. Matinotti, and F. Graziani, “Unicubesat: a test for the gravity-gradient solar array boom,” in 62nd International Astronautics Congress, Cape Town, South Africa, 2011.

[22] National Science Foundation, “CubeSat-based science missions for geospace and atmosphere research,” NASA, Wallops Island, VA, Tech. Rep. NP-2013-12-097-GSFC, Oct. 2013.

[23] *DTUsat project—attitude control system*. (n.d.). Technical University of Denmark. [Online]. Available: http://www.dtusat.dtu.dk/index.php?id=25. Accessed 24 August 2015.

[24] *Earth observation portal*. (2015). European Space Agency. [Online]. Available: https://directory.eoportal.org/web/eoportal/home. Accessed 24 August 2015.

[25] *SkyCube*. (n.d.). Southern Stars Group. [Online]. Available: http://www.southernstars.com/skycube/satellite.html. Accessed 24 August 2015.

[26] *PolySat*. (n.d.). California Polytechnic State University. [Online]. Available: http://polysat.calpoly.edu/launched-missions/cp8-ipex/. Accessed 24 August 2015.

[27] *NanoSail-D*. (2010). NASA. [Online]. Available: http://www.nasa.gov/sites/default/files/484314main_NASAfactsNanoSail-D.pdf Accessed 24 August 2015.

[28] T. Miyashita, *Waseda satellite project*, Waseda University Faculty of Science and Engineering [Online]. Available: http://www.miyashita.mmech.waseda.ac.jp/Waseda-Sat2/missionkei.html. Accessed 24 August 2015.

[29] H. Curtis, *Orbital Mechanics for Engineering Students*, Oxford, UK: Elsevier Butterworth-Heinemann, 2005.

[30] F. L. Markley and J. L. Crassidis, *Fundamentals of Spacecraft Attitude Determination and Control*, New York, NY: Springer, 2014.

[31] R. H. Byrne, R. D. Robinett, and B. R. Sturgis, "Moving mass trim control system design," in AIAA Guidance, Navigation and Control Conference, San Diego, CA, 1996.

[32] T. Petsopoulos and F. J. Regan, "Moving mass roll control system for fixed-trim re-entry vehicle," *Journal of Spacecraft and Rockets*, vol. 33, no. 1, pp. 54-60, 1996.

[33] J. Rogers and M. Costello, "A variable stability projectile using an internal moving mass," presented at AIAA Atmospheric Flight Mechanics Conference and Exhibit, Honolulu, HI, 2008.

[34] R. D. Robinett III, B. R. Sturgis, and S. A. Kerr, "Moving mass trim control for aerospace vehicles," *Journal of Guidance, Control and Dynamics*, vol. 19, no. 5, pp. 1064-1070, 1996.

[35] P. Guo and L. Zhao, "Modeling and attitude control of a spinning spacecraft with internal moving mass," in 2nd International Conference on Computer Science and Electronics Engineering, Hangzhou, China, Mar. 2013.

[36] B. M. Atkins and E. M. Queen, "Internal moving mass actuator control for Mars entry guidance," Journal of Spacecraft and Rockets, vol. 52, no. 5, pp. 1294-1310, 2015.

[37] B. Wie, "Solar sail attitude control and dynamics, part 2," *Journal of Guidance, Control and Dynamics*, vol. 27, no. 4, pp. 536-544, 2004.

[38] B. Wie and D. Murphy, "Solar-sail attitude control design for a sail flight validation mission," Journal of Spacecraft and Rockets, vol. 44, no. 4, pp. 809-821, 2007.

[39] S. Thomas, M. Paluszek, B. Wie, and D. Murphy, “Design and simulation of sailcraft attitude control systems using the solar sail control toolbox,” in AIAA Guidance, Navigation and Control Conference and Exhibit, Providence, RI, 2004.

[40] C. Grubin, “Dynamics of a vehicle containing moving parts,” *Transactions of the ASME: Journal of Applied Mechanics*, vol. 29, pp. 486-488, 1962.

[41] T. L. Edwards and M. H. Kaplan, “Automatic spacecraft detumbling by internal mass motion,” *AIAA Journal*, vol. 12, no. 4, pp. 496-502, 1974.

[42] D. K. Kumar and A. M. Zou, “Attitude control of miniature satellites using movable masses,” in SpaceOps 2010 Conference, Huntsville, AL, 2010.

[43] Y. Jiang, F. He and Y. Yao, “Hybrid control strategy for attitude stabilization of an underactuated spacecraft with two moving mass,” in *Proceedings of the IEEE International Conference on Automation and Logistics*, Jian, China, 2007.

[44] M. Swartwout. (2015, Sep. 2) *CubeSat database*. [Online]. Available: https://sites.google.com/a/slu.edu/swartwout/home/cubesat-database. Accessed 2 September 2015.

[45] G. D. Krebs. (2015). *Gunter's space page*. [Online]. Available: http://space.skyrocket.de/index.html. Accessed 2 September 2015.

[46] *Earth observation portal*. (2015). ESA [Online]. Available: https://directory. eoportal.org/web/eoportal/satellite-missions. Accessed 2 September 2015.

[47] C. Lafleur. (2015). *Spacecraft encyclopedia*. [Online]. Available: http://claudelafleur.qc.ca/Spacecrafts-index.html#Table-1. Accessed 2 September 2015.

[48] *FLOCK 1*. (2015). Planet Labs Inc. [Online]. Available: https://www.planet.com/ flock1/. Accessed 2 September 2015.

[49] B. Blake and P. O'Brien. (2014). *AeroCube-6: a brief overview and first light*. [Online]. Available: http://rbspgway.jhuapl.edu/sites/default/files/20140923/ Day_1/Theme_3/04-Blake_AC6-RBSP-SWG_v2.pdf. Accessed 30 January 2016.

[50] *Fox-1*. (2014). AMSAT. [Online]. Available: http://www.work-sat.com/ FUNDRAISING _files/Fox-1_Handout-1.pdf. Accessed 30 January 2016.

[51] United States Naval Academy and George Washington University, “Ballistic reinforced communication satellite (BRICSat-P): the first flight of an electric micropropulsion system for CubeSat mission applications,” in 5th Interplanetary CubeSat Workshop, Oxford, UK, 2016.

[52] E. J. Simburger, S. Liu, J. Halpine, D. Hinkley, J. R. Srour, and D. Rumsey. (2006). *Pico satellite solar cell testbed (PSSC Testbed)*. [Online]. Available: http://ieeexplore.ieee.org/stamp/stamp.jsp?arnumber=4060049. Accessed 30 January 2016.

[53] M. Bertino and B. Cooper, "Perseus-M on-orbit report and Corvus-BC satellite design," presented at 2015 CubeSat Developers Workshop, San Luis Obispo, CA, 2015. [Online]. Available: http://mstl.atl.calpoly.edu/~bklofas/Presentations/DevelopersWorkshop2015/Bertino_Perseus-M_Corvus-BC.pdf. Accessed 30 January 2016.

[54] United States Naval Academy, "USS *Langley*," presented at 2014 CubeSat Developers Workshop, San Luis Obispo, CA, 2014. [Online]. Available: http://mstl.atl. calpoly.edu/~bklofas/Presentations/DevelopersWorkshop2014/Sipe_USS_Langley.pdf. Accessed 2 September 2015.

[55] *GOM SPACE*. (2015). GOMSpace. [Online]. Available: http://gomspace.com/index.php?p=products. Accessed 12 October 2015.

[56] *CubeSatShop*. (2015). ISIS. [Online]. Available: http://cubesatshop.com/. Accessed 12 October 2015.

[57] *CubeSat design specification (CDS) rev. 13*. (2015, Apr. 6). California Polytechnic State University. [Online]. Available: http://www.cubesat.org/images/developers/cds_rev13_ final2.pdf. Accessed 12 October 2015.

[58] *NanoCam C1U datasheet*. (2011). GOMSPACE. [Online]. Available: http://gomspace. com/documents/GS-DS-NANOCAM-6.2.pdf. Accessed 12 October 2015.

[59] *NanoPower P-110 series solar panels datasheet*. (2013). GOMSPACE. [Online]. Available: http://gomspace.com/documents/GS-DS-P110-1.0.pdf. Accessed 12 October 2015.

[60] *NanoPower BP series datasheet*. (2014). GOMSPACE. [Online]. Available: http://gomspace.com/documents/gs-ds-bp4.pdf. Accessed 12 October 2015.

[61] *NanoCom ANT430 datasheet*. (2014). GOMSPACE. [Online]. Available: http://gomspace.com/documents/GS-DS-NANOCOM-ANT.pdf. Accessed 12 October 2015.

[62] *NanoCom AX100 datasheet*. (2015). GOMSPACE. [Online]. Available: http://gomspace. com/documents/gs-ds-nanocom-ax100-1.7.pdf. Accessed 12 October 2015.

[63] *NanoMind A712D datasheet*. (2015). GOMSPACE. [Online]. Available: http://gomspace.com/documents/gs-ds-nanomind-a712d-1.5.pdf. Accessed 12 October 2015.

[64] *NanoDock motherboard DMC-3 datasheet*. (2015). GOMSPACE. [Online]. Available: http://gomspace.com/documents/gs-ds-nanodock-motherboard-dmc-3-1.3.pdf. Accessed 12 October 2015.

[65] *Receivers OEM615*. (2014). NovAtel [Online]. Available: http://www.novatel.com/assets/Documents/Papers/OEM615.pdf. Accessed 12 October 2015.

[66] *3-Unit CubeSat structure*. (2015). ISIS. [Online]. Available: http://cubesatshop.com/index.php?page=shop.product_details&flypage=flypage.tpl&product_id=4&category_id=1&option=com_virtuemart&Itemid=66. Accessed 12 October 2015.

[67] *MAI SES product specification*. (2014). Maryland Aerospace Inc. [Online]. Available: http://d6110363.ozt807.onezerotech.com/wp-content/uploads/2015/08/MAI-SES-Specifications-20150827.pdf. Accessed 12 October 2015.

[68] *MAI-SS space sextant*. (2015). Maryland Aerospace Inc. [Online]. Available: http://cubesatshop.com/index.php?page=shop.product_details&flypage=flypage.tpl&product_id=130&category_id=7&option=com_virtuemart&Itemid=69. Accessed 12 October 2015.

[69] *35000 series size 14 stepper motor linear actuators*. (n.d.). Hayden Kerk Motion Solutions. [Online]. Available: http://www.haydonkerk.com/LinearActuatorProducts/StepperMotorLinearActuators/LinearActuatorsHybrid/Size14LinearActuator/tabid/77/Default.aspx#stepper_motor_linear_actuator_noncaptive. Accessed 12 October 2015.

[70] *Sinclair Interplanetary—Reaction Wheels*. (2015). Sinclair Interplanetary. [Online]. Available: http://www.sinclairinterplanetary.com/reactionwheels. Accessed 27 November 2015.

[71] J. Armstrong, C. Casey, G. Creamer, and G. Dutchover, "Pointing control for low altitude triple CubeSat space darts," in 23rd Annual AIAA/USU Conference on Small Satellites, Logan, UT, 2009.

[72] O. A. Yakimenko, *Engineering Computations and Modeling in MATLAB/Simulink*, Reston, VA: American Institute of Aeronautics and Astronautics, 2011.

[73] "Spacecraft disturbance torques," class notes for Rotational Spacecraft Mechanics, Department of Mechanical and Aerospace Engineering, Naval Postgraduate School, Monterey, CA, Spring 2015.

[74] *NRLMSISE-00 model 2001*. (2002). Community Coordinated Modeling Center (CCMC), Goddard Space Flight Center, NASA [Online]. Available: http://ccmc.gsfc.nasa.gov/modelweb/atmos/nrlmsise00.html. Accessed 25 October 2015.

[75] D. P. Drob, and Coauthors, “An empirical model of the Earth's horizontal wind fields: HWM07,” *Journal of Geophysical Research-Space Physics*, vol. 113, no. A12304, 2008.

[76] K. Ogata, *Modern Control Engineering*, 4th ed. Boston, MA: Prentice-Hall, 2010.

[77] *The World Magnetic Model*. (2015, May 27). NOAA. [Online]. Available: http://www. ngdc.noaa.gov/geomag/WMM/DoDWMM.shtml. Accessed 27 November 2015.

THIS PAGE INTENTIONALLY LEFT BLANK

INITIAL DISTRIBUTION LIST

1. Defense Technical Information Center
   Ft. Belvoir, Virginia

2. Dudley Knox Library
   Naval Postgraduate School
   Monterey, California